Molecular Beam Epitaxy Growth and Magnetic Studies of Fe Ultrathin Structures

by

Zbigniew Jan Celinski
M.Sc., Silesian University ,1982
M.A., Temple University, 1988

THESIS SUBMITTED IN PARTIAL FULFILLMENT OF
THE REQUIREMENTS FOR THE DEGREE OF
DOCTOR OF PHILOSOPHY
in the Department
of
Physics

SIMON FRASER UNIVERSITY
January 1992

Approval

Name: Zbigniew Jan Celinski

Degree: Doctor of Philosophy

Title of Thesis: Molecular Beam Epitaxy Growth and Magnetic Studies of Fe Ultrathin Structures.

Examining Committee:

Chairman: Dr. L.E. Ballentine

Dr. B. Heinrich
Senior Supervisor

Dr. A.S. Arrott

Dr. J.F. Cochran

Dr. A.E. Curzon

Dr. B.A. Gurney
External Examiner
IBM Almaden Research Center

Date Approved: January 9, 1991

PARTIAL COPYRIGHT LICENSE

I hereby grant to Simon Fraser University the right to lend my thesis, project or extended essay (the title of which is shown below) to users of the Simon Fraser University Library, and to make partial or single copies only for such users or in response to a request from the library of any other university, or other educational institution, on its own behalf or for one of its users. I further agree that permission for multiple copying of this work for scholarly purposes may be granted by me or the Dean of Graduate Studies. It is understood that copying or publication of this work for financial gain shall not be allowed without my written permission.

Title of Thesis/Project/Extended Essay

Molecular Beam Epitaxy Growth and Magnetic Studies of Fe Ultrathin Structures

Author:

(signature)

Zbigniew Jan Celinski

(name)

Oct. 4th 1991

(date)

Abstract

Epitaxial trilayer Fe(001)/Cu,Pd,Ag,Au(001)/Fe(001) structures have been grown on bulk Ag(001) single crystal substrates using the technique of Molecular Beam Epitaxy (MBE). The growth of bcc Fe(001), metastable bcc Cu(001), lattice expanded fcc Pd(001) and fcc Ag(001) and Au(001) layers were monitored and characterized by Reflection High Energy Electron Diffraction (RHEED) patterns and RHEED intensity oscillations. RHEED study revealed that the metastable bcc Cu(001) maintains its structure for 10-11 atomic monolayers (ML) before undergoing a surface reconstruction. Ferromagnetic Resonance (FMR) and Surface Magneto-Optical Kerr Effect (SMOKE) were used to investigate the exchange coupling in these trilayers using a wide range of Cu, Pd, Ag and Au interlayer thicknesses. It is shown that Cu and Pd interlayers exhibit long range antiferromagnetic coupling. Both interlayers exhibit unique oscillatory behavior. The exchange coupling through bcc Cu exhibits only one crossover to antiferromagnetic coupling. The strength of the antiferromagnetic coupling reveals an oscillatory behavior with a periodicity of 10 monolayers. The exchange coupling through Pd(001) shows an oscillatory behavior with periodicity of ~4 ML, which is superimposed on a monotonically decreasing ferromagnetic background. For Pd layers thicker than 12ML the exchange coupling becomes antiferromagnetic. The exchange coupling through Au and Ag interlayers behaves very differently from that of Cu. Only the 13ML thick Au interlayer showed a very weak antiferromagnetic coupling. Ag(001) interlayers show a couple very weakly. Thicker Ag(001) (d>7ML) layers showed no measurable coupling.

Dedication

For my wife, Jolanta, and my daughters,
Katarzyna and Magdalena

Acknowledgments

It has been my privilege to work with the Magnetism and Surface Science Group at Simon Fraser University. First and foremost I gratefully acknowledge the guidance and assistance of my supervisor Bretislav Heinrich. His enormous experimental expertise and theoretical insight have been invaluable to this work. I consider myself very lucky to have had an advisor who always had time to discuss physics and was so tolerant of my ignorance.

I am very grateful to Anthony Arrott and John Cochran for their advice, assistance and many stimulating discussions, throughout my time as a graduate student. I thank Tony Arrott for a careful reading of this manuscript.

I thank my co-workers and friends, Ken Myrtle, Jeff Rudd, Maciek Kowalewski, Ken Urquhart, and Milton From for their advice, support and assistance in matters of FMR, MBE, and otherwise.

I wish to express my gratitude for the friendship and laughter I had with the many good people that I came to know during my time spent at SFU: your friendship and companionship will always be remembered and appreciated. Thanks.

The financial support from Simon Fraser University and my supervisor is gratefully acknowledged.

Table of Contents

List of Tables

Table **Page**

List of Figures

Chapter 1

Introduction

During the last decade the study of magnetic properties of ultrathin metallic layers has attracted wide interest. The progress in ultra high vacuum (UHV) technology and especially the employment of the molecular beam epitaxy (MBE) technique made possible the creation of metallic structures with interfaces that are sharp on the atomic scale. This development brought exciting ways of engineering new magnetic materials. New phenomena have been discovered such as giant magnetic anisotropies [1.1, 1.2], antiferromagnetic coupling between two ferromagnetic layers separated by a non magnetic interlayer [1.3], and giant magnetoresistance observed for the first time in antiferromagnetically coupled Fe layers [1.4]. These new discoveries have raised expectations for novel devices in the near future, especially in the field of magneto-optical recording. In fact new high density storage media have been developed using the giant perpendicular anisotropies.

The studies presented in this thesis were focused on exchange magnetic coupling. The antiferromagnetic coupling observed by Grünberg in $[Fe/Cr]_n$ multilayers [1.3] triggered this exciting field. Metallic Cr is antiferromagnetic below 311K. It has a half filled 3d band. The complex topology of its Fermi surface results in spin density waves in bulk Cr and therefore it was not entirely surprising that the Cr interlayers showed an oscillatory behavior in the exchange coupling [1.5]. The understanding of the exchange coupling is very difficult in general and it becomes particularly

hard in Cr which itself can exhibit a long range antiferromagnetic order. In order to avoid these complexities studies using interlayers with simpler electronic bands are preferable. Therefore studies of the exchange coupling were carried out using non magnetic interlayers with either completely filled d bands (Cu, Ag, Au) or nearly filled 4d bands (Pd). The results are presented in this thesis.

The ultrathin magnetic structures were prepared by MBE using carefully prepared fcc Ag(001) single crystals substrates. The Fe(001)/X(001), X(001)/Fe(001) bilayers and Fe(001)/X(001)/Fe(001) trilayers were grown in a low-10^{-10} Torr range with the substrate held at room temperature. X denotes Cu, Pd, Ag or Au.

The quality of growth was monitored by Reflection High Energy Electron Diffraction (RHEED). The RHEED glancing incident scattering geometry makes it possible to monitor and characterize continuously the growth process at every stage. The presence of RHEED oscillations indicates a good epitaxial growth having a surface roughness confined mostly to the top two atomic layers. RHEED patterns reflect the crystallographic structure and the morphology of the films. Auger Electron Spectroscopy (AES) was used to monitor both the surface contamination and the uniformity of the metallic layers (see chapter 2).

The 4-fold hollow surface sites of fcc Ag(001) are closely matched to the bcc Fe(001) lattice. The lateral mismatch is very small, 0.6%. The Fe(001) layers grow epitaxially in a layer by layer mode on well prepared Ag(001) substrates.

The growth of Cu(001) on Fe(001) templates is remarkable. A significant mismatch of 12.5% precludes the growth of fcc Cu(001) on bcc

Fe(001). In fact the Cu adatoms adopt the Fe in-plane spacing and follow the bcc structure of Fe. The Cu overlayers maintain the in-plane symmetry of the Fe(001) substrates for the first 10-11 monolayers (ML) and then undergo a complex surface reconstruction.

Pd(001) layers grow very well on Fe(001) templates despite their 5.1% lateral lattice mismatch. The RHEED patterns show that the growth follows the Fe square mesh very closely; no surface reconstruction is visible for films thinner than 12ML. Pd(001) layers on Fe(001) templates grow in a laterally expanded fcc structure (see chapter 3).

The FMR technique was used to measure the magnetic properties of the ultrathin structures. The magnetic properties of the individual layers were determined using bilayer structures, Fe(001)/X(001) and X(001)/Fe(001). The trilayer structures, Fe/X/Fe, were employed to determine the exchange magnetic coupling. In ultrathin films the magnetic moments within individual layers are uniform. The exchange coupling between Fe layers leads to two resonant modes. In the acoustic mode all magnetizations are in phase and in the optical mode the rf magnetizations precess out of phase [1.2]. The exchange interface energy, E^{AB}, between ferromagnetic layers A and B is defined by

$$E^{AB} = J^{AB} \frac{\mathbf{M}^A \cdot \mathbf{M}^B}{M^A M^B}$$

where J^{AB} is the exchange coupling coefficient between the magnetization $\mathbf{M}^A$ and $\mathbf{M}^B$. The values of the exchange coupling coefficient J^{AB} were determined by fitting the resonance peak positions of acoustic and optical modes using the theory of exchange coupled trilayers (see chapter 4).

The exchange coupling through metastable bcc Cu(001) interlayers possess several interesting features. For Cu interlayers thinner than 8ML the

exchange coupling was found to be ferromagnetic. The crossover from the ferromagnetic to antiferromagnetic coupling occurred at 8ML and the antiferromagnetic coupling reached its first broad maximum at 10.5 - 11.5ML. The exchange coupling then exhibited an oscillatory behavior but remained antiferromagnetic with a periodicity of ~10ML. The strength of the exchange coupling was not affected by the onset of the bcc Cu surface reconstruction. With decreasing temperatures from 300K to 77K the exchange coupling through Cu increased appreciably (~50%) for all Cu thicknesses and preserved its sign. This indicates that the exchange coupling in Cu interlayers originates in the electron spin transport properties (see chapter 5).

In spite of the fact that the band structures in Cu, Ag, and Au are similar, the behavior of the exchange coupling through Ag and Au is very different from that of Cu. In Ag the exchange coupling is ferromagnetic and rapidly decreases to zero at ~7ML and then it remains at this value for thicker Ag layers. The exchange coupling through Ag is temperature independent (see chapter 5).

The exchange coupling in Fe(001)/Au(001)/Fe(001) structures is ferromagnetic for Au interlayers thinner than 11ML and then it crosses over to a weak antiferromagnetic coupling. The maximum value for the antiferromagnetic coupling, -0.022 ergs/cm^2, is 10 times smaller than that for Cu interlayers. The exchange coupling in Fe/Au/Fe trilayers is temperature independent as observed in Fe/Ag/Fe.

The exchange coupling in Fe(001)/Pd(001)/Fe(001) trilayers is fascinating. In the thickness range from 4 to 12ML the exchange coupling between two Fe layers is ferromagnetic and weak. It exhibits an oscillatory

behavior with a period of ~4ML. The crossover from the ferromagnetic to weak antiferromagnetic coupling occurs at 12ML. The antiferromagnetic coupling shows a broad maximum at ~14ML. Pd interlayers thinner then 8ML exhibit a strong temperature dependence in the exchange coupling which indicates that the Pd atoms in these interlayers possess fluctuating magnetic moments. Pd interlayers thinner than 4ML are most likely ferromagnetic as a result of the proximity of the Fe.

This thesis has two major parts. In chapter 2 and 3 the growth studies are presented. In chapter 4 and 5 the magnetic properties of MBE grown structures are described. A brief outline of the thesis is as follows. Chapter 2 contains descriptions of the MBE facility. Emphasis is put on RHEED and AES. Chapter 3 describes the growth studies and the structural characterizations of Fe-Cu, Fe-Pd, Fe-Ag and Fe-Au structures. Chapter 4 introduces the phenomenological theory of exchange coupled ferromagnetic layers separated by a non magnetic interlayer. This theory was used to analyze the FMR measurements. In order to illuminate various aspect of this theory detailed calculations are presented for the perpendicular configuration in which the applied dc field is perpendicular to the surface of the film. For the parallel configuration which was used in FMR measurements only numerical calculations are shown. In chapter 5 the magnetic studies of Fe(001)/X(001), X(001)/Fe(001) bilayers and Fe(001)/X(001)/Fe(001) trilayers are presented. The main attention is paid to the exchange coupling between two ferromagnetic films separated by a nonmagnetic interlayer. These results are discussed in the context of current theoretical understanding.

Chapter 2

The Molecular Beam Epitaxy Facility

2.1 Introduction

Epitaxial growths of ultrathin metallic structures such as Fe(001)-Cu(001), Fe(001)-Pd(001), Fe(001)-Ag(001) and Fe(001)-Au(001) were carried out in a Physical Electronics Molecular Beam Epitaxy (Φ-400 MBE) system. Two surface analysis tools, Reflection High Energy Electron Diffraction (RHEED) and Auger Electron Spectroscopy (AES) were indispensable throughout the course of this work. This chapter provides a brief description of the MBE system and a detailed account of RHEED and AES.

2.2 An overview of the Molecular Beam Epitaxy system

Figure 2.1 shows a schematic diagram of the Φ-400 MBE system. Two interconnected chambers, the analysis and growth chambers, form the main parts of the MBE machine. The vacuum is maintained by an ion pump connected to the analysis chamber and a cryopump connected to the growth chamber. The background pressure of the system ($1 \cdot 10^{-10}$ Torr) is monitored by means of several ionization gauges. A small introductory chamber is used to load samples into the MBE system. The sample arm is used to move the sample between the introductory, analysis and growth chambers. A turbomolecular pump connected to the introductory chamber

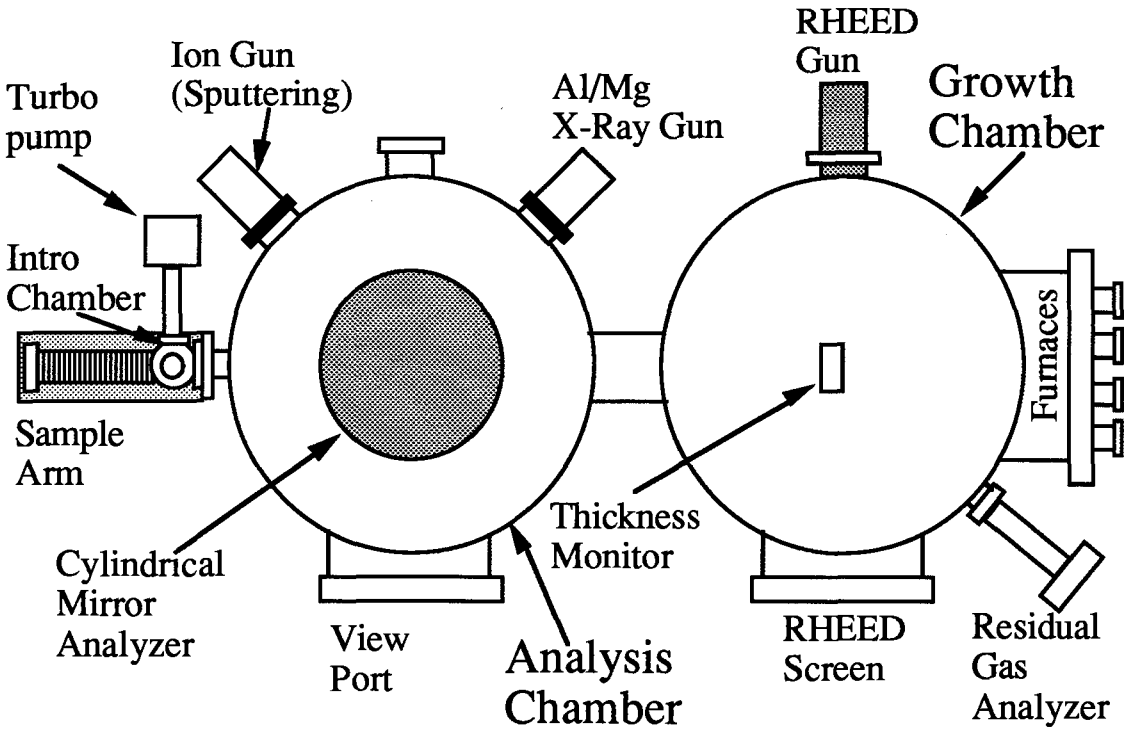

Fig. 2.1 Schematic drawing of the top view of the Φ-400 MBE facility.

maintains a pressure of approximately 10^{-6} Torr. Two cryosorption pumps are connected to the analysis chamber through a gold sealed valve. The cryosorption pumps are used after the MBE system is back filled with dry N_2 gas during maintenance.

The analysis chamber is used for substrate preparation and X-ray Photoemission (XPS) and Auger (AES) Electron Spectroscopies studies. This chamber houses an ion sputtering gun, a double pass Cylindrical Mirror Analyzer (CMA) and a Mg/Al X-ray source for XPS studies.
The ion sputtering gun (Φ model 04-191) is used to remove surface contamination from the sample substrate. During the sputtering process the MBE system is filled with argon, P ~$5 \cdot 10^{-5}$ Torr. Usually the argon ion beam, E=2keV, is rastered over an area of ~ 1 cm^2. A typical rate of sputtering is ~ 1 monolayer (ML) per minute. A double pass Cylindrical

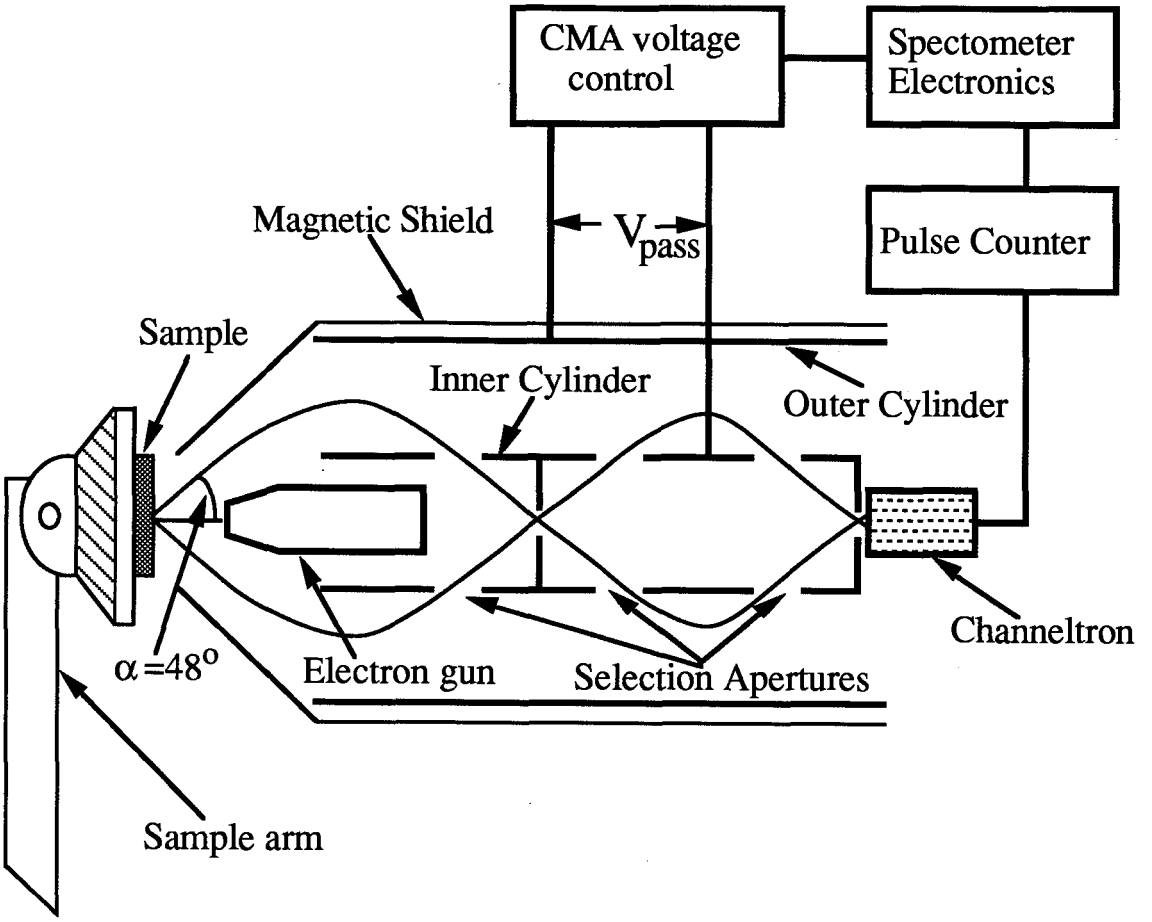

Fig. 2.2 Cross section of the double pass Cylindrical Mirror Analyzer.

Mirror Analyzer (Φ model 15-110), see Figure 2.2, is used for the detection of AES secondary electrons. The Auger electrons possess well defined kinetic energies and can be used to identify the elemental composition of the samples studied. Only electrons emitted at 48° with respect to the CMA axis are able to enter the detector (so called "acceptance angle"). The electrostatic voltage, V_{pass}, between the outer and inner cylinders selects electrons with an appropriate kinetic energy, $E_k=1.7 \cdot V_{pass}$. The electrostatic voltage, V_{pass}, is slightly modulated at 10kHz. The output of the channeltron is interconnected to a lock-in amplifier. The derivative of the secondary electron energy distribution, dN(E)/dE, is measured and displayed

on a X-Y recorder. The energy resolution, $\Delta E/E$ ~0.6-1.6%, is determined by the selection apertures. The AES electron gun (2-10keV) is mounted concentrically inside the CMA. The spatial resolution of the electron gun is ~ 0.2mm.

The growth chamber is used for film growth and RHEED studies. This chamber houses the RHEED unit, a thickness monitor, a quadruple mass spectrometer (also called the Residual Gas Analyzer or RGA) and Fe, Cu, Pd, Ag, Au furnaces placed inside a cryoshroud cooled by liquid nitrogen. Figure 2.3 shows a schematic diagram of the RHEED unit. The electron gun generates a 0.5-10keV beam of electrons (0.2mm in diameter). This beam is directed towards the surface of the specimen at a low angle of incidence ranging from 0^{o} to 5^{o}. Diffracted electrons can be observed on a phosphorescent screen. This screen is located 30.5cm away from the center of the sample. The intensities and profiles of diffraction features are measured by means of a photomultiplier tube equipped with a microscope objective lens and 50 μm diaphragm. A set of Helmholtz coils is used to deflect the diffracted electron beam in order to measure a RHEED pattern profile. The photomultiplier tube and Helmholtz coils are interfaced with a PC computer. The specular spot RHEED intensities were monitored during the growth and RHEED intensity oscillations were used to measure the thickness of the films deposited.

A crystal thickness monitor (Mathis model TM-100) was used to determine the overall thickness of the deposited layers. It consisted of two piezoelectric quartz crystals connected to a 6MHz resonant circuit. The thickness monitor electronics and quartz crystals are cooled by circulating water whose temperature is stabilized by a thermostat (Haake model E3). The quartz

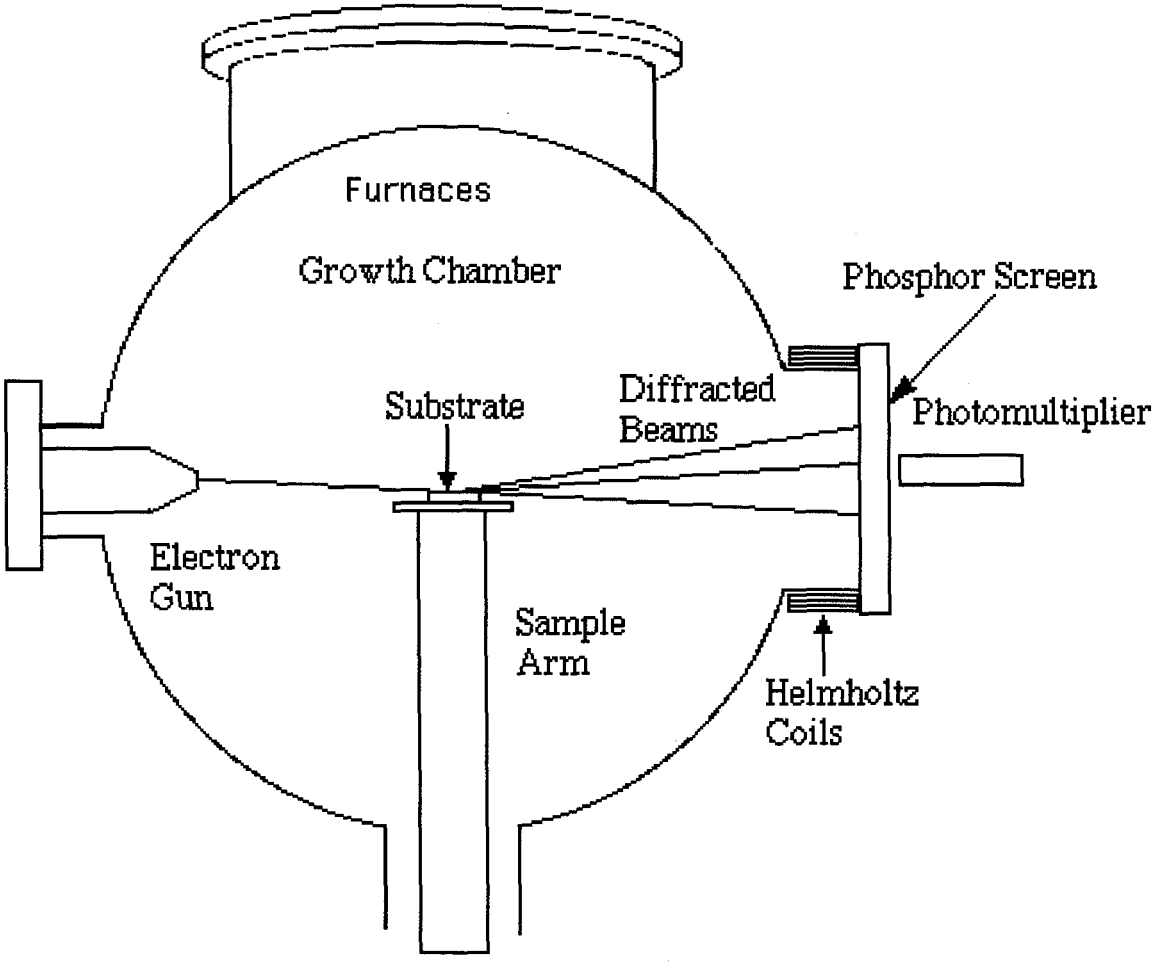

Fig. 2.3 A schematic diagram of the RHEED unit installed in the growth chamber of the MBE system.

crystal is placed 1 cm above the substrate. A careful calibration of the thickness monitor allows one to determine the film thickness with an accuracy better than ±0.5 monolayer (ML).

Four types of furnaces were used to create atomic beams. Cu was evaporated from a resistively heated tantalum boat, ~2cm long and ~0.4 cm wide. The ends of the tantalum boat were spot welded to tungsten support posts. The furnace was attached to a 2.75" UHV flange. A typical evaporation rate of 2ML/min was achieved by using 40 watts of power. Pd and some Fe films were evaporated from a tungsten filament. Pd and Fe fine wires (0.5mm)

were wound around a 0.5mm tungsten heating wire which was then bent into a spiral. The tungsten heating wire was spot welded to tungsten support posts attached to a 2.75" UHV mounting flange. A tantalum reflector improved the furnace efficiency. A power of 70 watts provided evaporation rates of ~1 ML/min. Most Fe layers discussed in this thesis were evaporated by using an Fe furnace suggested by Dr W.F. Egelhoff Jr. [2.1] from NIST. Figure 2.4 shows a schematic cross section of this furnace. A 2mm thick Fe plate was attached to the tantalum radiation shield. Radiation from a tungsten filament, see Figure 2.4, heated the Fe plate. A typical evaporation rate of ~1 ML/min was reached by using 130 Watts of power. The uniformity of flux was excellent. Ag and Au were evaporated from pyrolitic boron nitride furnaces which were purchased from Perkin-Elmer (Φ model 04-410). Crucibles heated to ~ 1000 ^{o}C provided a constant flux of atoms with flux rates at the substrate of 0.5 and 1 ML/min for Au and Ag furnaces respectively. All of

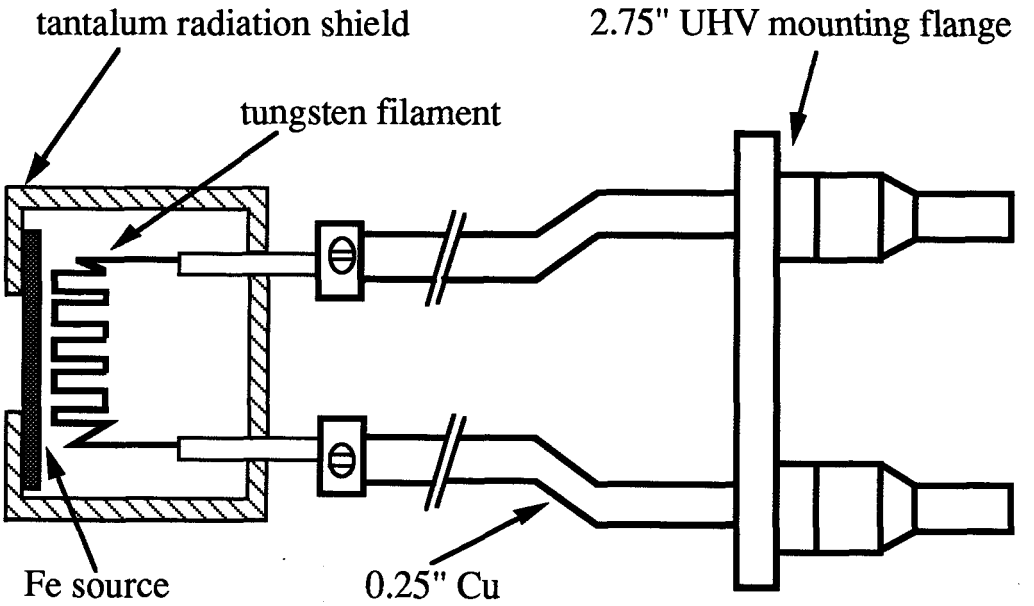

Fig. 2.4 A schematic cross section of the furnace used for Fe evaporation. Details of the design were obtained due to courtesy of Dr. W.F. Egelhoff Jr. from the National Institute of Standards and Technology in Gaithersburg.

the above mentioned furnaces were surrounded by a cryoshroud which was cooled by liquid nitrogen. This kept the vacuum in the low 10^{-10} Torr range during the growth. The distance between the substrate and furnaces was ~ 25cm. The flux of atoms from the furnaces was initiated and terminated by pneumatically operated shutters.

The substrate was mounted on a molybdenum holder. The substrate holder is screwed to the transfer rod manipulator end. This procedure is carried out in the introductory chamber which was back-filled with flowing dry N_2. After the sample was mounted, the introductory chamber was sealed and pumped out by a turbomolecular pump to the low 10^{-6} Torr range. An electric motor drove the sample arm through a pneumatic valve assembly which connects the introductory and analysis chambers. A sequence of annealing and sputtering cycles was performed to clean the substrate and to prepare the substrate surface with large atomically flat terraces. Substrate temperatures up to 800 ^{o}C can be achieved by a substrate heater located on the back side of the Mo holder. The substrate temperature is monitored by a chromel-alumel thermocouple. After this procedure the substrate was transferred to the growth chamber. After the growth and RHEED studies the sample arm was transferred back to the introductory chamber and the prepared film was taken out of the MBE system for further magnetic studies.

2.3 Auger Electron Spectroscopy

Auger Electron Spectroscopy (AES) was used to monitor both the surface contamination and the quality of coverage of the grown metallic layers. AES is based on an Auger electron emission occurring after a surface is bombarded with primary high energy electrons. Figure 2.5 shows the

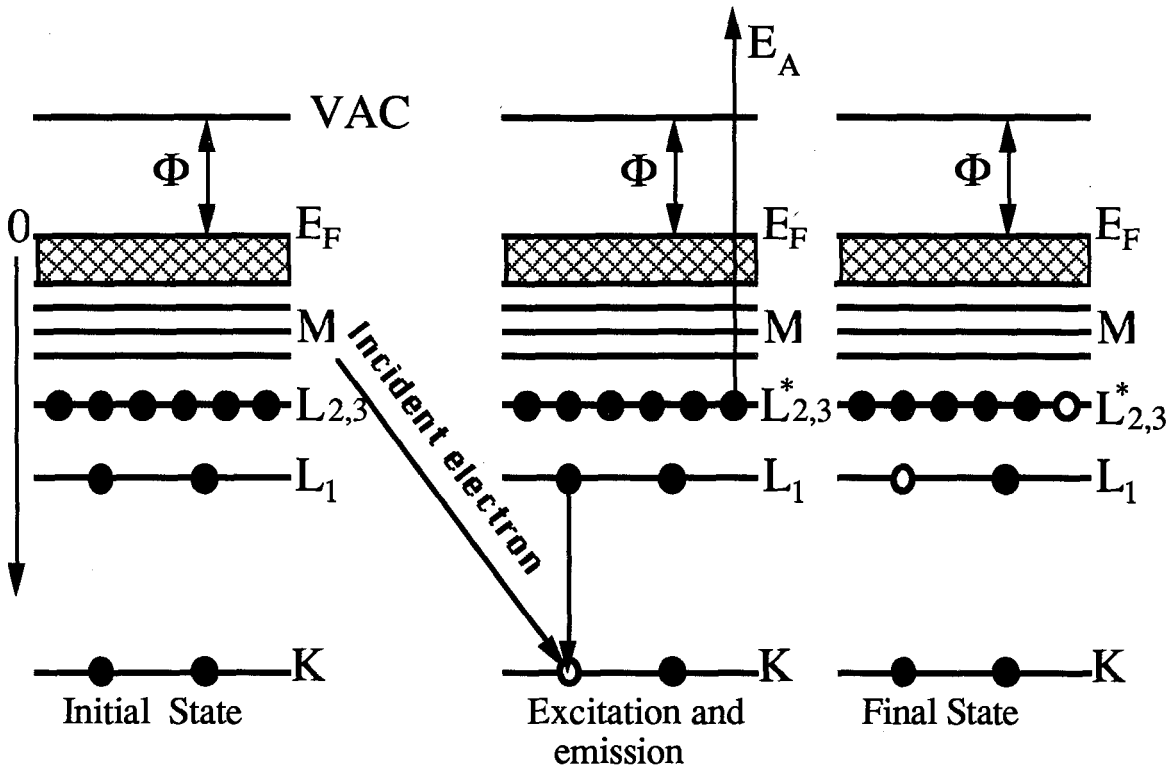

Fig. 2.5 Diagram of the sequence of events for an Auger process. An incident electron creates a hole in the K level. The electron from an L_1 level relaxes into the vacant state, giving part of it's energy to another electron which is ejected from the atom. The kinetic energy of the ejected Auger electron is very well defined and is used for identification purposes.

sequence of events for an Auger process following the ionization of core levels. The incoming primary electron (from CMA) with a sufficiently high kinetic energy can ionize an appropriate atom, creating a hole in the K level. The ionized atom relaxes by filling the hole with an electron from the outer level, e.g. L_1. The energy difference (E_K-E_L) becomes available and can be used by the atom in two different ways. Either a characteristic X-ray photon can be emitted (X-ray fluorescence) or another electron in the same level or in a more shallow level can be ejected from the atom (Auger process). The probability of relaxation by an Auger process is strongly dominant over that of X-ray fluorescence for lighter elements [2.2]. The energy of the ejected

Auger electron for a particular Auger line is

$$E_{KL_1L_{23}} = E_K - E_{L_1} - E^*_{L_{23}}$$

where E_K is the binding energy of the K atomic energy level and $E^*_{L_{23}}$ is the binding energy of the L_{23} level in the presence of a hole in level L_1. The Auger electron energy expressed by the above equation depends only on the atomic energy levels. Therefore each element possesses a unique set of Auger energies. AES measurements provide element identification immediately by comparing the measured Auger peak energies with published standard spectra, e.g. see Davis et al. [2.3]. The Auger transitions are labeled according to an old historical X-ray notation of atomic levels, where the atomic states with n=1,2,3,4,.... are denoted by K,L,M,N,... and V for valence electrons. Different Auger series, such as KLL, KLM, KMM, LLM,..., KLV, KVV,... may be measured. Relative intensities of different Auger transitions within the same element, or the same Auger transition in different elements, show large variations. Theoretical calculation have not been able to explain these variations yet. Therefore published Auger handbooks (e.g. [2.3]) are used to determine the Auger peak positions and intensities for different elements.

Auger electrons strongly interact with solids. An Auger electron which originates deep in the sample is frequently inelastically scattered and no longer possesses a well defined energy. A characteristic length, called the inelastic mean free path (IMFP), λ, is introduced. The flux of unscattered Auger electrons decays exponentially as a function of the distance λ from the point of origin. The IMFP λ can be approximated using the formula given by Seah and Dench [2.4]

$$\lambda = 0.41 \cdot \sqrt{\frac{E_M \cdot A_M}{\rho_M N}} \qquad (2.1)$$

where ρ_M is the density (in kg/m^3), N is Avogadro's number, A_M is the mean atomic weight, E_M is the Auger kinetic energy in keV and λ is in nanometers. The values of λ are in the range of 2 - 10 atomic monolayers, making the AES spectroscopy sensitive only to surfaces. The "escape depth", δ_e, is the distance over which 95% of Auger electrons will be inelastically scattered before leaving sample. It is defined as

$$\delta_e = 3 \lambda \cos\Theta$$

where Θ is the angle of emission from the surface normal. The angle of emission is related to the angle of acceptance of the CMA analyzer and $\Theta=48^o$ if the sample normal is parallel with the CMA axis.

AES can be used to monitor the uniformity of the grown overlayers. For a well defined layer-by-layer growth (Frank - van der Merwe model) the intensity of the Auger signal from the substrate will decrease exponentially with an increasing overlayer thickness. For the film normal parallel with the CMA axis it is described by

$$I(d) = I(0) \exp\left(\frac{-d}{\lambda_s \cos 48^o}\right)$$

where d is the overlayer thickness, λ_s is the IMFP of the substrate Auger electron, 48^o is the CMA acceptance angle. On the other hand the overlayer AES intensity increases with an increasing layer thickness and can be described by

$$I(d) = I(\infty)\left(1 - \exp\left(\frac{-d}{\lambda_l \cos 48^o}\right)\right)$$

where λ_l is the IMFP and $I(\infty)$ is the bulk intensity of the measured overlayer Auger peak.

2.4 Reflection High Energy Electron Diffraction.

Reflection High Energy Electron Diffraction (RHEED) was used to monitor the growth. The unique sensitivity of RHEED to the sample surface allows one to characterize the surface structure at every stage of the growth process. RHEED can characterize the substrate preparation; features such as the density of atomic steps (average terrace size) and superlattice reconstructions are clearly visible in RHEED patterns. The RHEED glancing angle scattering geometry allows one to monitor continuously the growth process. The RHEED intensity oscillations indicate the mode of growth and can be used to determine the film thickness during the growth. RHEED patterns reflect the crystallographic structure and morphology of grown films. Despite a wide use of RHEED in MBE a full theoretical treatment has not been accomplished yet. However, a simple kinematic theory provides a qualitative picture sufficient to interpret the main RHEED pattern features. Ewald's construction and RHEED intensity oscillations will be discussed below in some detail. A more complete account of RHEED can be found in the thesis by P.R. Pukite [2.5] and by S.T. Purcell [2.6] and in the review article by Bauer [2.7].

A 10 keV electron beam impinges on the sample at a very shallow angle, typically 1^{o}. In order to penetrate to a depth of 1ML the primary beam electrons have to traverse a distance of ~100 Å inside the top atomic layer. However the IMFP for 10 keV is ~50Å. This indicates that the RHEED probe is sensitive only to the top most atomic layers.

Figure 2.6 shows the 2-D net of scattering centers (atoms). Each point of the lattice is defined by $\mathbf{R} = n\mathbf{a} + p\mathbf{b}$ in the X-Y plane, where n, p are integers and **a**, **b** are basis vectors. This construction is periodic in the X-Y

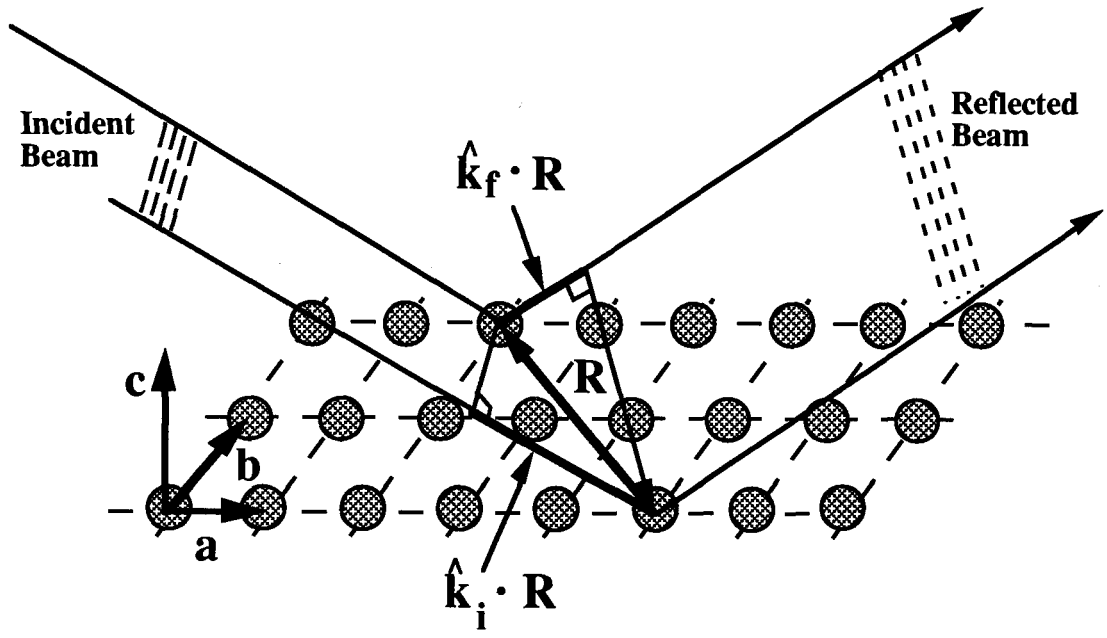

Fig. 2.6 Laue construction for the 2-dimensional scattering centers.

plane. In the z direction, normal to the lattice surface, only one scattering center is present (for a given **R**) and can be approximated by a delta function. The Fourier transform determines the reciprocal lattice. This reciprocal lattice is discrete and periodic in X-Y plane with basis vectors given by

$$\mathbf{A} = 2\pi \frac{\mathbf{b} \times \hat{\mathbf{c}}}{|\mathbf{a} \times \mathbf{b}|} \qquad \mathbf{B} = 2\pi \frac{\hat{\mathbf{c}} \times \mathbf{a}}{|\mathbf{a} \times \mathbf{b}|}$$

where $\hat{\mathbf{c}}$ is the normal unit vector. The Fourier transform of a delta function (in z direction) is a constant value. Therefore the reciprocal lattice is represented by a set of rods perpendicular to the film surface.

Using the Bragg picture (see Figure 2.6) constructive interference between waves reflected from different points requires

$$\mathbf{k_f} = \mathbf{k_i} + \mathbf{G} \quad \text{and} \quad |\mathbf{k_i}| = |\mathbf{k_f}|.$$

where $\mathbf{k_i}$, $\mathbf{k_f}$ are the incident and reflected electron wavevectors respectively and **G** is a reciprocal lattice vector. The **G** vector can be written as

$$\mathbf{G} = h\mathbf{A} + k\mathbf{B} + \mathbf{C}$$

where h, k are integers and **C** is a continuous vector in the z direction.

Ewald's construction, shown in Figure 2.7, is very useful in the interpretation of RHEED results. A set of rods on the right-hand side of this figure represents the 2-D reciprocal lattice. The vector $\mathbf{k}_i$ is drawn in the direction of the incident electron beam and it is terminated at the origin of the reciprocal lattice space. The Ewald's sphere of radius equal to $|\mathbf{k}_i| = 2\pi/\lambda$ has its center at the origin of $\mathbf{k}_i$ and intercepts reciprocal lattice rods. Scattering vectors $\mathbf{k}_f$ are determined by the intersection of the Ewald sphere with reciprocal rods. The diffracted beams hit a phosphorescent screen and generates the observed RHEED patterns. RHEED patterns exhibit the following features: (1) a bright spot from the straight through beam if part of it missed the surface of the sample, (2) the shadow edge from inelastically scattered electrons which form a brighter background in one half of the screen, (3) the bright "specular spot" which originates from the {00} reciprocal rod. (4) additional spots created by diffraction beams with other components of the reciprocal vectors **G**. Sharp diffraction spots distributed along a circle are observed for perfect surfaces such as for an Fe whisker, see Figure 2.8a.

For cubic structures the reciprocal lattice rods corresponding to the (001) surface form a square mesh with an in-plane k vector separation of $2\pi/a$ and $2\sqrt{2}\pi/a$ for bcc or fcc packing respectively, where a is the lattice constant of the cubic crystal. The separation between diffraction spots can be used to determine the in-plane lattice constant.

The surfaces of silver single crystal substrates used throughout the course of this work are not as perfect as those on iron whiskers. Figure 2.8b

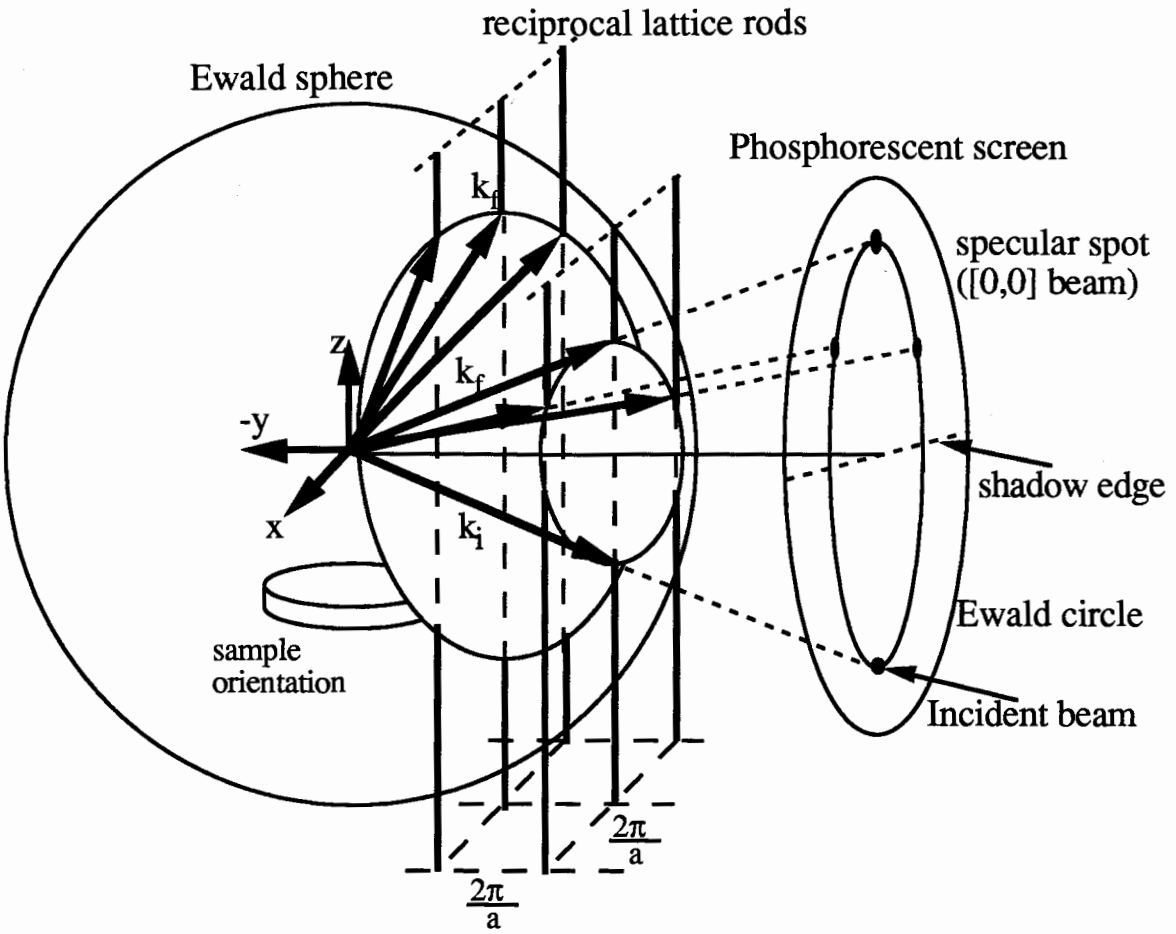

Fig. 2.7 Ewald's construction of 2-dimensional diffraction.

shows a RHEED pattern of a well prepared single crystal of silver. Instead of sharp spots a set of streaks is visible. An average terrace size can be extracted from this pattern. A typical RHEED pattern from a well prepared silver single crystal leads to W ~ 300 atoms/terrace, where W is the average number of atoms across the terrace.

The silver crystals have a mosaic spread ($<0.2^{o}$). The mosaic blocks have their {001} axes randomly misoriented with respect to the surface normal. If the surface of each mosaic block has a range of W's this distribution of terrace sizes cause the reciprocal lattice rods to possess a finite width, which would result in the spots becoming elongated perpendicular to

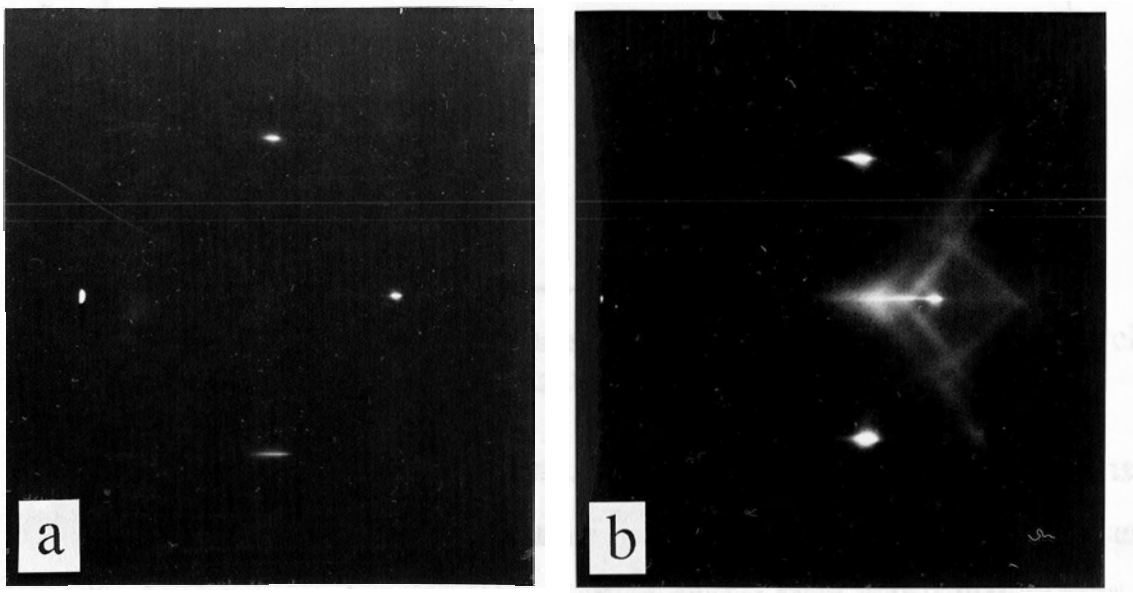

Fig. 2.8 RHEED patterns obtained from: (a) (110) azimuth of an Fe(001) whisker facet. This pattern indicates an average terrace size larger than 2000-3000Å (instrumentally limited) (b) (100) azimuth of a well prepared Ag(001) single crystal substrate. The straight through beam will always appear as a spot on the left side of the photographs.

the surface. The sum of intensities from differently oriented mosaic blocks will also lead to elongated streaks. A third effect in RHEED is that the electron beam is convergent. This gives a range of transverse k vectors which broaden the streaks.

For surfaces with large terraces for which atoms are correlated over large distances the interference of electron beams scattered from different islands affects the RHEED pattern. For such a case Lent and Cohen [2.8] introduced a model of the surface with finite number of vertical atomic levels, see Figure 2.9. The correlation function C(**u**) describes the probability of finding two scattering centers separated by a vector **u** on the terrace surface. The Fourier transform of the correlation function provides

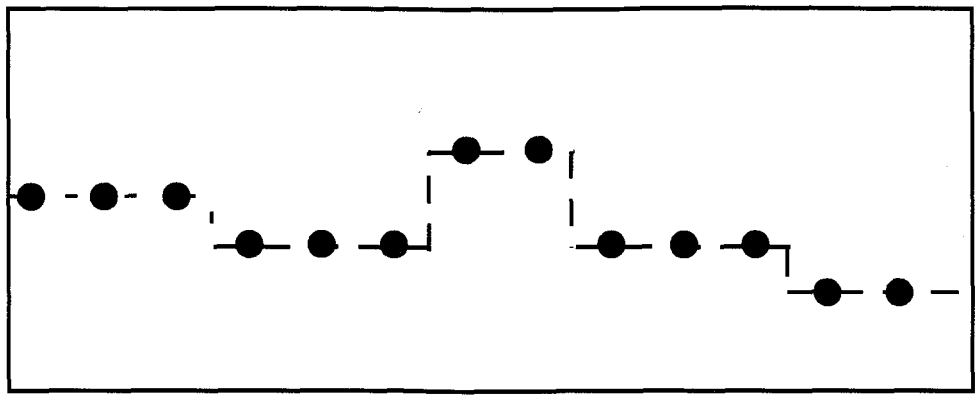

Fig. 2.9 Schematic illustration of the surface cross section. The closed circle represent the positions of surface scatterers.

the distribution of diffracted intensity. The profiles of the diffracted beams from such a surface exhibits two main features; (1) a central spike that arises from the long range coherence of the lattice, that is from atoms that occupy the correct lattice sites, (2) a step-broadened part, which could be smoothly varying or have structure arising from the finite extent of the correlation function. The relative contribution of the two parts is a function of both coverage and the momentum transfer perpendicular to the surface. The width of the broadened parts reflects the mean value of a terrace size.

The length of RHEED streaks, for a crystal with a small mosaic spread, is affected by the distribution of atomic terraces along the direction of the primary electron beam. Figure 2.10 shows a geometrical construction which explains the observed effect. The Ewald sphere intersects the thickened reciprocal lattice rods along a portion of their length creating a set of long RHEED streaks. The thickness of the reciprocal rod is $\delta K=2\pi/(aW)$, where W is the average number of atoms across the terrace. From geometrical considerations the angular spread $\delta\Theta$ is given by $\delta\Theta=\delta K/(k_i \sin\Theta_i)$. The length of the streak is $L=\delta\Theta k_i$. The distance between the incoming beam and the shadow edge is equal $D=\Theta_i k_i$. Therefore

$$W = \frac{D}{L\Theta_i \sin\Theta_i}$$

determines the average number of atoms on a terrace. The size of the average terrace can also be extracted by an analogous argument from a measurement of the streak profile. Such an interpretation of RHEED streaks is correct only for surfaces with small terraces randomly displaced from one another.

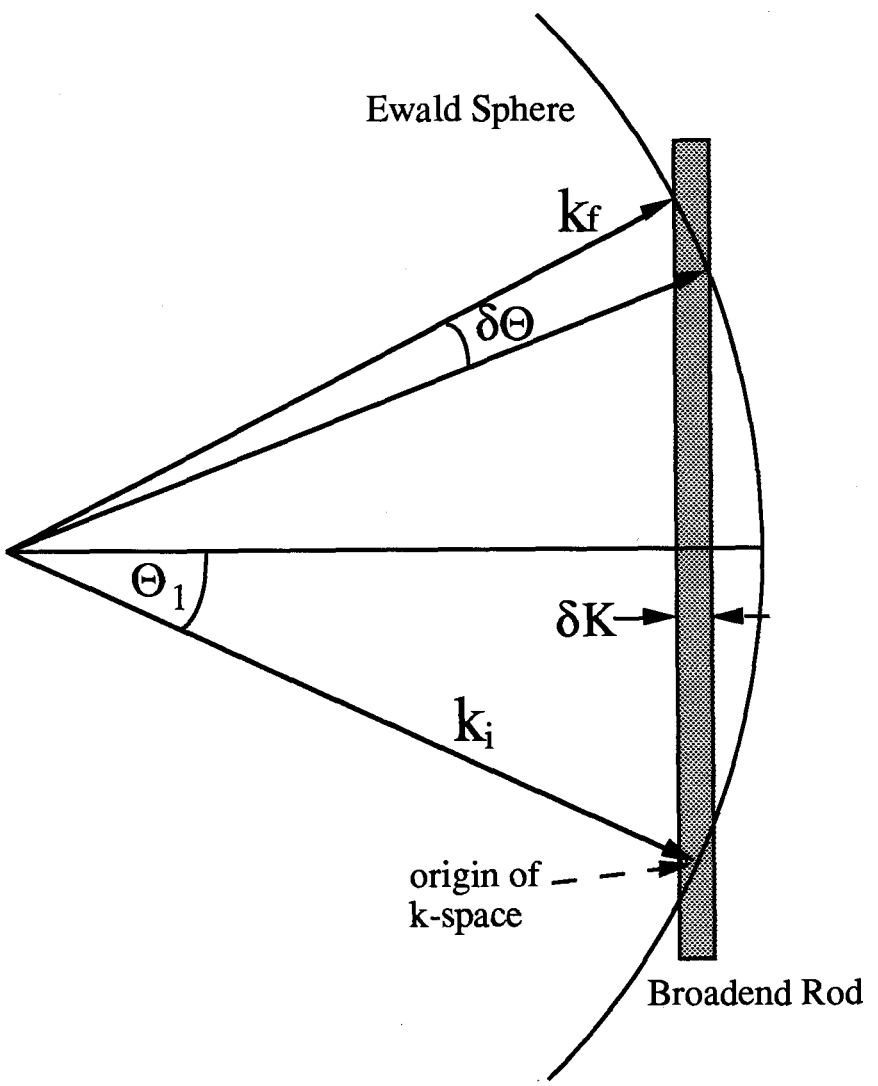

Fig. 2.10 Ewald's construction for the specular spot on the real crystal. The reciprocal lattice rod possesses a finite width δK.

Monitoring the RHEED patterns during a growth process provides valuable information concerning the type of growth and can also be used to determine accurately the film thickness. The intensity measurement of the specular spot can exhibit an oscillatory behavior during the growth process indicating layer-by-layer growth.

Neave et al. [2.9] suggested a qualitative model in which the RHEED oscillations are related to changes in the surface roughness during deposition. Prior to evaporation the electron beam is reflected from a perfectly flat surface resulting in a high intensity of specular spot. At the start of deposition the adatoms condense on the surface forming small, 1ML thick, islands thus introducing atomic steps on the surface which increases the diffuse scattering. The intensity of the reflected beam will decrease as the roughness increases. Statistically, the maximum number of steps (maximum roughness) can be expected for 1/2 ML. At this point the specular spot intensity reaches a minimum. As the deposition continues the islands merge which decreases the number of surface steps. The surface again becomes more smooth on an atomic scale and the reflectivity of the electron beam increases. This repetitive process of roughness variations results in an oscillatory behavior of the RHEED intensity. RHEED oscillations are observed when the growth proceeds in a near layer-by-layer mode.

Van Hove et al. [2.10] suggested a very simple model based on the kinematic approximation in which the intensity of the diffracted electron beam also exhibits oscillations. In this model electrons are scattered only from the two surface levels, z=0 and z=d, see Figure 2.11. The coverage of the top atomic layer, C, changes during deposition, the lower layer is completely full. Electrons reflected from the the top, partially filled layer

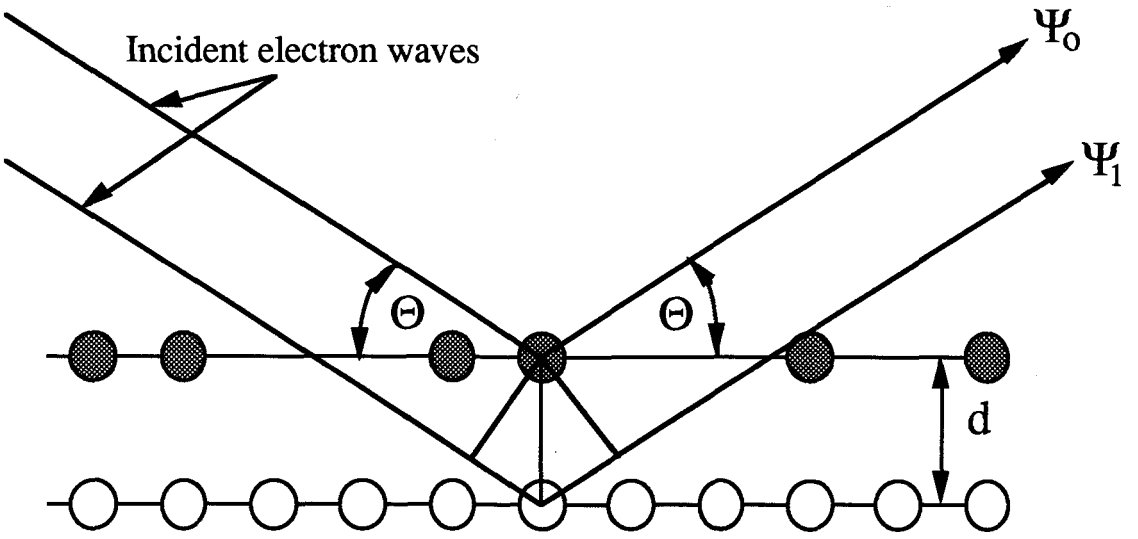

Fig. 2.11 A schematic diagram of the two top atomic layers used to model RHEED oscillation in simple kinematic approximation.

(z=d) will have a phase difference $\delta\phi$ with respect to those which are reflected from the uncovered part of the fully filled layer (z=0). The electron wave function Ψ_o and Ψ_1 for the electron scattered from the top and bottom atomic layers will be proportional to C and (1-C)exp(-i$\delta\phi$) respectively. The intensity of the specular spot is given by:

$$I = |\Psi_o + \Psi_1|^2 = C^2 + (1-C)^2 + 2C(1-C)\cos(\delta\phi)$$

where $\delta\phi$ is equal to $2|k_i|d\sin\Theta_i$. Figure 2.12 shows the intensity of the RHEED specular spot as a function of time for C linearly increasing between 0 and 1. This is a perfect layer-by layer growth. The condition $\delta\phi = 2\pi, 4\pi$ .. at which the amplitude of the oscillations is equal to 0, is called the first , second, etc. Bragg condition and the condition $\delta\phi = \pi, 3\pi, 5\pi$, ... is called the first, second, etc. anti-Bragg condition. For the arbitrary value of $\delta\phi$ the intensity oscillations will not reach zero at 50% coverage. This model can be generalized for the case where additional layers start to form before the

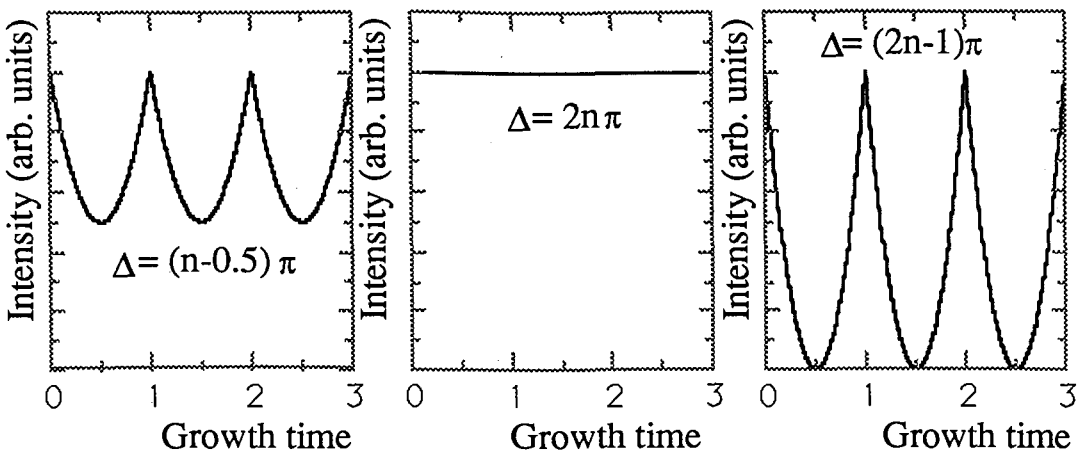

Fig. 2.12 The intensity of the RHEED specular spot as a function of time (coverage) in simple model postulated by Van Hove et al. [2.10].

that the RHEED oscillations are wiped out if there are more than three atomic layers participating significantly in the growth at any given time. In some cases when no RHEED oscillations were observed the RHEED patterns clearly showed 3 dimensional features indicating that the growth did not proceed in a layer-by-layer fashion. It is worth while to point out that the RHEED intensity oscillations do not represent a perfect layer-by-layer growth. The next layer can be nucleated before the previous one is filled.

Chapter 3

Growth and structural characterization of ultrathin metallic structures

3.1 Introduction

In this chapter studies of growth and structural characterizations of the Fe-Cu, Fe-Pd, Fe-Ag and Fe-Au structures are reported. All structures were grown on Ag(001) single crystal substrates whose (001) axis was parallel with the normal to the specimen surface within 0.2^{o}. Magnetic studies were carried out on Fe(001)/X(001), X(001)/Fe(001) bilayers and Fe(001)/X(001)/Fe(001) trilayer structures where X(001) denotes a layer of metastable bcc Cu(001), distorted fcc Pd(001), fcc Ag(001) and fcc Au(001). All the structures studied were capped with 20ML of epitaxial Au(001) which protected the films from oxidation when exposed to ambient conditions for further FMR and SMOKE studies.

Subsection 3.2 contains a brief review of the main concepts describing the epitaxial growth and introduces the nomenclature used in the literature. Subsection 3.3 provides a description of the Ag substrate preparation. The growth studies of the Fe-Cu, Fe-Pd, Fe-Ag, and Fe-Au structures are described in the subsection 3.4. The characterization of growth was based on RHEED patterns, RHEED intensity oscillations and AES peak intensity measurements.

3.2 Surface structure and epitaxial growth

To achieve an epitaxial growth many factors have to be satisfied. Some of them, such as a rate of deposition or the substrate temperature are relatively easy to control. Others, such as the smoothness of the substrate surface or surface defects are more difficult to control. Finally there are factors, such as the surface free energy of adatoms and the free energy of substrate atoms which are intrinsic material properties and are beyond our control.

Figure 3.1 shows a schematic picture of a growth process. Incoming atoms arrive at a rate R (# of atoms/cm^2 s) and are accommodated on the substrate. With the substrate held at room temperature the sticking coefficient is near unity for metallic elements. The population of single atoms builds up. The atoms diffuse over the substrate surface. This can be described by a temperature dependent diffusion coefficient D ($cm^{-2}\,s^{-1}$). Small clusters start to form and become stable at a certain "critical" size (e.g. their growth is more probable than their decay). Single atoms can diffuse across the substrate to join a stable cluster, or they can impinge directly on the growing cluster and become incorporated. As the growth continues the stable clusters coalesce and fill the atomic layer. However additional small clusters can be formed on the top of the growing clusters before they coalesce into a single atomic layer.

The mode of nucleation and the initial growth of epitaxial layers is strongly governed by the bonding between the deposited atoms and the substrate. The surface and interfacial free energies can be employed in a simplified description of the initial phase of layer formation. If we assume that the deposited adatoms form a hemispherical cap, then a relation

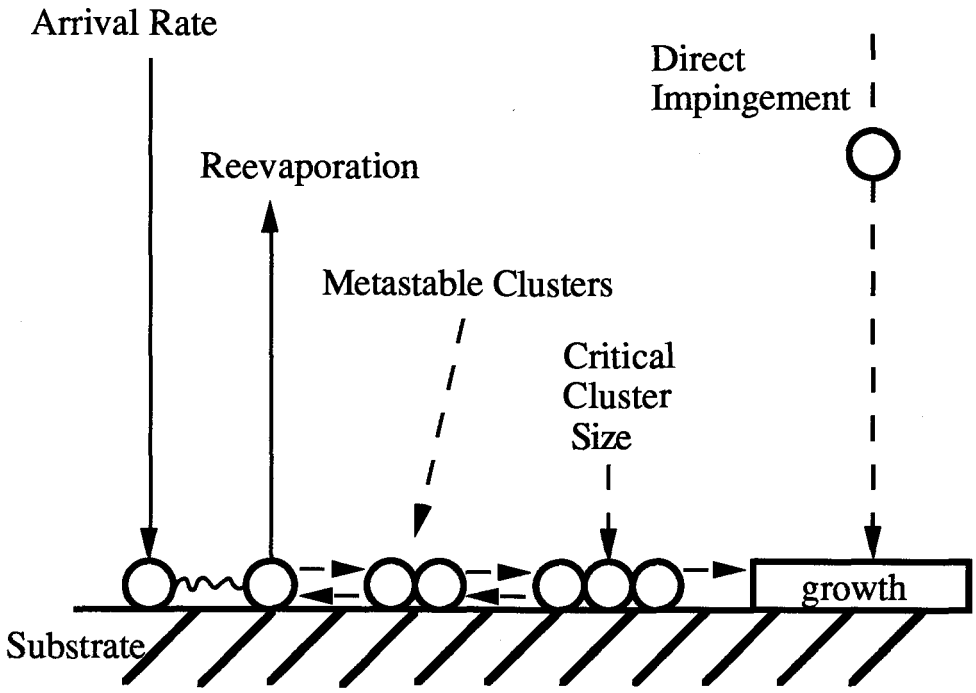

Fig. 3.1 Nucleation and growth of epitaxial films on a single crystal substrate.

$$\gamma_{sv} = \gamma_{as} + \gamma_{av} \cos\theta$$

has to be satisfied, where γ_{sv}, γ_{as} and γ_{av} are the free energies of the substrate - vapor, adatoms - substrate and adatoms - vapor interfaces and θ is the contact angle. E. Bauer [3.1] introduced three basic categories of the initial film formation (see Figure 3.2):

1. A layer-by-layer mode of growth (Frank - van der Merwe model) occurs when $\theta=0$ and $\gamma_{sv} = \gamma_{as} + \gamma_{av}$. Clusters, one atom in height, are nucleated during deposition. Clusters coalesce and form a single atomic layer. After the first layer is completed nucleation starts again and the whole process repeats itself (see Figure 3.2a).
2. The island mode of growth (Vollmer - Weber model) occurs when $\gamma_{sv} < \gamma_{as} + \gamma_{av}$. Add atoms form 3-dimensional clusters which eventually agglomerate into a continuous film with a significant surface roughness,

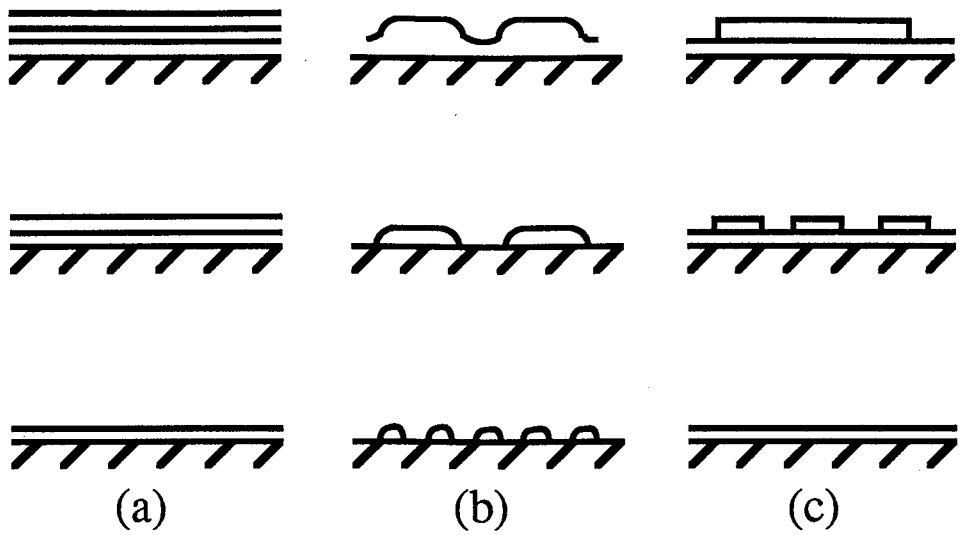

Fig. 3.2 Three forms of epitaxial growth : (a) layer-by-layer growth (Frank - van der Merwe mode); (b) formation and growth by 3-dimensional clusters (Vollmer-Weber model); (c) initial formation of tightly bound layers followed by 3D growth (Stranski-Krastanov model)

see Figure 3.2b.

3. The transition layer/islands mode of growth (Stranski-Krastanov model) occurs when $\gamma_{sv} > \gamma_{as} + \gamma_{av}$. Initially the strong interaction between add atoms and the substrate compared to that among add atoms themselves favours a layer formation. Eventually discrete 3-dimensional clusters may formed at a later stage, as depicted in Figure 3.2c.

The above mentioned classification is over simplified and purely based on thermodynamics. It does not take into account such factors as the smoothness of the substrate surface, the density of steps in the substrate surface, the number of defects on the surface and the lattice mismatch between the substrate and growing film. These factors strongly affect the film quality and the mode of growth. The above discussion indicates only qualitatively the initial stages of growth.

The growth of our structures was carried out under non equilibrium conditions and was mainly governed by the heat of condensation and

subsequent diffusion of the adatoms on the surface. In our studies the RHEED oscillations, RHEED patterns and the AES peak intensity measurements were used to characterize the mode of growth and the quality of the grown layers.

3.3 Preparation of silver substrates

Single crystals of silver were used as substrates for all the structures presented in this thesis. Seven disk-shaped substrates, called Ag G1, ..., Ag G7, were spark cut from a boule having a small mosaic spread ($<0.2^{o}$) supplied by Monocrystals Co., Ohio. Slices were cut from the boule which were 15 mm in diameter and 3.5 mm thick. The Ag crystals were aligned to within $\pm 0.2^{o}$ of the (001) plane (so called "singular" cuts). Such careful orientation was necessary to create relatively big terraces, on average 300 atoms across a terrace. Two, 1 mm deep, slots were cut on the side of each disk in order to mount the substrates on the end of the sample arm without obstructing their surface during the deposition. The preparation process was carried out in two stages; one stage outside the UHV system and the second stage in UHV.

The substrates were mounted on a polishing jig with a good electric contact (~1Ω) between the Ag substrate and the jig. A standard reflecting Laue camera was used to accurately orient the Ag substrate. The polishing jig was part of the goniometer. The distance 12.5 cm between the crystal and X-ray film insured very good angular resolution. The degree of misalignment was determined by the accuracy with which the Laue patterns could be marked and by the mosaic spread of the crystals. Mechanical polishing was carried out on nylon pads (B1031 from Micro Metallurgical

Ltd., Ontario) with a slurry consisting of Al_2O_3 and water. Three steps of mechanical polishing were performed, each with a different particle size (9, 5, and 1 μm). The first two steps took approximately 30 minutes each and the last one with 1 μm Al_2O_3 particles required only 5 to 10 minute. Each mechanical polishing step produced a progressively shinier surface and removed all damage from the previous polishing. After mechanical polishing the Ag crystal possessed a flat, well oriented surface with only tiny scratches left. Approximately 5 minutes of electrolytic polishing was carried out in a cyanide-free solution [3.2] which produced a strain-free and a smooth mirror like surface. The Ag substrate was then carefully cleaned with acetone and was dryed by a flow of N_2. Special care was taken to remove a low melting point resinous cement (Crystalbond^{TM}) which was used to hold the Ag crystal on the aluminum base of the polishing jig. A more detailed description of the mechanical and electrolytic polishing can be found in the thesis by Ken Urquhart [3.3].

After electrolytic polishing the Ag substrate was placed in the introductory chamber of the MBE system and left there for a few hours to outgas. The AES measurements revealed that the substrate surface was heavily contaminated with S and sometimes with Cl. Therefore, at room temperature, the Ag crystal was sputtered for ~ 1 hour with a beam of 2keV Ar^+ ions and with a sputtering rate of ~1ML/minute. The Ar gas was supplied to the analysis chamber through a needle valve to a pressure of $4 \cdot 10^{-5}$ Torr. AES was used to monitor the sputtering process to insure that all contaminants were removed. However such treatment creates significant surface damage. Annealing at elevated temperatures tends to restore the surface quality but allows impurities to resurface from the bulk Ag (for

example Sb). A proper balance between sputtering and annealing has to be achieved in order to produce the best quality of Ag substrates. The crystals were annealed at 550°C for 2 hours and then sputtered at this temperature for 30-min. at an Ar pressure of $2 \cdot 10^{-5}$ Torr. The substrate temperature was then decreased by 50°C and sputtered for ~30 min. at the same pressure. This process of reducing the temperature by 50°C and subsequent sputtering at each temperature was repeated until 350°C was reached. At 350°C the substrate was not sputtered anymore, but it was annealed for 10 min. and then cooled down to room temperature. The Ag substrate prepared in this way showed no impurities detectable by AES. The RHEED patterns exhibited sharp and short streaks with an easily identifiable specular spot, see Figure 3.3.

Only Ag single crystals prepared in the above described manner could be used to grow high quality single crystal structures of bcc Fe(001), bcc metastable Cu(001), fcc metastable Pd(001), fcc Ag(001) and fcc Au(001). A significant departure from this procedure resulted in a lack of layer by layer growth and led to 3 dimensional (3-D) structures [3.4].

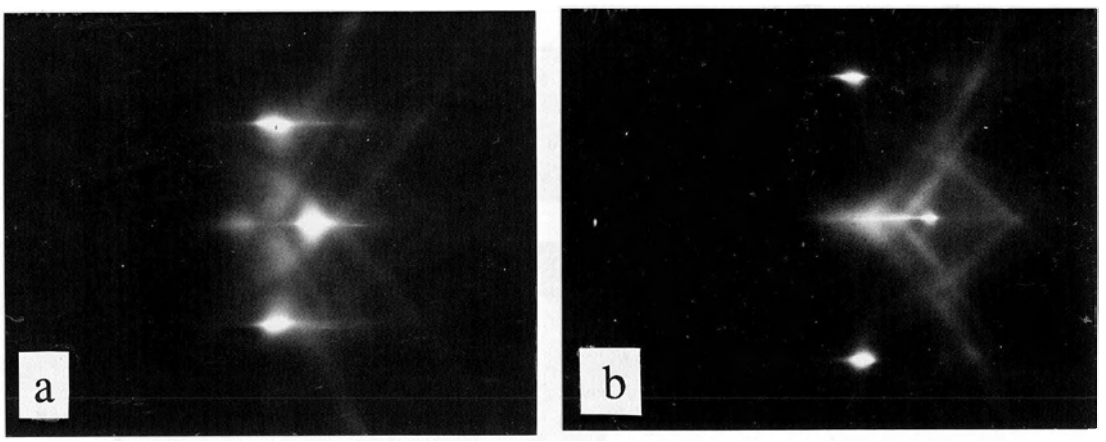

Fig. 3.3 RHEED patterns from a well prepared Ag(001) single crystal substrate. The incident electron beam (10keV) is along the Ag{100} and the Ag{110} azimuths in (a) and (b) respectively.

3.4 The results of growth studies of the Fe-Cu, Fe-Pd, Fe-Ag, and Fe-Au structures

Studies of the exchange magnetic coupling between two ferromagnetic layers separated by a non magnetic interlayer were carried out on trilayer structures. Figure 3.4 shows a schematic diagram of the trilayer structure. The first bcc Fe(001) layer was grown on a Ag(001) single crystal substrate. Cu, Pd, Ag, or Au interlayers oriented along (001) were grown on the first Fe(001) layer. The second bcc Fe(001) layer was grown on top of the non magnetic interlayer. The whole structure was covered by an epitaxial Au(001) layer 20ML thick before it was exposed to ambient conditions for FMR and SMOKE measurements. The bilayer structures, with the same interfaces as used in the trilayer structures, were employed to determine the magnetic properties of the individual Fe layers.

Fcc Ag(001) templates were used because their 4-fold hollow surface is very closely matched to the bcc Fe(001) lattice, see Figure 3.5. The in-plane distance between 4-fold hollow sites is equal to 2.88Å which is very close to

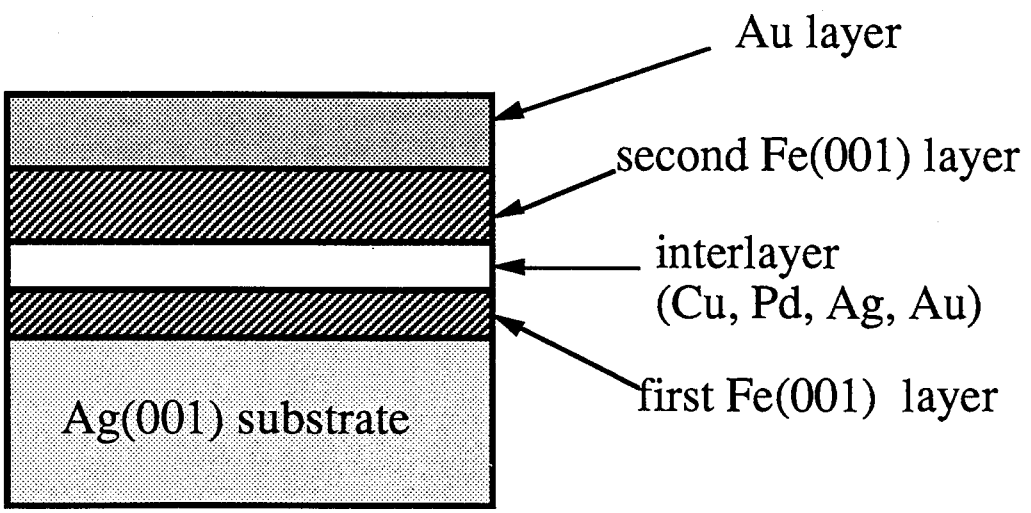

Fig. 3.4 A schematic diagram of the trilayer structure employed in magnetic studies.

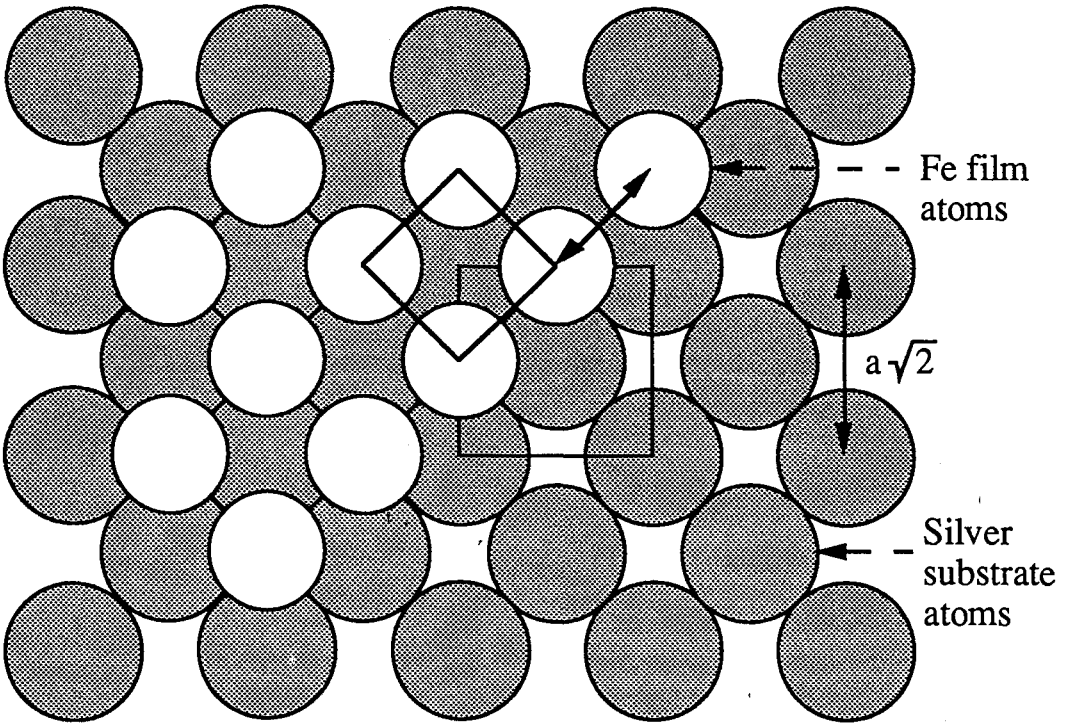

Fig. 3.5 Schematic diagram of the atomic layer of bcc Fe(001) deposited on the Ag(001) surface. After a 45° rotation the net of Fe atoms matches very well the 4-fold hollow sites of the Ag(001) surface.

the in-plane bcc Fe lattice spacing, a_{Fe} = 2.87Å. The lateral mismatch is very small, 0.6%. However there is a significant difference (17%) between the vertical spacing of bcc Fe(001) and fcc Ag(001). A high density of steps on the Ag(001) substrate affects the quality of the Fe(001) layers.

All layers were grown in a low-10^{-10} Torr range with the exception of Au which was growth in ~$4 \cdot 10^{-10}$ Torr. The substrate temperature was maintained at 300K. Deposition rates, approximately 1 to 2ML per minute, were monitored by means of the RHEED intensity oscillations of the specular spot and by a quartz crystal thickness monitor. All RHEED intensity measurements were recorded with the electron beam under the same angle of incidence, ~ 1°, close to the first anti-Bragg condition for a Fe(001) film. The only exception was the growth of Fe(001) on a Pd(001) template where a

smaller angle of incidence (~ 0.65°) was used. The film thickness determined from the period of RHEED intensity oscillations was in good agreement (within ±1/4 ML) with the thickness monitor reading.

The four studied systems would require characterization of 13 different growths. In order to keep the growth chapter within reasonable limits the following growths will be described in detail; Fe(001) on Ag(001), Cu(001) on Fe(001) and on Ag(001), and Pd(001) on Fe(001) and on Ag(001). These growths contain all the important features and therefore other growths are described by tables and short summaries in order to present all material with lucidity.

3.4.1 Fe(001) grown on Ag(001) single crystal substrates

Figure 3.6. shows the amplitude of RHEED intensity oscillations measured at the specular spot during the growth of a 12 ML film of bcc Fe(001) on a Ag(001) bulk single crystal substrate. The RHEED oscillations corresponding to the first 3ML are irregular despite the constant flux of Fe atoms from the furnace. Moreover, the oscillation period decreases (15%) during the first 5 - 6 oscillations of the iron growth. After that the period of oscillations remained constant. This result indicates that it takes at least 3ML of bcc Fe(001) to heal the vertical mismatch between the bcc Fe and fcc Ag lattices. After 3ML the iron film grows in a layer-by-layer mode. It is worth noting that for well prepared Ag(001) single crystals the RHEED oscillations were very reproducible. This is illustrated by a few RHEED oscillations patterns presented in this chapter and which were obtained on different Ag(001) substrates.

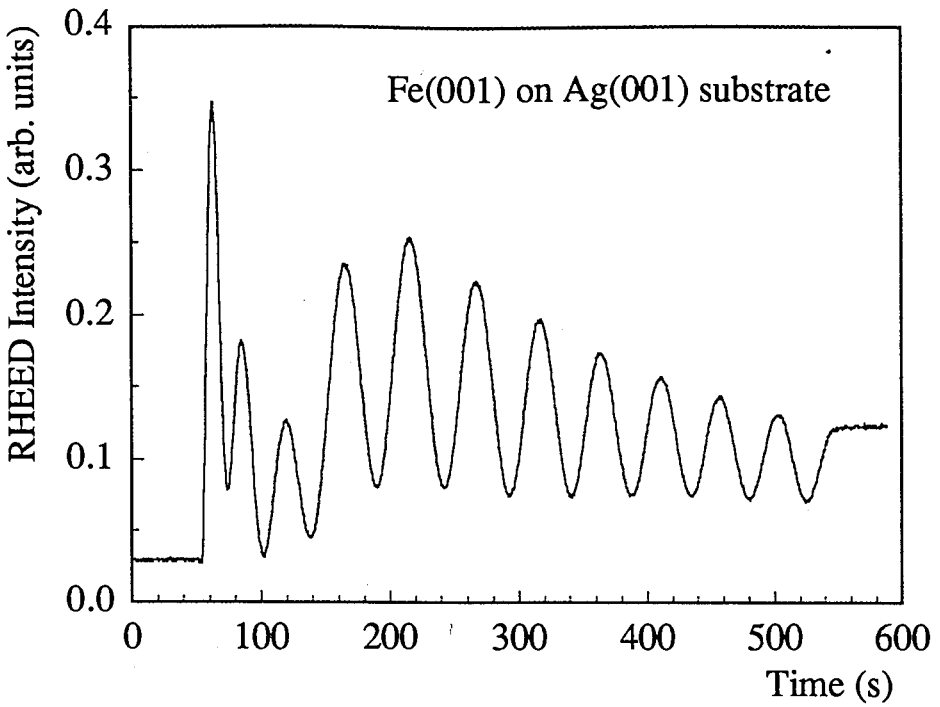

Fig.3.6 RHEED oscillations during the growth of Fe(001) on a singular Ag(001) single crystal substrate. Notice that the oscillations are present during the entire growth. The angle of incidence of the electron beam was 1^{o}, close to first anti-Bragg condition for Fe(001). The electron beam was directed ~5^{o} off the Fe{110} azimuth to avoid the Kikuchi line coming from inelastically scattered electrons [2.5].

The amplitude of RHEED intensity oscillations during the growth of Fe(001) on a Ag(001) substrate was very similar to that observed during the growth of Co(001) on Cu(001). Recently Dr. J. Kirschner's group [3.5] studied the growth of Co(001) on Cu(001) using Scanning Tunnelling Microscopy (STM). These studies clearly revealed a layer by layer growth. The STM results show directly that the presence of strong RHEED oscillations is a consequence of good layer by layer growth.

The RHEED intensity oscillations of Fe(001) on Ag(001) will be used as a "standard" to which all other growths will be compared. Three "categories" of RHEED oscillations were observed;

good - RHEED oscillations comparable to those observed during the growth of Fe(001) on Ag(001)

poor - the amplitude of RHEED oscillations was 3-4 times smaller than that observed during the growth of Fe(001) on Ag(001)

very poor - the strength of the RHEED oscillations was at least 10 times less than that observed during Fe(001) growth on Ag(001) substrate.

Figure 3.7 shows RHEED patterns along the {110} and {100} azimuths for a 5.7 ML thick Fe(001) layer grown on a Ag(001) substrate. After ~2ML the Fe(001) RHEED streaks develop a narrow split which is azimuthally symmetric. Once the split is created it remains throughout the whole growth. Such behavior was first observed by Henzler's group [3.6] for the growth of W on W(001) substrate using a high resolution LEED. They suggested that the nucleation proceeds by forming round atomic clusters one monolayer thick with nucleation centers randomly distributed but maintaining approximately an equidistant separation. The separation between nucleation centers is given by the reciprocal value of the vertical RHEED streak splitting [3.7]. For Fe on Ag(001) this distance was estimated to be 30 - 40 atomic distances. During growth the RHEED streak splitting is continuously present. This indicates that a new set of atomic islands is nucleated on top of already existing ones before the growing atomic islands coalesce into a complete atomic layer. Therefore one can argue that the Fe growth proceeds with at least two unfinished atomic layers. However the presence of strong RHEED oscillations indicates that only two partially covered atomic layers exist at any moment during the growth, see computer simulations by Arrott et at. [2.11]. The growth of Cu(001) on Fe(001) further supports this

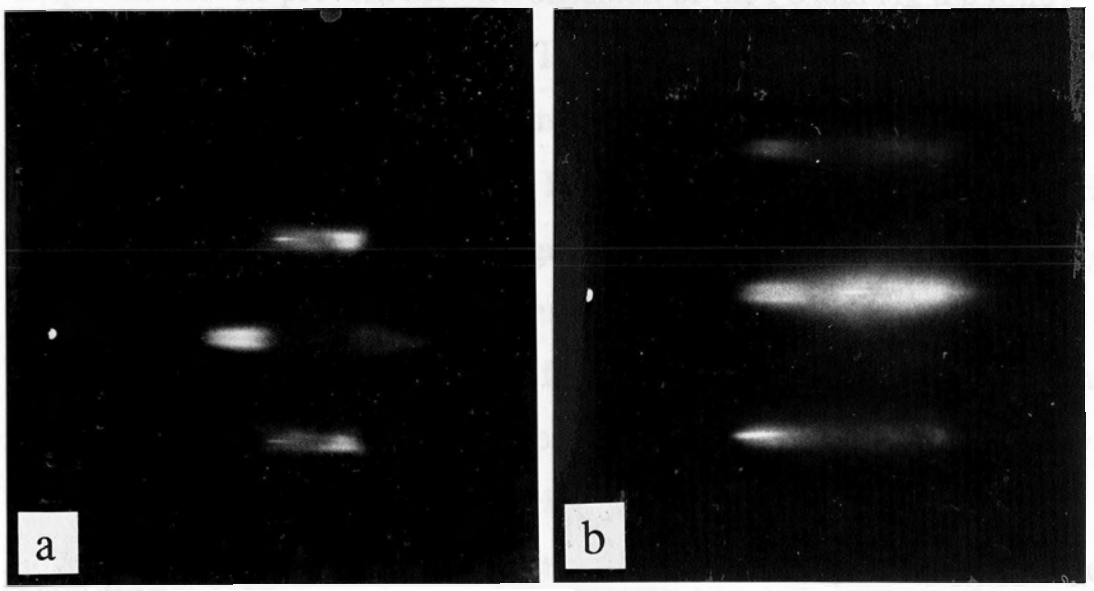

Fig. 3.7 RHEED patterns from a 5.7ML thick bcc Fe(001) layer grown on a Ag(001) single crystal substrate. (a) and (b) corresponds to the incident electron beam (10keV) directed along the Ag{100} and Ag{110} azimuths respectively. Note the streak splitting in the region of anti-Bragg scattering which indicates the presence of Henzler's structure.

conclusion. The bcc Cu(001) grows very well over an Fe(001) template which exhibits a well developed Henzler pattern. A single ML of Cu is sufficient to eradicate all traces of the Henzler pattern. This is strong evidence that the Henzler structure corresponds to a Fe(001) surface which is flat to within 1 ML. Fe growth terminated at a maximum of the RHEED intensity signal minimizes the roughness introduced by the Henzler mode of growth, see Figure 3.6 and was commonly used throughout the work presented in this thesis.

All studies presented in this thesis were carried out on structures which were grown at room temperature. The first Fe(001) layer in a trilayer structure always exhibited a Henzler structure on its top surface. The Henzler RHEED pattern can be avoided by growing Fe at elevated

temperatures. To prevent the interdiffusion of the Fe and Ag the following procedure has to be employed. An Fe(001) buffer layer was grown on the Ag(001) substrate at room temperature, usually 5.7ML thick, see Figure 3.8. Then the temperature was raised to 140 - 150°C for 10 minutes of annealing. AES measurements indicated no sign of intermixing between Fe(001) layers and the Ag(001) substrate. At elevated temperatures (140 - 150°C) the Henzler streak splitting diminished from the start of the Fe evaporation and disappeared before ~1ML was completed. The amplitude of the RHEED oscillations for Fe layers grown at elevated temperature was bigger than that observed in a Fe growth at room temperature indicating an excellent layer-by-layer growth - see Figure 3.8. RHEED patterns of Fe(001) films grown according to this procedure showed no signs of RHEED streak splitting indicating that the average terrace size was increased substantially and became comparable to that of the Ag(001) substrate.

The separation between the main Fe(001) RHEED streaks are indistinguishable from those of Ag(001). This indicates that within the limits of experimental resolution the in-plane Fe spacing corresponds to the lattice spacing of bulk Fe, a=2.87Å. Recent X-ray measurements by Dr. E. Fullerton [3.8] suggest that the interplanar separation of Fe layers is vertically expanded by 4%, $a_{\perp}$=3.0 Å.

In conclusion: Epitaxial Fe(001) layers were grown in a layer-by-layer mode on properly prepared Ag(001) single crystal substrates at room temperature. At least 3ML of bcc Fe(001) have to be grown to heal significantly the vertical mismatch between the bcc Fe and fcc Ag lattices. The Fe films terminated at maxima of RHEED oscillations have their surface roughness limited to 1ML.

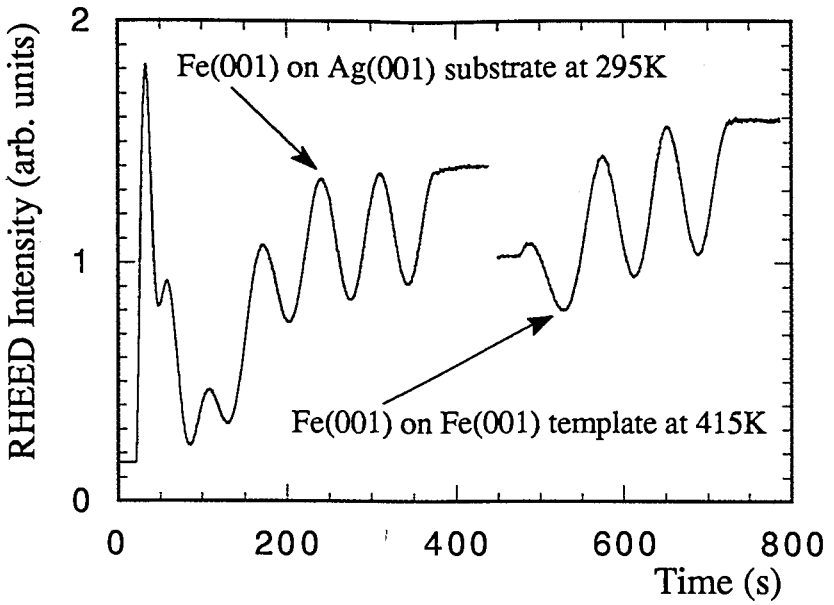

Fig. 3.8 RHEED intensity oscillations measured at the specular spot during the growth of Fe(001) on Ag(001) single crystal substrate at 295K and Fe(001) on Fe(001) template at 415K. Note the increase of the RHEED amplitude at elevated temperature. The angle of incidence of the electron beam was 1^{o}, close to the first anti-Bragg condition for iron. The primary electron beam was directed ~5^{o} off the Fe{110} azimuth.

3.4.2 The growth of Cu(001) on bcc Fe(001) film templates and on fcc Ag(001) single crystal substrates

Figure 3.9 shows RHEED intensity oscillations measured at the specular spot during the growth of 18 ML of Cu(001) on a 5.7ML thick bcc Fe(001) template. The presence of large RHEED intensity oscillations from the start of the deposition indicates that the Cu(001) films were formed in a good layer-by-layer growth mode. The period of the RHEED intensity oscillations corresponds to the completion of one monoatomic layer. This result was cross-correlated with the thickness monitor data. Only the first

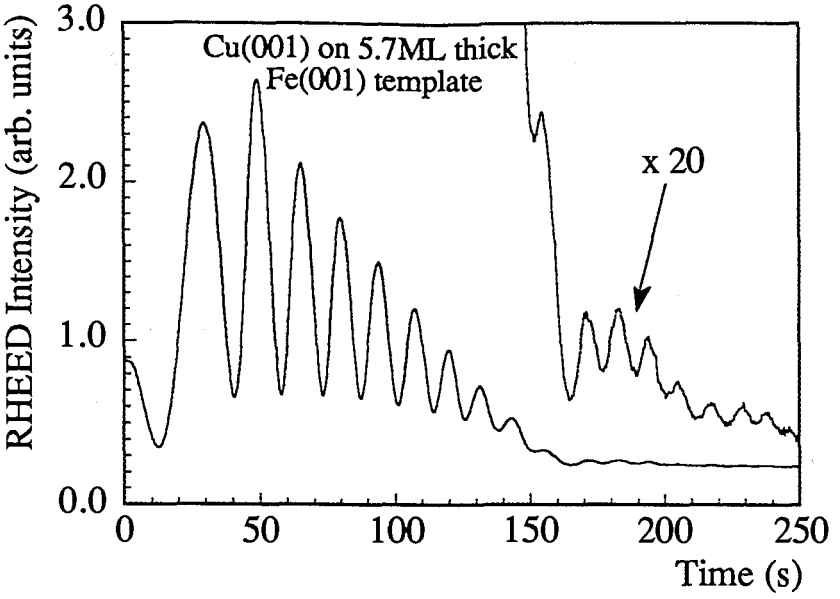

Fig. 3.9 RHEED oscillations during the growth of metastable bcc Cu(001) on bcc Fe(001). Notice that RHEED oscillations are present during the entire growth with the amplitude of oscillations decreasing rapidly at the onset of surface reconstruction. The angle of incidence of the electron beam was 1°. The electron beam was directed ~5° off the Fe{110} azimuth.

two periods, see Fig. 3.9, are irregular despite the constant flux of Cu atoms from the furnace. The amplitude of oscillations decays slowly with an increasing thickness. At a critical thickness of 10 - 11ML, the amplitude of RHEED oscillations decreases substantially. RHEED oscillations are diminished, but clearly visible even after the critical thicknesses was reached, see Figure 3.9. This behavior is related to the onset of a Cu(001) surface reconstruction which starts to develop after the Cu layer reaches a critical thickness.

Figure 3.10 shows the RHEED patterns of unreconstructed and reconstructed Cu films grown on Fe(001) templates. The unreconstructed layer (see Figure 3.10 a,b) maintains the in-plane symmetry of Fe(001). The

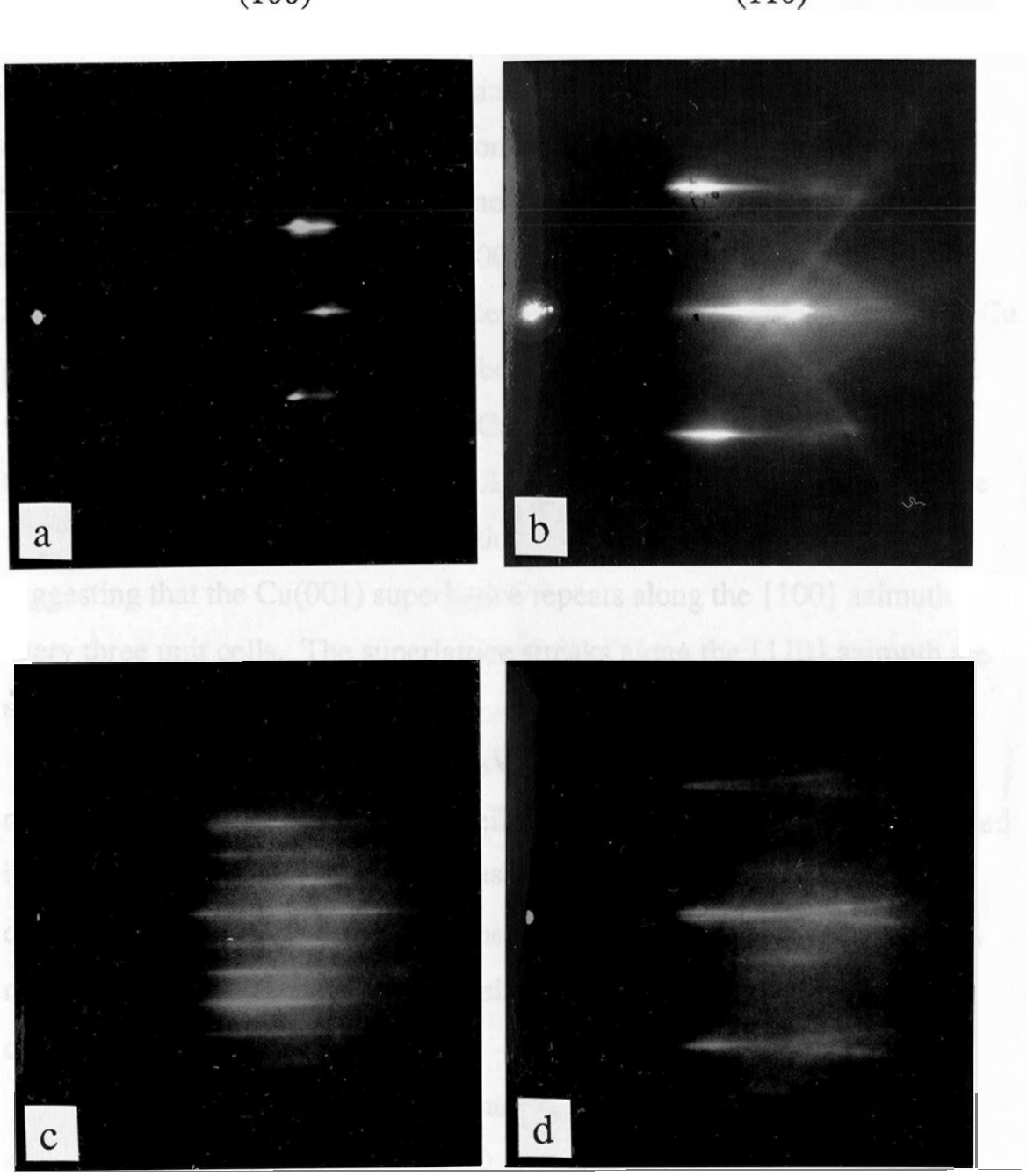

Fig.3.10 RHEED patterns from metastable bcc Cu(001) layers; (a) and (b) in 6ML Cu(001) grown on a 5.7ML thick Fe(001) template; (c) and (d) from 14ML Cu(001) grown on a 5.7ML thick Fe(001) template. The incident electron beam (10keV) is along the Cu{100} and Cu{110} azimuths in (a), (c) and (b), (d) respectively.

RHEED streak separations for the Cu(001) film grown on Fe(001) are approximately 1% smaller than those for the Fe(001) template. These measurements indicate that the in-plane copper lattice spacing was approximately 1% larger than the iron lattice spacing (2.87Å for bcc Fe). The RHEED technique is generally not sensitive to the vertical spacing. Recent LEED measurements of Cu(001) grown on an Fe(001) whisker by Dr. S.T. Purcell [3.9] from Philips Research Laboratories showed that the Cu growth proceeds in a nearly perfect bcc structure. The RHEED patterns were significantly altered when the Cu(001) overlayer reached the critical thickness of 10-11 ML; see Figure 3.10 c, d. The RHEED pattern along the {100} azimuths developed two additional symmetrically spaced streaks, suggesting that the Cu(001) superlattice repeats along the {100} azimuth every three unit cells. The superlattice streaks along the {110} azimuth are more complex, see Figure 3.10 d

AES measurements of the Fe L_3VV line as a function of the Cu overlayer thickness showed a well defined exponential decay. The calculated inelastic mean free path (IMFP) λ was in a good agreement with the calculated value (see eq. 2.1) using the Seah and Dench formula [2.4]. This result confirms that the Fe(001) template is well covered by the Cu(001) overlayer.

Figure 3.11 shows RHEED intensity oscillations measured at the specular spot during the growth of Cu(001) on an fcc Ag(001) substrate. This result indicates that bcc Cu(001) grows well on Ag(001) single crystal substrates. The angular resolved XPS measurements by W.F. Egelhoff, Jr. et al. [3.10] showed that the vertical distortion in bcc Cu(001) films is small, approximately 4% expanded. EXAFS investigations by D.T. Jiang et al.

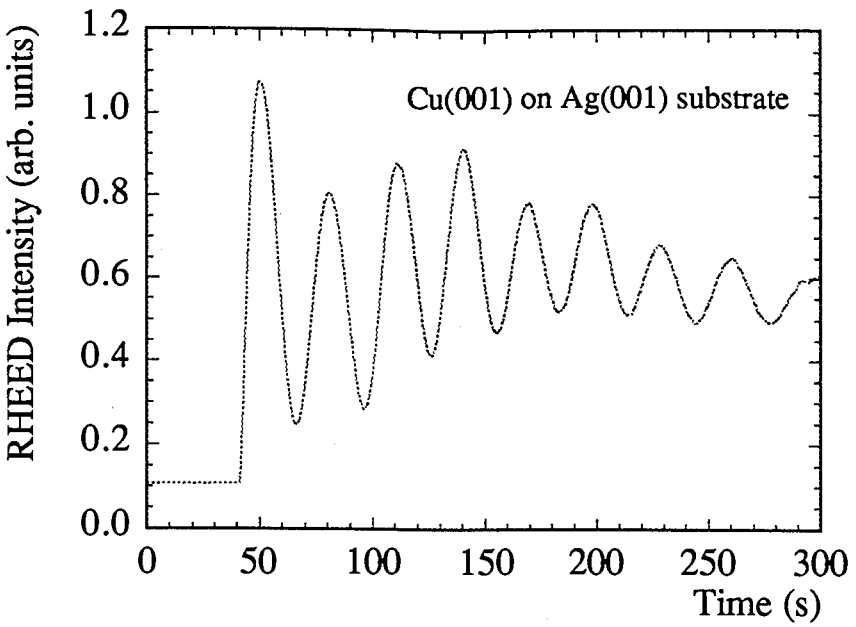

Fig. 3.11 RHEED oscillations during the growth of metastable bcc Cu(001) on a Ag(001) single crystal substrate. Notice that the oscillations are present during the entire growth. The electron beam angle of incidence was 1° and the electron beam were directed ~5° off the Cu{110} azimuth.

[3.11] concluded that the structure of epitaxial Cu(001) film grown on the Ag(001) substrate is bct (body centered tetragonal) with a vertical axis, c=3.10Å, which is 7.6% expanded relative to the in-plane spacing.

In conclusion: Metastable phases of epitaxial bcc Cu(001) were grown on bcc Fe(001) templates and fcc Ag(001) single crystal substrates. Cu(001) grows in a layer-by-layer growth mode up to a thickness of ~10-11ML. For Cu(001) layers thicker then 11ML there is a complicated surface reconstruction and a substantial decrease in RHEED intensity oscillations.

3.4.3 The growth of Pd(001) on bcc Fe(001) film templates and fcc Ag(001) single crystal substrates

Figure 3.12 shows RHEED intensity oscillations measured at the specular spot during the growth of Pd(001) on a 5.7ML thick bcc Fe(001) film template. The presence of large RHEED oscillations from the start of deposition indicates that the Pd(001) films were formed in a good layer by layer growth mode. The amplitude of oscillations decays very slowly until a critical thickness (12ML) is reached at which thickness the Pd(001) film undergoes a minor surface reconstruction. The RHEED intensity oscillations are clearly visible even after the reconstruction. Note that part of the data shown in Figure 3.12 was expanded 10 times in order to show the oscillations.

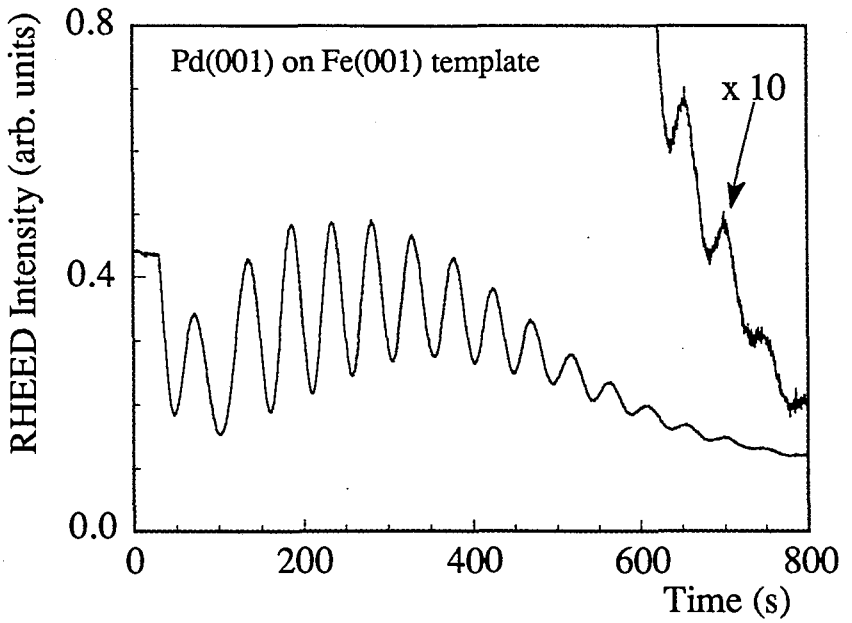

Fig. 3.12 RHEED oscillations during the growth of metastable fcc Pd(001) on bcc Fe(001). Notice that the oscillations are present during the entire growth with the amplitude of oscillations decreasing rapidly at the onset of the surface reconstruction. The angle of incidence of the electron beam was 1°. The electron beam was directed ~5° off the Fe{110} azimuth.

Figure 3.13 shows the RHEED patterns of a unreconstructed and a reconstructed Pd film grown on a Fe(001) template. The unreconstructed layer (see Figure 3.13 a, b) maintains the in-plane symmetry and spacing of the Fe(001) template indicating that the in-plane palladium lattice is latterly expanded 5% ($a_{\parallel Pd}$=4.06Å) compared to that of the bulk fcc palladium (3.89Å). Recent X-ray measurements by Dr. E. Fullerton [3.8] carried out on Pd(001) overlayers grown on Fe(001) film templates revealed that the Pd layer is vertically contracted (8%), with the vertical lattice spacing of $a_{\perp Pd}$=3.62Å. Therefore the volume per Pd atom in latterly expanded Pd(001) increases by 2% compared with that in bulk Pd.

The RHEED patterns were altered when the Pd(001) overlayer reached a critical thickness of 12 ML; see Figure 3.13 c, d. The RHEED patterns along {210} azimuth possess a well developed additional streak which is a half way between original the {210} streaks. Two symmetric superlattice streaks along the {100} azimuths were observed, see Figure 3.13 d. The blobiness of RHEED patterns indicates an increased surface roughness in reconstructed Pd(100) films.

AES measurements of the Fe L_3VV line as a function of the Pd overlayer thickness showed an exponential decay, see Figure 3.14. The calculated inelastic mean free path (IMFP) λ=5.6ML was 20% smaller that predicted by the Seah and Dench formula [2.4], $\lambda \approx$7ML. This result shows good coverage of the Fe(001) template by Pd and supports the conclusion, based on RHEED studies, that the growth of Pd(001) on a Fe(001) template proceeds in a good layer by layer manner.

Figure 3.15 shows RHEED intensity oscillations measured at the specular spot during the growth of Pd(001) on a fcc Ag(001) single crystal

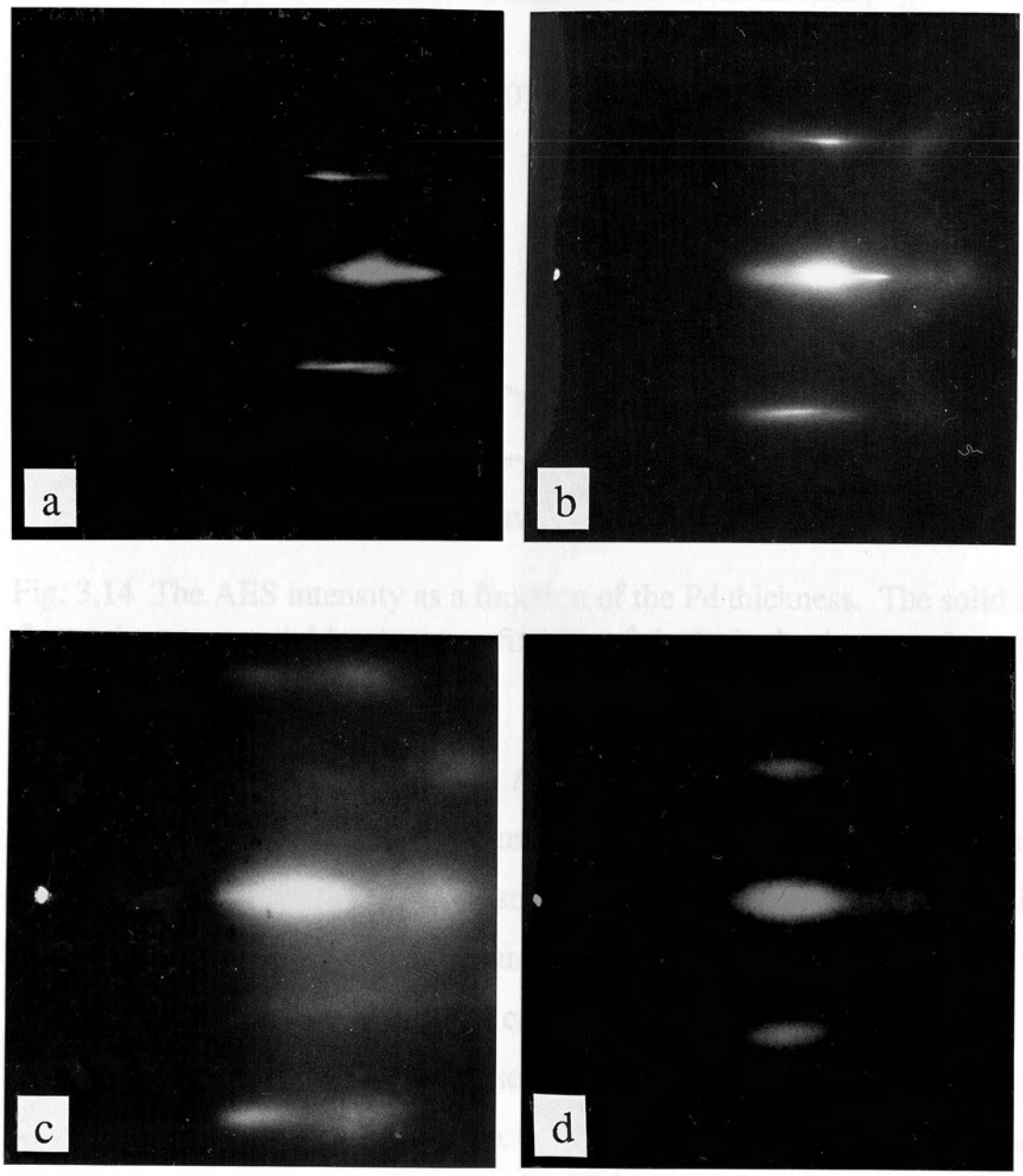

Fig. 3.13 The Pd(001) RHEED patterns; (a) and (b) in RHEED patterns of 8ML Pd(001) grown on a 5.7ML thick Fe(001) template along the {110} and {100} azimuths respectively; (c) and (d) in RHEED patterns of 16ML Pd(001) grown on a 5.7ML thick Fe(001) template along {210} and {100} azimuths respectively.

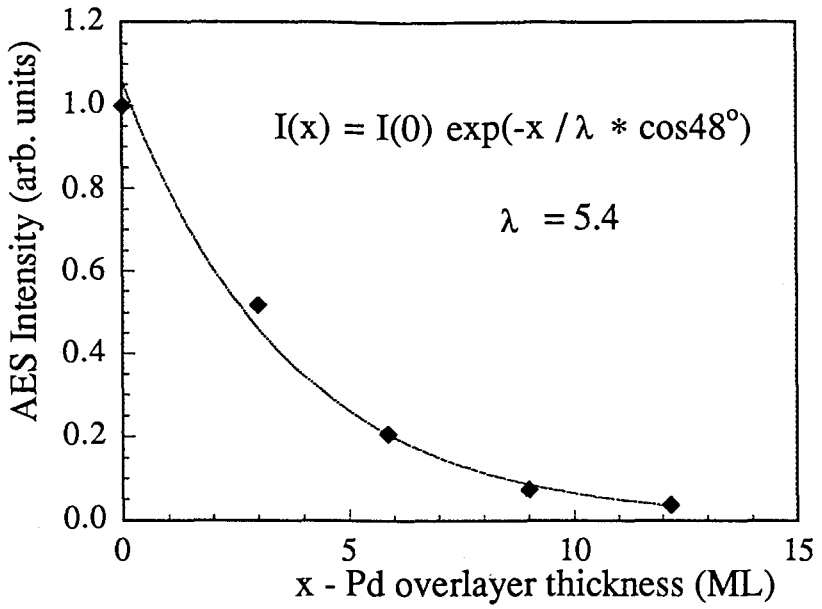

Fig. 3.14 The AES intensity as a function of the Pd thickness. The solid line shows the exponential least square fit where λ is the inelastic mean free path of an Auger electron.

substrate. Again Pd(001) grows on Ag(001) substrates in a good layer by layer growth mode. The unreconstructed Pd layer maintained the in-plane symmetry of the Ag(001) substrate. The RHEED streak separations for the Pd(001) overlayer are the same as for the Ag(001) substrate indicating the same in-plane lattice constant, a=4.089Å.

In conclusion: Metastable phases of epitaxial fcc Pd(001) films were grown on Fe(001) templates and on Ag(001) single crystal substrates. The growths of Pd(001) proceeds in a layer-by-layer mode up to a critical thickness of ~12ML. Minor surface reconstruction occurs in Pd(001) layers thicker then 12ML and results in an increased surface roughness.

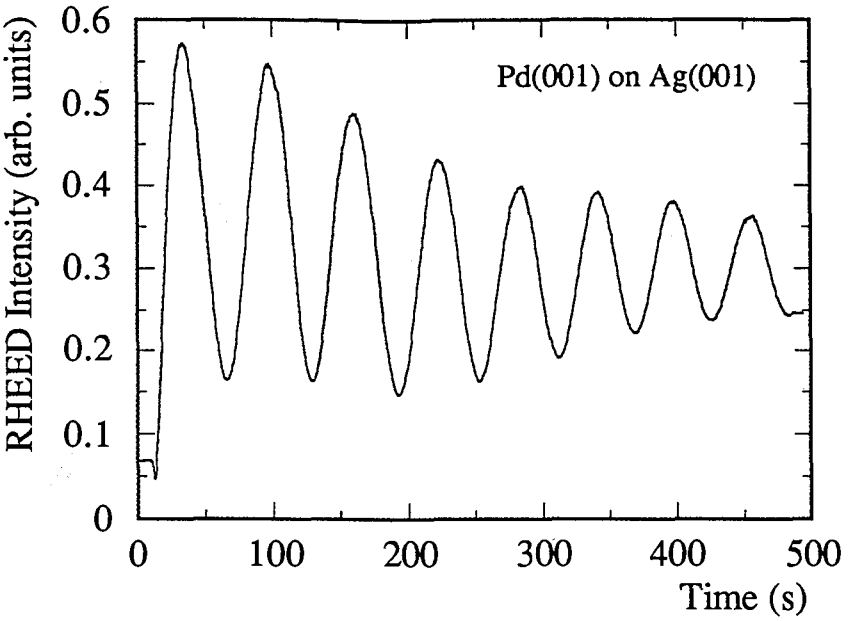

Fig. 3.15 RHEED oscillations during the growth of metastable fcc Pd(001) on a Ag(001) single crystal substrate. Notice that the oscillations are present during the entire growth. The angle of incidence of the electron beam was 1^{o}. The electron beam was directed ~5^{o} off the Pd{100} azimuth.

3.4.4 The growth of Ag(001) on Fe(001) film templates

Table 3.1 summarizes the RHEED studies of Ag(001) growth on Fe(001) templates. The presence of large RHEED intensity oscillation from the start of the deposition indicates that the Ag(001) films were formed in a good layer-by-layer growth mode, see Figure 3.16. The amplitude of RHEED oscillations decays very slowly with an increasing Ag thickness. Thick Ag(001) layers, up to 26ML, were grown with strong oscillations during the entire growth.

Table 3.1 The growth of Ag(001) on Fe(001) film templates - RHEED studies.

Growth	RHEED intensity oscillations	RHEED patterns
Ag(001) on Fe(001) film templates	good - large RHEED intensity oscillations are present from the start of the Ag deposition, see Figure 3.16. Their amplitude decays very slowly with increasing Ag thickness.	fair - the RHEED patterns indicate that the Ag(001) films are not as flat as the Ag(001) single crystal substrates.

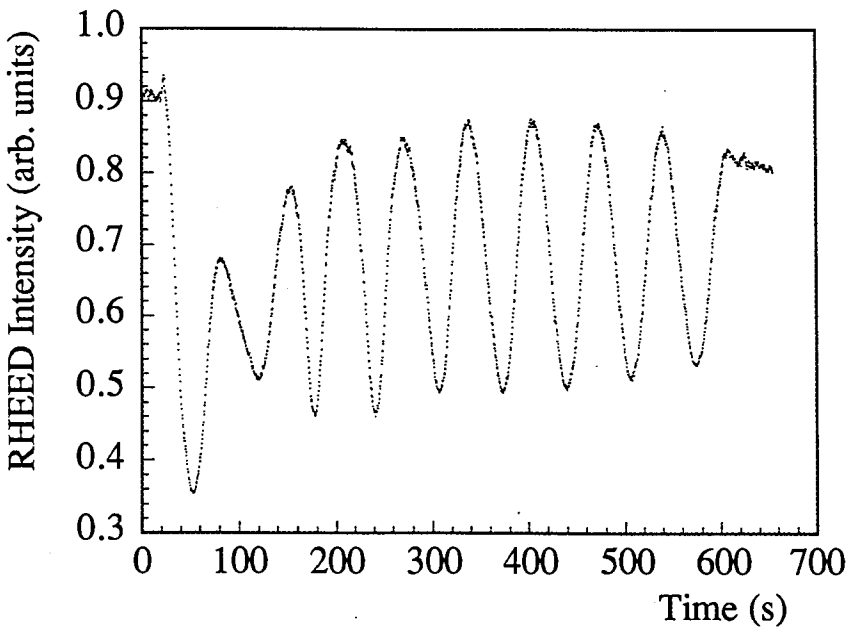

Fig. 3.16 RHEED oscillations during the growth of fcc Ag(001) on a bcc Fe(001) template. Notice that the oscillations are present during the entire growth. The angle of incidence of the electron beam was 1°. The electron beam was directed ~5° off the Fe{110} azimuth.

3.4.5 The growth of Au(001) on Fe(001) film templates

Table 3.2 summarizes the RHEED studies of Au(001) growth on Fe(001) templates. The Au(001) films exhibited a typical bulk Au(001) surface reconstruction [3.12], see Figure 3.17. Fe adatoms cover the corrugated Au(111) surface well. One additional atomic layer of Fe reestablishes a simple (001) RHEED pattern.

Table 3.2 The growth of Au(001) on Fe(001) film templates - RHEED studies.

Growth	RHEED intensity oscillations	RHEED patterns
Au (001) on Fe(001) film templates	good - after the first three oscillations which are irregular; a distinct second harmonic develops after depositions of 5ML of Au, see Figure 3.18	good - streaks are very narrow and exhibit no sign of the 3-D features; reconstructed surface of Au(001) develops four additional symmetrically spaced streaks along {100} azimuths; along {110} azimuths characteristic fans are visible, see Figure 3.17

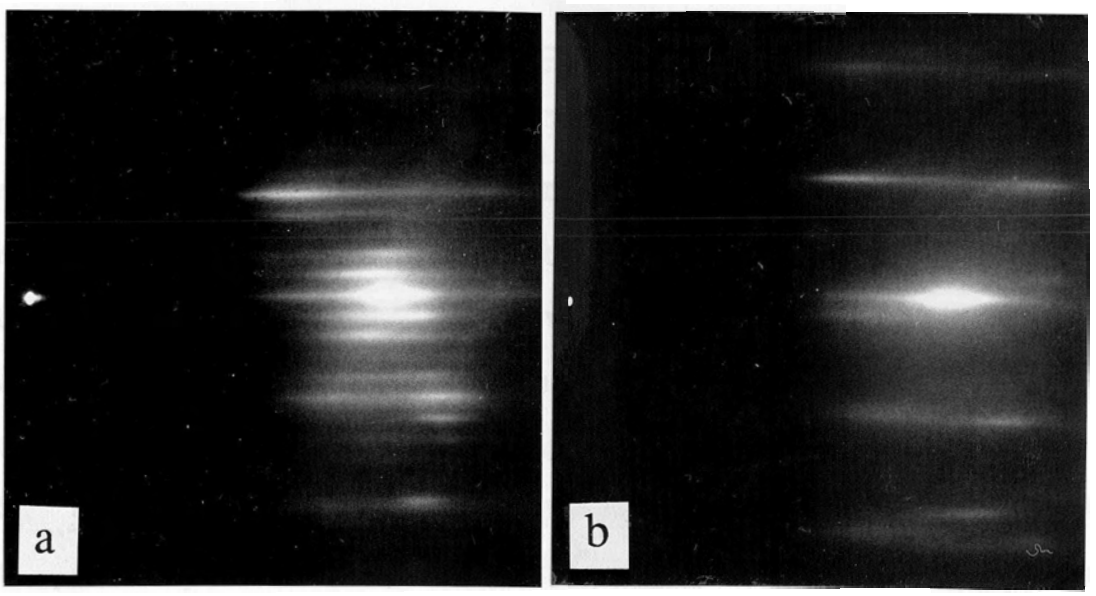

Fig. 3.17 RHEED patterns from a 10ML Au(001) grown on 5.7ML bcc Fe(001). (a) and (b) show {100} and {110} azimuths respectively.

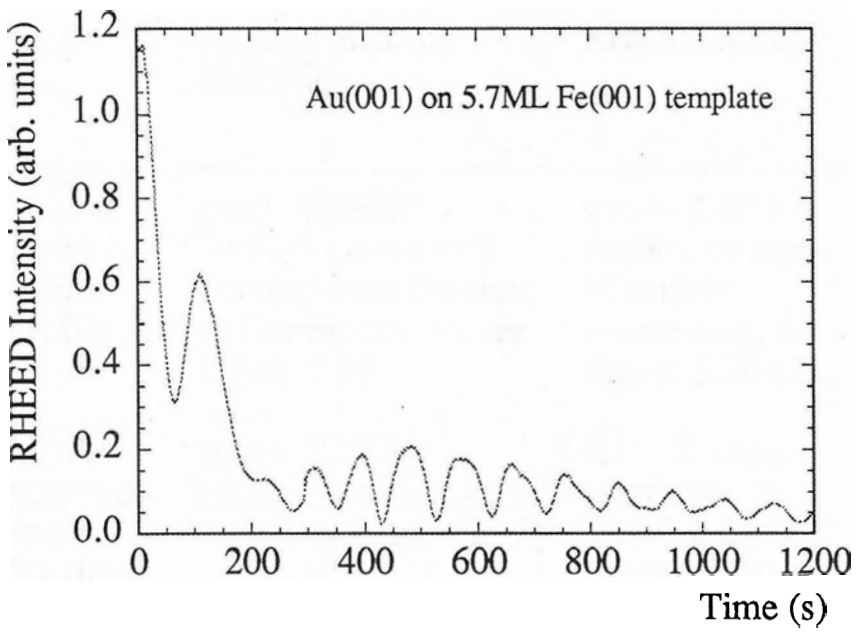

Fig. 3.18 RHEED oscillations during the growth of fcc Au(001) on a bcc Fe(001) template. The angle of incidence of the electron beam was 1°. The electron beam was directed ~5° off the Fe{110} azimuth.

3.4.6 The growth of Fe(001) on metastable bcc Cu(001) film templates

Table 3.3 summarizes the RHEED studies of Fe(001) growth on metastable bcc Cu(001) templates. These Cu(001) templates were grown on Ag(001) single crystal substrate or on Fe(001) films which were grown on Ag(001) single crystal substrates.. Fe(001) films grown on an unreconstructed Cu(001) surface showed well developed RHEED oscillations from the start of the iron evaporation. The amplitude of oscillation is comparable to that of Fe grown on Ag, see Figure 3.19a, clearly indicating a layer by layer growth. However the growth of Fe on reconstructed Cu(001) templates is poor with the RHEED pattern indicating 3-dimensional features, see Figures 3.19b and 3.20.

Table 3.3 The growth of Fe(001) on metastable bcc Cu(001) film templates - RHEED studies.

Growth	RHEED intensity oscillation	RHEED patterns	Henzler streak splitting
Fe on unreconstructed surface of Cu(001) film	good - RHEED oscillations are well develop from the start of Fe evaporation, see Figure 3.19	good - 2-D pattern, no sign of surface roughening, see Figure 3.20 a,b	present
Fe(001) on reconstructed surface of Cu(001) film	poor - RHEED oscillations were very weak, see Figure 3.19	fair - features presence associated with 3-D clearly indicating an increased surface roughness, see Figure 3. 20 c,d	-

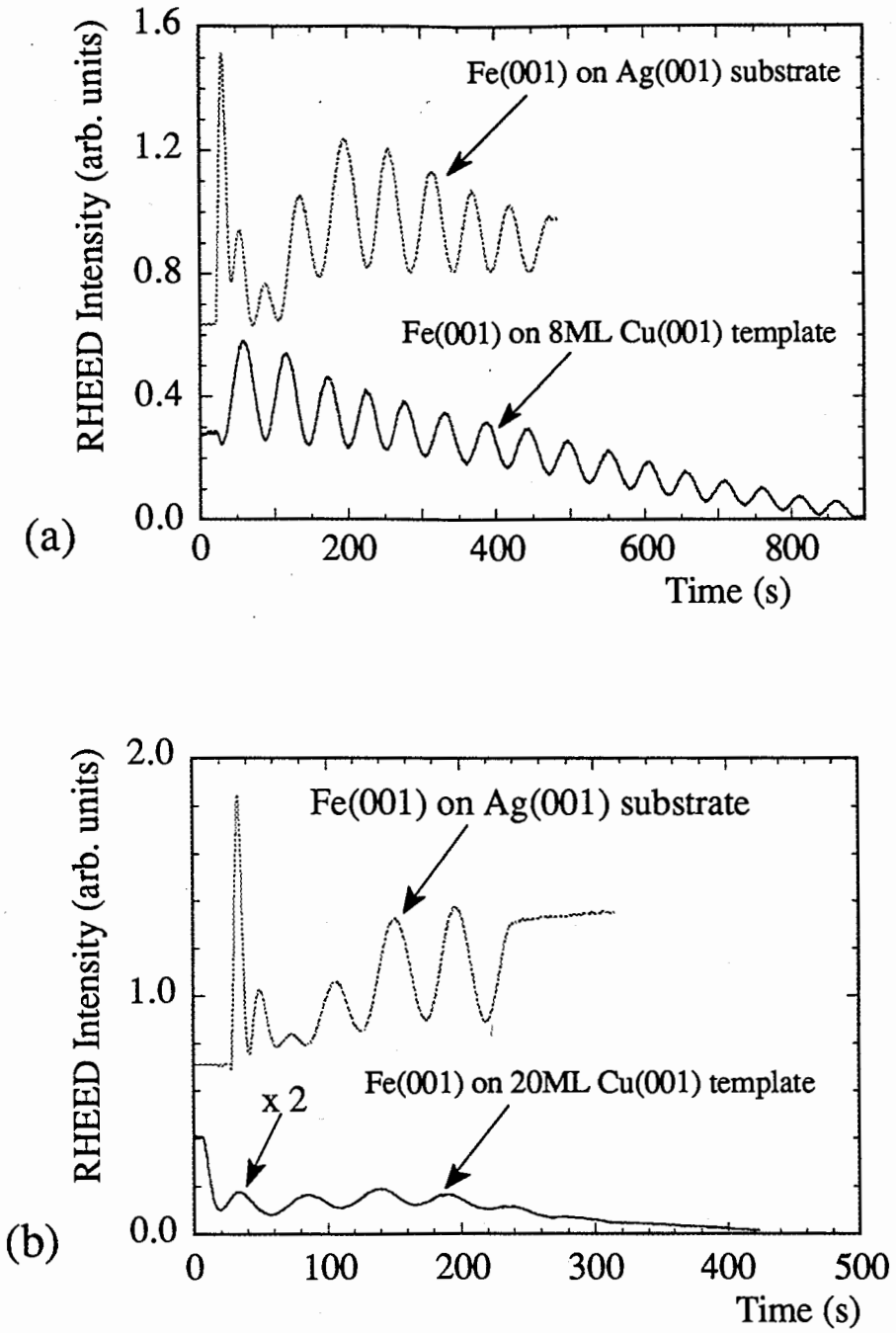

Fig. 3.19 RHEED intensity oscillations measured at the specular spot during the growth of Fe(001) on metastable bcc Cu(001) templates. (a) 16 ML Fe(001) grown on a 8 ML thick unreconstructed Cu(001) template. (b) 10 ML Fe(001)grown on a reconstructed 20ML thick Cu(001) template. For comparison, the growth of Fe(001) grown on Ag(001) single crystal substrate is shown also. The angle of incidence of the electron beam was 1^{o}, close to first anti-Bragg condition for iron. The electron beam was directed ~5^{o} off the Fe{110} azimuth.

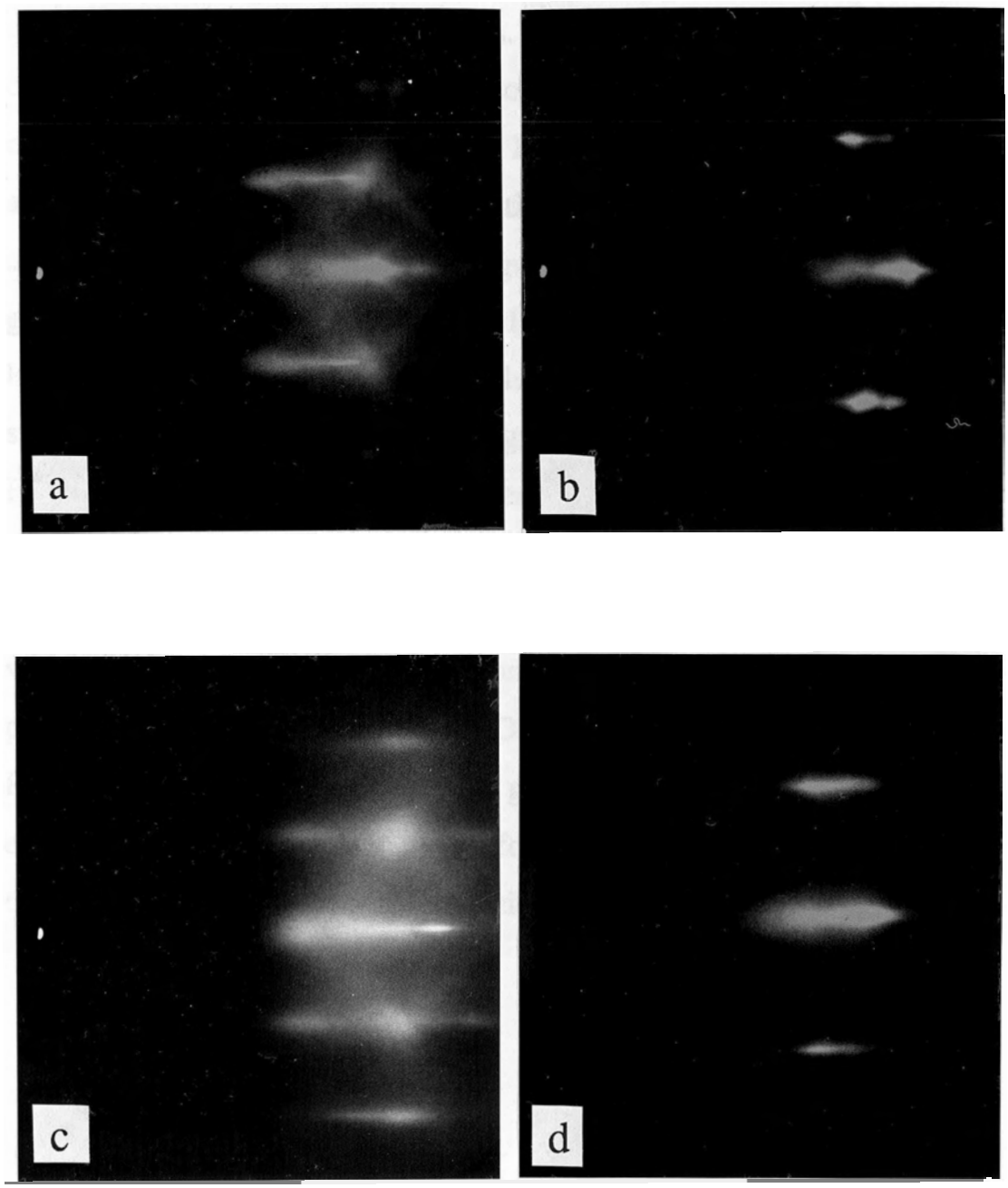

Fig. 3.20 RHEED patterns: (a),(b) from 11ML Fe(001) grown on 6ML unreconstructed bcc Cu(001); (c), (d) from 10ML Fe(001) grown on a 12.6ML reconstructed Cu(001) template. (a), (c) and (b), (d) show {100} and {110} azimuths respectively.

3.4.7 The growth of Fe(001) on metastable fcc Pd(001) film templates

Table 3.4 summarizes the RHEED studies of Fe(001) growth on latterly expanded fcc Pd(001) film templates. These Pd(001) templates were grown on Ag(001) single crystal substrates or on Fe(001) films which were grown on Ag(001) single crystal substrates. RHEED studies showed that the amplitude of the iron RHEED oscillations is very weak and depends on the thickness of the Pd(001) film, see Figure 3.21. These results indicate that the growth did not proceed in a layer by layer mode. RHEED patterns from Fe layers grown on unreconstructed and reconstructed surfaces of Pd(001) were similar and revealed clear signs of significant surface roughening, see Figure 3.22a and b. However the intensity measurements of the Pd MNN Auger line as a function of Fe overlayer thickness showed that Pd covered well the Fe substrate. The Pd MNN electron inelastic mean free path was within 5% of the calculated value from an empirical equation (see eq. 2.1) proposed by Seah and Dench [2.4]. Despite the 3-D features observed in RHEED patterns, the Fe(001) layers grown on Pd(001) film templates exhibit narrow FMR lines and therefore the Fe(001)/Pd(001)/Fe(001) trilayers were well suited for magnetic studies.

Table 3.4 The growth of Fe(001) on metastable fcc Pd(001) templates - RHEED studies.

Growth	RHEED intensity oscillation	RHEED patterns	Henzler streak splitting
Fe(001) on unreconstructed surface of Pd(001)	very poor - only first 3 RHEED oscillations were visible; the smaller angle of incident, ~0.65°, was used to follow the Fe RHEED oscillations throughout the whole ~10ML growth, see Figure 3.21 a	poor - 3-D pattern, signs of significant surface roughening, see Figure 3.22 a,b	-
Fe(001) on reconstructed surface of Pd(001)	very poor - the smaller angle of incidence, ~0.65°, was used to follow the Fe RHEED oscillations throughout the whole ~10ML growth, see Figure 3.21b	poor - 3-D pattern clearly indicating surface roughening	-

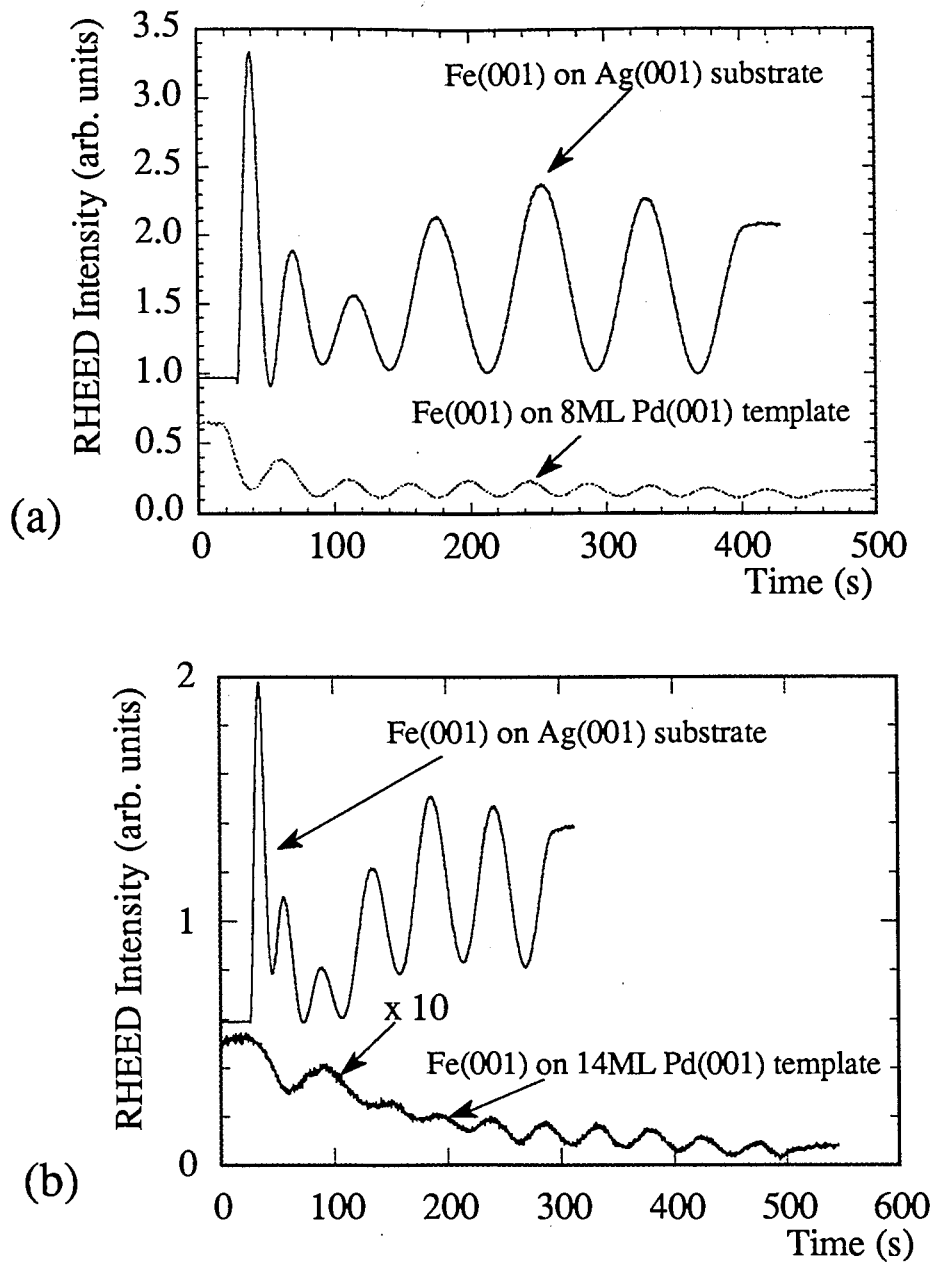

Fig. 3.21 RHEED intensity oscillations measured at the specular spot during the growth of an Fe(001) layer on a Pd(001) template. (a) for 10 ML Fe(001) film on 8 ML thick unreconstructed Pd(001) template. (b) for 10 ML thick Fe(001) film on 14ML thick Pd(001) with reconstructed surface. For comparison, the growth of Fe(001) on a Ag(001) single crystal substrate is shown.

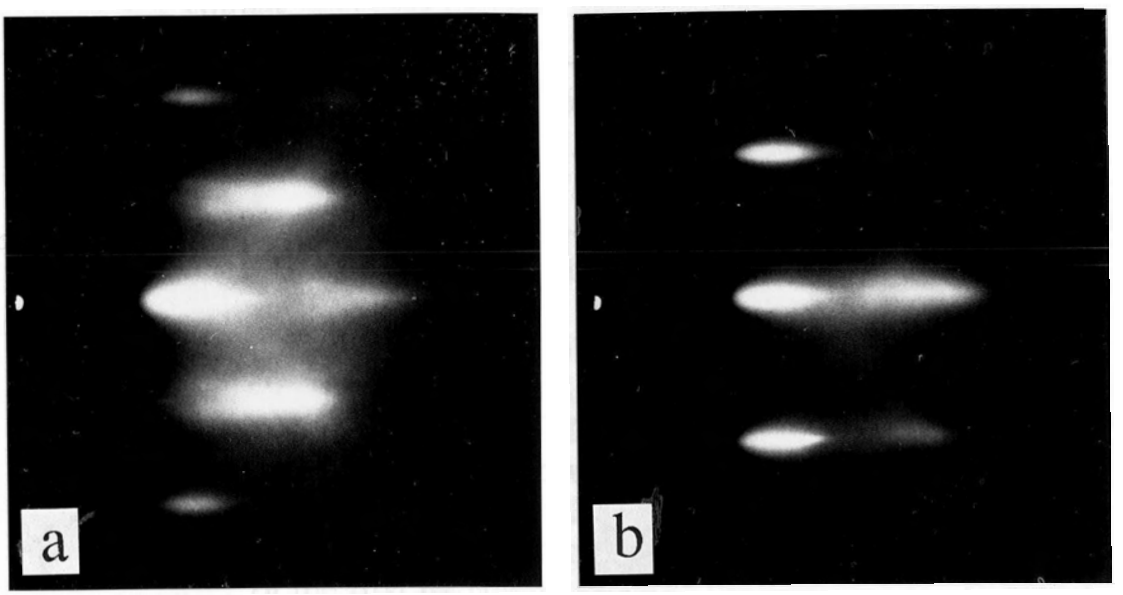

Fig. 3.22 RHEED patterns from 10ML Fe(001) grown on 8ML fcc Pd(001). (a) and (b) show {110} and {100} azimuths respectively.

3.4.8 The growth of Fe(001) on fcc Ag(001) film templates

Table 3.5 summarizes the RHEED studies of Fe(001) growth on fcc Ag(001) film templates. Fe(001) layers grew in a good layer-by-layer mode on Ag(001) film templates. However 4ML of Fe(001) are needed to heal the vertical mismatch between the bcc Fe and fcc Ag lattices. The Fe RHEED patterns indicate an increased surface roughness compared with that of Fe grown on single crystal Ag(001) substrates.

Table 3.5 The growth of Fe(001) on Ag(001) film templates - RHEED studies.

Growth	RHEED intensity oscillation	RHEED patterns	Henzler streak splitting
Fe(001) on fcc Ag(001) film templates	poor - it takes 4ML of Fe to establish regular oscillations on Ag(001) film templates, see Figure 3.23; The amplitude of RHEED oscillation in this growth is 5 times smaller than that observed during the growth of the first Fe layer, see Figure 3.23	fair - weak 3-D features clearly indicate an increased surface roughening	present

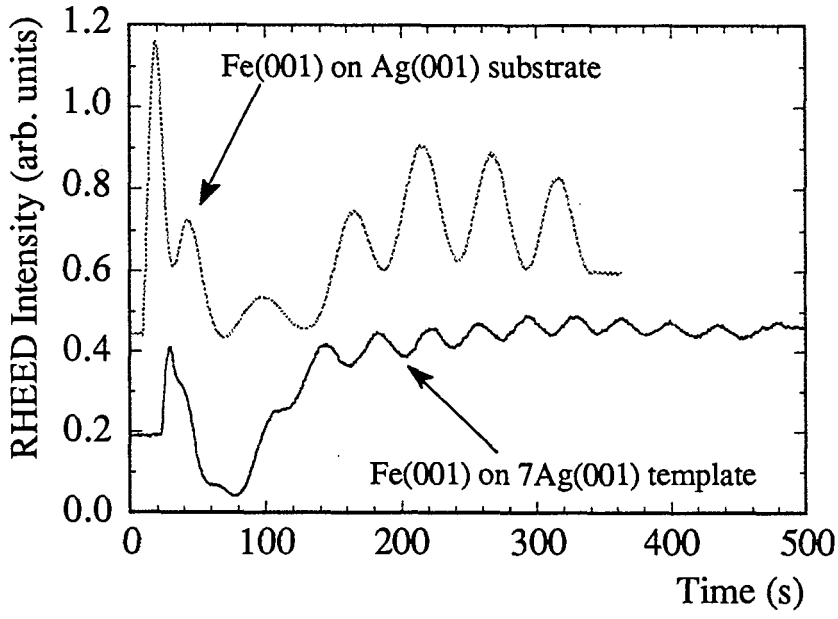

Fig. 3.23 RHEED intensity oscillations measured at the specular spot during the growth of a 12ML thick Fe(001) layer on a fcc Ag(001) template. For comparison, the growth of Fe(001) on a Ag(001) single crystal substrate is shown. The angle of incidence of the electron beam was 1°. The electron beam was directed ~5° off the Fe{110} azimuth.

3.4.9 The growth of Fe(001) on fcc Au(001) film templates

Table 3.6 summarizes the RHEED studies of Fe(001) growth on fcc Au(001) film templates. Epitaxial Fe(001) layers were grown in a good layer-by-layer growth mode on Au(001) film templates at room temperature despite the fact that Au(001) templates exhibits a strong surface reconstruction. The surface of the Fe(001) film is smooth. The Henzler structure was not present in the RHEED patterns during the growth of Fe on Au(001) templates.

Table 3.6 The growth of Fe(001) on Au(001) film templates - RHEED studies.

Growth	RHEED intensity oscillation	RHEED patterns	Henzler streak splitting
Fe(001) on fcc Au(001) film templates	good - large RHEED intensity oscillations are present from the start of Fe deposition, see Figure 3.24 Their amplitude is comparable to that observed during the growth of the first Fe layer.	good - sharp streaks with no features of 3-D blobiness	not present

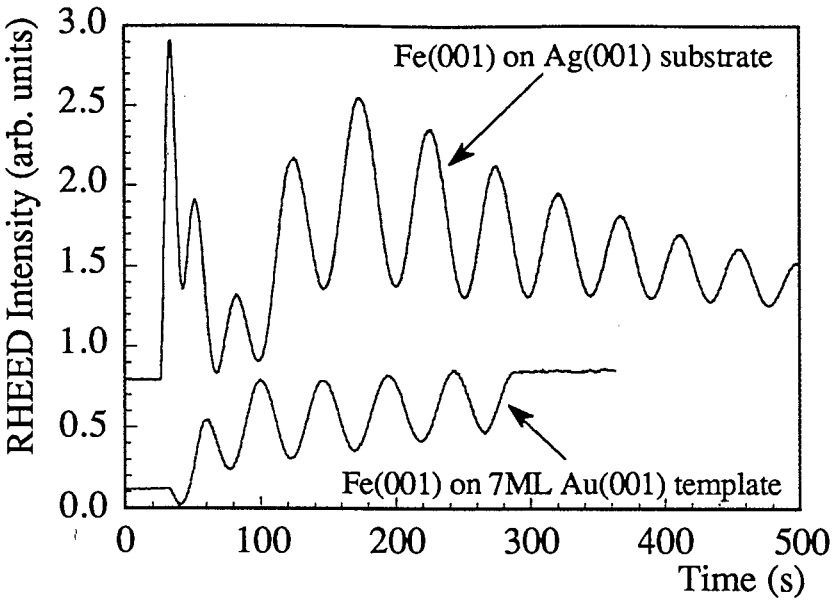

Fig. 3.24 RHEED intensity oscillations measured at the specular spot during the growth of a 5.5ML thick Fe(001) layer on a 7ML thick fcc Au(001) template. For comparison, the growth of Fe(001) on the Ag(001) single crystal substrate is shown. The angle of incidence of the electron beam was 1°. The electron beam was directed ~5° off the Fe{110} azimuth.

Chapter 4

The exchange magnetic coupling; phenomenology of FMR measurements

A phenomenological model of exchange coupled layers is described in this chapter. This model was used in FMR studies of Fe(001)/X(001)/Fe(001) trilayers, where X(001) denotes a non magnetic interlayer. The exchange coupling will be treated for both parallel and perpendicular configurations. In the perpendicular configuration the dc applied field and the saturation magnetization are perpendicular to the surface. In the parallel configuration the static magnetization lies in the plane of the surface. The rf magnetization in the perpendicular configuration can be expressed in the form of right and left handed polarized precessions. This results in a significant simplification of the algebraic solutions; this configuration will be used to explore the main features of exchange coupled trilayers. The FMR measurements were carried out using the parallel configuration. In this configuration the algebraic treatment of the exchange coupling becomes complex and only computer calculations will be shown.

Figure 4.1 shows the coordinate system appropriate for the perpendicular configuration. A and B denote two ferromagnetic layers. The static magnetizations $\mathbf{M}_S^A = M_S^A \hat{\mathbf{z}}$ and $\mathbf{M}_S^B = M_S^B \hat{\mathbf{z}}$ and the applied static magnetic field, $\mathbf{H}_O = H_O \hat{\mathbf{z}}$ are perpendicular to the surface. An incident microwave radiation, $\mathbf{h} = (h_x \hat{\mathbf{x}} + h_y \hat{\mathbf{y}})\exp(-i\omega t)$, stimulates the transverse rf magnetizations, $\mathbf{m}^A = (m_x^A \hat{\mathbf{x}} + m_y^A \hat{\mathbf{y}})\exp(-i\omega t)$ and $\mathbf{m}^B = (m_x^B \hat{\mathbf{x}} + m_y^B \hat{\mathbf{y}})\exp(-i\omega t)$,

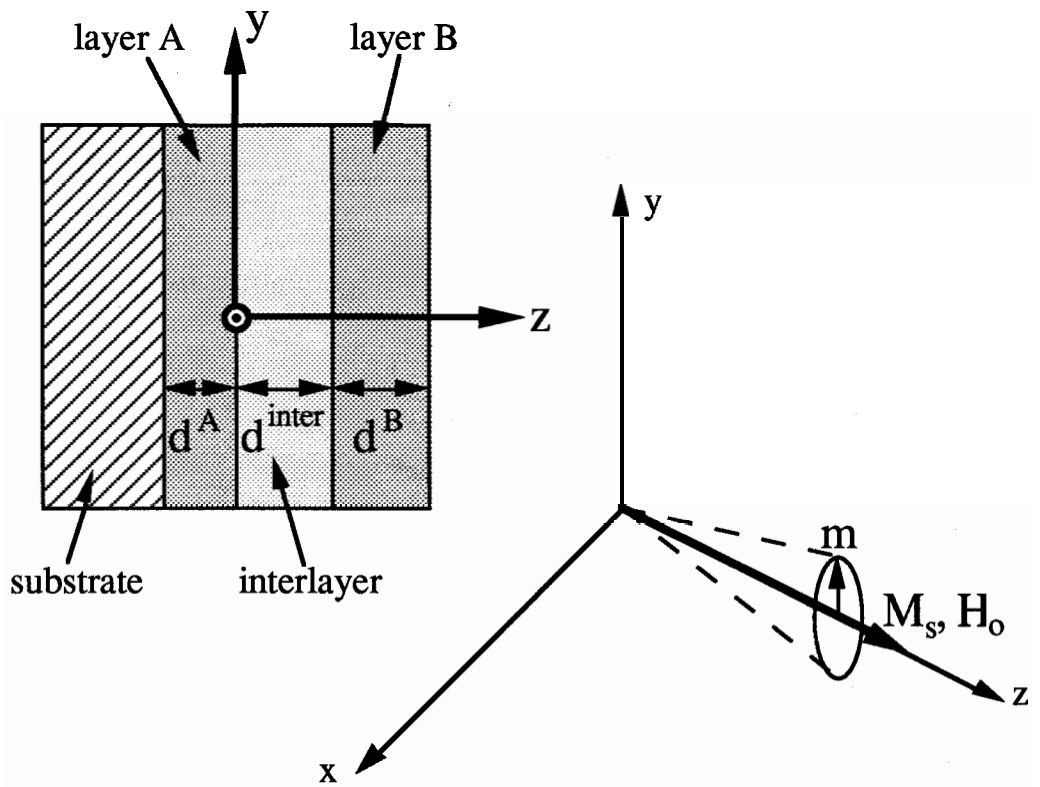

Fig. 4.1 The coordinate system used for the theory of eigenmodes of two ferromagnetic layers separated by a non magnetic interlayer.

where $\hat{x}$, $\hat{y}$, and $\hat{z}$ are the unit vectors. The h_x, h_y, m_x^A, m_y^A, m_x^B, and m_y^B are complex number which are function of z. The response of the magnetic system to applied rf fields can be found by analyzing the Landau-Lifshitz (L-L) equations of motion with appropriate boundary conditions. The discussion will be carried out for the layer A only, keeping in mind that the same equations are valid for the layer B unless clearly indicated otherwise. The Landau-Lifshitz equation of motion is given by

$$-\frac{1}{\gamma^A}\frac{\partial \mathbf{M}^A}{\partial t} = \tau = \mathbf{M}^A \times \mathbf{H}_{eff}^A \qquad 4.1$$

where $\gamma^A = g|e|/(2mc)$ is the gyromagnetic ratio and τ is the torque density. The magnetization, $\mathbf{M}^A$, and the effective field, $\mathbf{H}_{eff}^A$, have contributions from both static and rf components, that is [4.1]

$$\mathbf{M}^A = \mathbf{M}_S^A + \mathbf{m}^A \quad \text{and} \quad (\mathbf{H}_{eff}^A)_\alpha = - \frac{\partial F^A}{\partial M_\alpha^A} \qquad 4.2$$

where F^A is the magnetic free energy per unit volume of the layer A and α = x, y, and z.

For ultrathin films the demagnetizing energy density is given by

$$E_D^A = - \frac{4\pi D}{2} \left(M_\perp^A \right)^2, \qquad 4.3$$

where $4\pi D$ is the demagnetization factor and $\mathbf{M}_\perp^A$ is the component of magnetization $\mathbf{M}^A$ perpendicular to the film surface. The demagnetizing factor, $4\pi D$, in ultrathin films depends on the number of atomic planes and for bcc and fcc films was calculated by Heinrich et al. [1.2, 4.2].

Spin-orbit interactions generate magnetocrystalline anisotropies. Since the electron orbital motion is coupled to the crystal, the free energy of a ferromagnetic layer acquires terms which depend on the direction of magnetization $\mathbf{M}^A$ with respect to the crystal lattice axes. These satisfy the ultrathin film lattice symmetry requirements. For (001) films:

$$E_K^A = - \frac{1}{2} K_{1\parallel}^A \left[(\alpha_x^4 + \alpha_y^4) \right] - \frac{1}{2} K_{1\perp}^A \alpha_z^4 - K_u^A \alpha_z^2 \qquad 4.4$$

where α_x, α_y, α_z are the directional cosines with respect to the cubic axes, $K_{1\parallel}^A$ describes the strength of the in-plane four fold anisotropy, and K_u^A and $K_{1\perp}^A$ are the second order and fourth order terms for the perpendicular uniaxial anisotropies.

The spin orbit interaction contributes also to the damping of the precessional motion. The intrinsic damping which determines the FMR linewidth is described by the Gilbert effective damping field. For the time dependence exp(-iωt) the Gilbert field is given by

$$\mathbf{h}_G^A = i \left(\frac{\omega}{\gamma^A}\right) \left(\frac{G^A}{\gamma^A}\right) \left(\frac{\mathbf{m}^A}{(M_s^A)^2}\right) \qquad 4.5$$

where G^A is the Gilbert damping parameter (of order 10^8 Hz for Fe ultrathin films) and $\gamma^A = (g|e|/(2mc))$. For simplicity $\gamma^A = \gamma^B = \gamma$.

The exchange interaction energy, E_{ex}, is minimized when all spins are parallel. Any nonuniformity in spin direction results in an increase of E_{ex}. The exchange energy density with a spatial nonuniform $\mathbf{M}^A$ is described by

$$E_{ex}^A = \frac{A_{ex}}{(M_s^A)^2} \{ (\nabla M_x^A)^2 + (\nabla M_y^A)^2 + (\nabla M_z^A)^2 \} \qquad 4.6$$

where A_{ex} is the coefficient describing the stiffness of the exchange interaction (Brown [4.3]).

It is assumed that $M_s^A >> m^A$, and $M_s^B >> m^B$, and $H_o >> h$. Therefore only the linear response to an applied microwave driving field **h** is considered, neglecting all terms in the L-L equations that are of the second or higher order in m_x^A, m_y^A, m_x^B, m_y^B, h_x, and h_y. From now on the time dependent factor $\exp(-i\omega t)$ will be omitted.

The torque, τ_h, exerted on the magnetization $\mathbf{M}^A$ by applied dc and rf fields is given by

$$\tau_h = \mathbf{M}^A \times (\mathbf{H}_o + \mathbf{h}) = \begin{bmatrix} H_o m_y^A - M_s^A h_y \\ M_s^A h_x - H_o m_x^A \\ 0 \end{bmatrix} \qquad 4.7$$

The demagnetizing field $\mathbf{H}_D^A$ and the corresponding torque, τ_D, are given by

$$\mathbf{H}_D^A = \begin{bmatrix} 0 \\ 0 \\ -4\pi D M_s^A \end{bmatrix} \quad \text{and} \quad \tau_D = \mathbf{M}^A \times \mathbf{H}_D^A = \begin{bmatrix} -4\pi D M_s^A m_y^A \\ 4\pi D M_s^A m_x^A \\ 0 \end{bmatrix} \qquad 4.8$$

The effective fourth order uniaxial anisotropy field, $\mathbf{H}_K^A$, and the torque, τ_K, exerted on $\mathbf{M}^A$ are given by

$$\mathbf{H}_K^A = \frac{2K_{1\perp}^A}{M_s^A}\begin{bmatrix} 0 \\ 0 \\ 1 \end{bmatrix} \quad \text{and} \quad \tau_K = \mathbf{M}^A \times \mathbf{H}_K^A = \frac{2K_{1\perp}^A}{M_s^A}\begin{bmatrix} m_y^A \\ -m_x^A \\ 0 \end{bmatrix} \qquad 4.9$$

The contribution of the second order uniaxial anisotropy is given by

$$\mathbf{H}_u^A = \frac{2K_u^A}{M_s^A}\begin{bmatrix} 0 \\ 0 \\ 1 \end{bmatrix} \quad \text{and} \quad \tau_u = \mathbf{M}^A \times \mathbf{H}_u^A = \frac{2K_u^A}{M_s^A}\begin{bmatrix} m_y^A \\ -m_x^A \\ 0 \end{bmatrix} \qquad 4.10$$

The effective field, $\mathbf{h}_G^A$, and corresponding torques, τ_G, due to the Gilbert damping are given by

$$\mathbf{h}_G^A = \frac{i\omega}{\gamma}\frac{G^A}{\gamma(M_s^A)^2}\begin{bmatrix} m_x^A \\ m_y^A \\ 0 \end{bmatrix} \quad \text{and} \quad \tau_G = \mathbf{M}^A \times \mathbf{h}_G^A = i\Delta H^A \begin{bmatrix} -m_y^A \\ m_x^A \\ 0 \end{bmatrix} \qquad 4.11$$

where $\Delta H^A = \frac{\omega}{\gamma}\frac{G^A}{\gamma M_s^A}$.

The exchange field, $\mathbf{h}_{ex}^A$, and the torque, τ_{ex}, exerted on $\mathbf{M}^A$ are given by

$$\mathbf{h}_{ex}^{A} = \frac{2A_{ex}}{(M_S^A)^2}\begin{bmatrix} \dfrac{\partial^2 m_x^A}{\partial z^2} \\ \dfrac{\partial^2 m_y^A}{\partial z^2} \\ 0 \end{bmatrix} \quad \text{and} \quad \tau_{ex} = \mathbf{M}^A \times \mathbf{h}_{ex}^A = \frac{2A_{ex}}{M_S^A}\begin{bmatrix} -\dfrac{\partial^2 m_y^A}{\partial z^2} \\ \dfrac{\partial^2 m_x^A}{\partial z^2} \\ 0 \end{bmatrix} \qquad 4.12$$

The left side of the L-L equation is equal to:

$$-\frac{1}{\gamma}\frac{\partial \mathbf{M}^A}{\partial t} = \frac{i\omega}{\gamma}\begin{bmatrix} m_x^A \\ m_y^A \\ 0 \end{bmatrix} \qquad 4.13$$

The L-L equations of motion for layer A are given by the sum of the above torques:

$$\begin{aligned} -i\frac{\omega}{\gamma} m_x^A - (b^A - i\Delta H^A) m_y^A &= h_y M_S^A + \frac{2A_{ex}}{M_S^A}\frac{\partial^2 m_y^A}{\partial z^2} \\ (b^A - i\Delta H^A) m_x^A + i\frac{\omega}{\gamma} m_x^A &= h_x M_S^A + \frac{2A_{ex}}{M_S^A}\frac{\partial^2 m_x^A}{\partial z^2} \end{aligned} \qquad 4.14$$

where $b^A = H_o - 4\pi D M_S^A + \dfrac{2K_u^A}{M_S^A} + \dfrac{2K_{1\perp}^A}{M_S^A}$

A similar pair of equations can be written for layer B.

It is useful to take explicitly into account that FMR is sensitive to the magnetic moments per unit area, $\boldsymbol{M}^A$ and $\boldsymbol{M}^B$, for which the components are:

$$M_\alpha^A \equiv \int_{-d^A}^{0} m_\alpha^A \, dz \quad \text{and} \quad M_\alpha^B \equiv \int_{d^{inter}}^{d^{inter}+d^B} m_\alpha^B \, dz \qquad 4.15$$

where α=x or y, and d^{inter} is the thicknesses of a non magnetic interlayer, see Fig. 4.1. For ultrathin films:

$$m_x^A(0) \approx m_x^A(-d^A) \approx \frac{M_x^A}{d^A} \quad \text{and} \quad m_y^A(0) \approx m_y^A(-d^A) \approx \frac{M_y^A}{d^A} \tag{4.16}$$

$$m_x^B(d^{inter}) \approx m_x^B(d^{inter} + d^B) \approx \frac{M_y^B}{d^B} \quad \text{and} \quad m_y^B(d^{inter}) \approx m_y^B(d^{inter} + d^B) \approx \frac{M_y^B}{d^B}$$

The integration results in following equations of motion

$$-i\frac{\omega}{\gamma} M_x^A + (b^A - i\Delta H^A) M_y^A = h_y M_s^A d^A + \frac{2A_{ex}}{M_s^A} \left\{ \left(\frac{\partial m_y^A}{\partial z}\right) \Big|_{z=0} - \left(\frac{\partial m_y^A}{\partial z}\right) \Big|_{z=-d^A} \right\}$$

$$(b^A - i\Delta H^A) M_x^A + i\frac{\omega}{\gamma} M_y^A = h_x M_s^A d^A + \frac{2A_{ex}}{M_s^A} \left\{ \left(\frac{\partial m_x^A}{\partial z}\right) \Big|_{z=0} - \left(\frac{\partial m_x^A}{\partial z}\right) \Big|_{z=-d^A} \right\} \tag{4.17}$$

$$-i\frac{\omega}{\gamma} M_x^B + (b^B - i\Delta H^B) M_y^B = h_y M_s^B d^B + \frac{2A_{ex}}{M_s^B} \left\{ \left(\frac{\partial m_y^B}{\partial z}\right) \Big|_{z=d^{inter}+d^B} - \left(\frac{\partial m_y^B}{\partial z}\right) \Big|_{z=d^{inter}} \right\}$$

$$(b^B - i\Delta H^B) M_x^B + i\frac{\omega}{\gamma} M_y^B = h_x M_s^B d^B + \frac{2A_{ex}}{M_s^B} \left\{ \left(\frac{\partial m_x^B}{\partial z}\right) \Big|_{z=d^{inter}+d^B} - \left(\frac{\partial m_x^B}{\partial z}\right) \Big|_{z=d^{inter}} \right\}$$

where h_x and h_y are the averaged rf fields. The second term on the right containing derivatives in eqs. 4.17 represents the surface exchange torques per unit area which are the consequence of the discontinuities at the surfaces.

These exchange torques at the surfaces are balanced by the surface anisotropies and the interlayer exchange torques, that is

$$\begin{aligned} &\mathbf{M}^A \times \mathbf{H}_S \Big|_{z=-d^A} = 0 \quad \text{and} \quad \mathbf{M}^A \times \mathbf{H}_S \Big|_{z=0} = 0 , \\ &\mathbf{M}^B \times \mathbf{H}_S \Big|_{z=d^{inter}} = 0 \quad \text{and} \quad \mathbf{M}^B \times \mathbf{H}_S \Big|_{z=d^{inter}+d^B} = 0 , \end{aligned} \tag{4.18}$$

where $\mathbf{H}_S$ represents all surface effective fields evaluated at $z=-d^A$ and 0 for layer A and at $z=d^{inter}$, $d^{inter}+ d^B$ for layer B. To solve the equations of motion (eqs. 4.17) the derivative terms in these equations are expressed in terms of the surface anisotropy fields and the interlayer exchange fields.

In order to see clearly each of the contributors to H_S (see eqs. 4.18) the atomistic Heisenberg - like model will be used. The return to continuum treatment will be carried out by replacing the magnetic moments per atom by

$$\mu = M_S \cdot \frac{a^3}{2} \tag{4.19}$$

where $a^3/2$ represent the volume per atom for a bcc lattice.

To evaluate the exchange coupling torques a pair interaction energy will be used in the Heisenberg form,

$$E_{ij} = -2J\, \mathbf{S}_i \cdot \mathbf{S}_j , \tag{4.20}$$

where $\mathbf{S}_i$ and $\mathbf{S}_j$ are the nearest neighbor spins and J is the exchange integral. Figure 4.2 shows the spin configuration used in calculations evaluating the exchange torque. For the surface spin $\mathbf{S}_0^A$ the exchange energy is $-8J\mathbf{S}_0^A\mathbf{S}_{-1}^A$. In the bcc lattice $\mathbf{S}_{-1}^A$ represents the nearest 4 neighbor spins. For a continuum the Taylor expansion can be used to evaluate the exchange energy

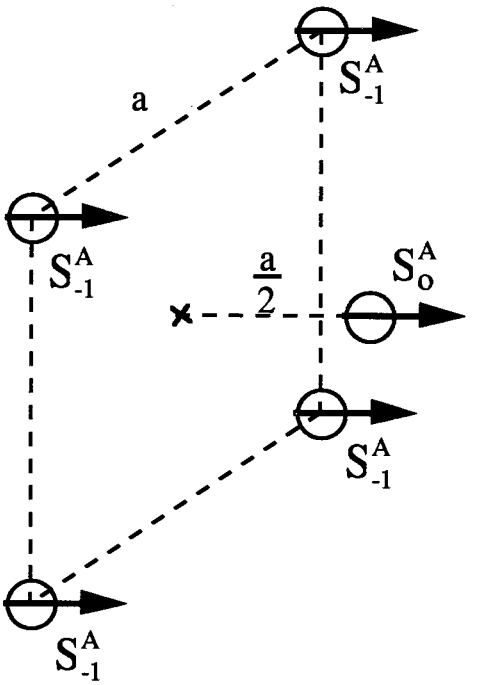

Fig. 4.2 The spin configuration used in evaluation of the exchange torques.

$$E_0^A = -\,8J\,\mathbf{S}_0^A \cdot \left(\mathbf{S}_0^A + \frac{-a}{2}\frac{\partial \mathbf{S}_0^A}{\partial z} + \ldots\right) \qquad 4.21$$

On the other hand the energy of a magnetic moment μ can be expressed by the relation

$$E_0^A = -\,\mu \cdot \mathbf{H}_0^A \qquad 4.22$$

where $\mu = g\mu_B\,\mathbf{S}_0^A$ and $\mathbf{H}_0^A$ the exchange effective field acting on spin $\mathbf{S}_0^A$. Therefore the $\mathbf{H}_0^A$ can be written as

$$\mathbf{H}_0^A = \frac{8J}{g\mu_B}\left(\mathbf{S}_0^A + \frac{-a}{2}\frac{\partial \mathbf{S}_0^A}{\partial z} + \ldots\right) \qquad 4.23$$

The above expansion can be rewritten by using the relationship between the saturation magnetization and the spin per atom in a bcc lattice,

$$M_S = \frac{2g\mu_B S}{a^3} \qquad 4.24$$

This leads to expression for the surface exchange field

$$\mathbf{H}_0^A = \frac{8A_{ex}}{a^2 M_s^2}\mathbf{M} - \frac{4A_{ex}}{aM_s^2}\frac{\partial \mathbf{M}}{\partial z} - .. \qquad 4.25$$

where the exchange stiffness coefficient A_{ex} is defined as

$$A_{ex} = \frac{2JS^2}{a} \qquad 4.26$$

The first term produces no torque as it acts along **M**. For spins at the surface the second term is dominant. Therefore the surface exchange fields for layer A and B are given by

$$\mathbf{H}_o^A\Big|_{z=-d^A} = \frac{2}{a}\frac{2A_{ex}}{(M_s^A)^2}\left(\frac{\partial \mathbf{m}^A}{\partial z}\right)\Big|_{z=-d^A}$$

$$\mathbf{H}_o^A\Big|_{z=0} = -\frac{2}{a}\frac{2A_{ex}}{(M_s^A)^2}\left(\frac{\partial \mathbf{m}^A}{\partial z}\right)\Big|_{z=0} \qquad 4.27$$

$$\mathbf{H}_o^B\Big|_{z=d^{inter}} = \frac{2}{a}\frac{2A_{ex}}{(M_s^B)^2}\left(\frac{\partial \mathbf{m}^B}{\partial z}\right)\Big|_{z=d^{inter}}$$

$$\mathbf{H}_o^B\Big|_{z=d^{inter}+d^B} = -\frac{2}{a}\frac{2A_{ex}}{(M_s^B)^2}\left(\frac{\partial \mathbf{m}^B}{\partial z}\right)\Big|_{z=d^{inter}+d^B}$$

The interface exchange energy per unit area is given by

$$E_{ex}^{AB} = -\frac{J^{AB}}{M_s^A M_s^B}\mathbf{M}^A\cdot\mathbf{M}^B \qquad 4.28$$

where J^{AB} is the interfacial exchange coefficient. Therefore the energy per interface atom is

$$E_{ex}^{AB}\, a^2 = -\, J^{AB}\, a^2 \frac{\mathbf{M}^A \cdot \mathbf{M}^B}{M_s^A M_s^B} = -\frac{a^3\, \mathbf{M}^A}{2} \cdot \frac{2\, J^{AB}}{a\, M_s^A M_s^B}\, \mathbf{M}^B \qquad 4.29$$

where a^2 is the area per atom. Comparing eqs. 4.22 and 4.29 one can evaluate the interlayer exchange fields:

$$\mathbf{H}^{AB}\Big|_{z=0} = \frac{2}{a}\frac{J^{AB}}{M_s^A M_s^B}\mathbf{M}^B$$

$$\mathbf{H}^{AB}\Big|_{z=d^{inter}} = \frac{2}{a}\frac{J^{AB}}{M_s^A M_s^B}\mathbf{M}^A \qquad 4.30$$

The surface anisotropy energy per unit area can be written as:

$$\left(E_K^S(\beta)\right)^{A,B} = -\frac{1}{2}\left(K_{1\|}^S(\beta)\right)^{A,B}\left[(\alpha_x^4 + \alpha_y^4)\right] - \left(K_u^S(\beta)\right)^{A,B}\alpha_z^2 \qquad 4.31$$

where $\left(K_{1\|}^S(\beta)\right)^{A,B}$ describes the strength of the surface four fold in-plane anisotropy, $\left(K_u^S(\beta)\right)^{A,B}$ is the surface second order term for the perpendicular uniaxial anisotropy, and $\beta = -d^A$, 0, and d^{inter}, $d^{inter}+d^B$ for the layer A and B respectively. The energy per surface atom is then given by $\left(E_K^S(\beta)\right)^{A,B} \cdot a^2$. For brevity the surface uniaxial anisotropy field will be evaluated only. Therefore the uniaxial energy at the surface per unit volume is given by

$$\frac{\left(E_K^S(\beta)\right)^A \cdot a^2}{\frac{a^3}{2}} = \frac{2}{a}\left(E_K^S(\beta)\right)^A \quad \text{and} \quad \frac{\left(E_K^S(\beta)\right)^B \cdot a^2}{\frac{a^3}{2}} = \frac{2}{a}\left(E_K^S(\beta)\right)^B \qquad 4.32$$

Applying the relation 4.2 results in the surface uniaxial anisotropy fields which are given by

$$\left(\mathbf{H}_u^S(\beta)\right)^A = \frac{2}{a}\frac{2\left(K_u^S(\beta)\right)^A}{M_s^A}\begin{bmatrix}0\\0\\1\end{bmatrix} \qquad 4.33$$

$$\left(\mathbf{H}_u^S(\beta)\right)^B = \frac{2}{a}\frac{2\left(K_u^S(\beta)\right)^B}{M_s^B}\begin{bmatrix}0\\0\\1\end{bmatrix}$$

The effective fields, H_S, at the appropriate interfaces are given by

$$\begin{aligned}
\mathbf{H}_S\Big|_{z=-d^A} &= \mathbf{H}_o^A\Big|_{z=-d^A} + \left(\mathbf{H}_u^S(-d^A)\right)^A \\
\mathbf{H}_S\Big|_{z=0} &= \mathbf{H}_o^A\Big|_{z=0} + \mathbf{H}^{AB}\Big|_{z=0} + \left(\mathbf{H}_u^S(0)\right)^A \\
\mathbf{H}_S\Big|_{z=d^{inter}} &= \mathbf{H}_o^B\Big|_{z=d^{inter}} + \mathbf{H}^{AB}\Big|_{z=d^{inter}} + \left(\mathbf{H}_u^S(d^{inter})\right)^B \\
\mathbf{H}_S\Big|_{z=d^{inter}+d^B} &= \mathbf{H}_o^B\Big|_{z=d^{inter}+d^B} + \left(\mathbf{H}_u^S(d^{inter}+d^B)\right)^B
\end{aligned} \qquad 4.34$$

The requirement that the sum of the surface torques must be equal zero (eqs. 4.18) results in the Hoffman boundary conditions:

$$\frac{2A_{ex}}{M_s^A}\left\{\left(\frac{\partial m_y^A}{\partial z}\right)\Big|_{z=0} - \left(\frac{\partial m_y^A}{\partial z}\right)\Big|_{z=-d^A}\right\} = -\frac{2}{d^A M_S^A}\left(K_u^S(0) + K_u^S(-d^A)\right)^A M_y^A$$

$$+ J^{AB}\left[\frac{M_y^B}{d^B M_S^B} - \frac{M_y^A}{d^A M_S^A}\right]$$

$$\frac{2A_{ex}}{M_s^A}\left\{\left(\frac{\partial m_x^A}{\partial z}\right)\Big|_{z=0} - \left(\frac{\partial m_x^A}{\partial z}\right)\Big|_{z=-d^A}\right\} = -\frac{2}{d^A M_s^A}\left(K_u^S(0) + K_u^S(-d^A)\right)^A M_x^A$$

$$+ J^{AB}\left[\frac{M_x^B}{d^B M_s^B} - \frac{M_x^A}{d^A M_s^A}\right] \qquad 4.35$$

$$\frac{2A_{ex}}{M_s^B}\left\{\left(\frac{\partial m_y^B}{\partial z}\right)\Big|_{z=d^{inter}+d^B} - \left(\frac{\partial m_y^B}{\partial z}\right)\Big|_{z=d^{inter}}\right\} =$$

$$-\frac{2}{d^B M_s^B}\left(K_u^S(d^{inter}) + K_u^S(d^{inter}+d^B)\right)^B M_y^B + J^{AB}\left[\frac{M_y^A}{d^A M_s^A} - \frac{M_y^B}{d^B M_s^B}\right]$$

$$\frac{2A_{ex}}{M_s^B}\left\{\left(\frac{\partial m_x^B}{\partial z}\right)\Big|_{z=d^{inter}+d^B} - \left(\frac{\partial m_x^B}{\partial z}\right)\Big|_{z=d^{inter}}\right\} =$$

$$-\frac{2}{d^B M_s^B}\left(K_u^S(d^{inter}) + K_u^S(d^{inter}+d^B)\right)^B M_x^B + J^{AB}\left[\frac{M_x^A}{d^A M_s^A} - \frac{M_x^B}{d^B M_s^B}\right]$$

In the above equation the magnetizations at the surface have been expressed in term of the total magnetic moment per unit area using eq.4.16.
The substitution of the derivative terms in the equations of motion (eqs. 4.17) by the right hand side of Hoffman boundary conditions (eqs 4.35) will result in a system of 4×4 algebraic equations.

Note that in ultrathin structures the surface anisotropies behave like uniaxial anisotropies which are inversely proportional to the layer thickness,

see eq. 4.35. Therefore the effective uniaxial anisotropies combine the bulk and surface contributions:

$$\left(K_u^{eff}\right)^A = K_u^A + \frac{\left(K_u^S(0)\right)^A + \left(K_u^S(-d^A)\right)^A}{d^A}$$

$$\left(K_u^{eff}\right)^B = K_u^B + \frac{\left(K_u^S(d^{inter})\right)^B + \left(K_u^S(d^{inter}+d^B)\right)^B}{d^B} \qquad 4.36$$

The effective uniaxial anisotropies enter the equations of motion like effective demagnetization fields. The effective magnetizations are given by

$$\left(4\pi M_{eff}\right)^A = 4\pi D M_s^A - \frac{2\left(K_u^{eff}\right)^A}{M_s^A}$$

$$\left(4\pi M_{eff}\right)^B = 4\pi D M_s^B - \frac{2\left(K_u^{eff}\right)^B}{M_s^B} \qquad 4.37$$

The solution of the equations of motion can be obtained somewhat more simply by the introduction of right and left hand polarized rf fields and rf magnetizations:

$$h_\pm = h_x \pm i\, h_y, \quad M_\pm^A = M_x^A \pm i\, M_y^A \quad \text{and} \quad M_\pm^B = M_x^B \pm i\, M_y^B \qquad 4.38$$

The equations of motion in terms of these variables are easily deduced from eqs. 4.17 and 4.35 and have the following form:

$$\left[\left(B_{eff}^A + \frac{J^{AB}}{d^A M_s^A} - i\Delta H^A\right) \pm \frac{\omega}{\gamma}\right] M_\pm^A + \frac{-J^{AB}}{d^B M_s^B} M_\pm^B = d^A M_s^A h_\pm$$

$$\frac{-J^{AB}}{d^A M_s^A} M_\pm^A + \left[\left(B_{eff}^B + \frac{J^{AB}}{d^B M_s^B} - i\Delta H^B\right) \pm \frac{\omega}{\gamma}\right] M_\pm^B = d^B M_s^B h_\pm \ , \qquad 4.39$$

where $B_{eff}^{A} = H_o - (4\pi M_{eff})^{A} + \frac{2K_{1\perp}^{A}}{M_S^{A}}$ and $B_{eff}^{B} = H_o - (4\pi M_{eff})^{B} + \frac{2K_{1\perp}^{B}}{M_S^{B}}$.

The general expression for susceptibility $\chi_{\pm}$ is given by

$$\chi_{\pm} = \frac{(M_{\pm}^{A} + M_{\pm}^{B})}{h_{\pm}} \qquad 4.40$$

where $M_{\pm}^{A}$ and $M_{\pm}^{B}$ were determined from the equations of motion (eq. 4.39). Only the susceptibility χ_- for the right hand polarization is considered because it exhibits a resonant behavior. In order to simplify the expression for χ_- the following notation is introduced:

$$H = H_o - \frac{\omega}{\gamma}, \quad K^{A} = (4\pi M_{eff})^{A} - \frac{2K_{1\perp}^{A}}{M_S^{A}} \quad \text{and} \quad K^{B} = (4\pi M_{eff})^{B} - \frac{2K_{1\perp}^{B}}{M_S^{B}} \qquad 4.41$$

The denominator which determines the resonant fields is given by

$$D_- = H^2 - H\left[K^{A} + K^{B} - J^{AB}\left(\frac{1}{d^{A}M_S^{A}} + \frac{1}{d^{B}M_S^{B}}\right)\right] + K^{A}K^{B} - J^{AB}\left(\frac{K^{B}}{d^{A}M_S^{A}} + \frac{K^{A}}{d^{B}M_S^{B}}\right)$$

$$- i\left[\Delta H^{A}\left(H - K^{B} + \frac{J^{AB}}{d^{B}M_S^{B}}\right) + \Delta H^{B}\left(H - K^{A} + \frac{J^{AB}}{d^{A}M_S^{A}}\right)\right] \qquad 4.42$$

The terms related to Gilbert damping parameters, ΔH^{A} and ΔH^{B}, are 100 times smaller than other effective fields. Therefore the imaginary part of the denominator can be neglected in the calculation of the resonant fields. The imaginary part contributes only to the FMR linewidth. The general expression for susceptibility has the following form:

$$\chi_- = \frac{d^{A}M_S^{A}\left(H - K^{B} + \frac{J^{AB}}{d^{B}M_S^{B}} - i\Delta H^{B}\right) + d^{B}M_S^{B}\left(H - K^{A} + \frac{J^{AB}}{d^{A}M_S^{A}} - i\Delta H^{A}\right) + 2J^{AB}}{D_-} \qquad 4.43$$

Two limits are considered here before a general solution will be given. For $J^{AB}=0$ the expression for χ_- reduces to

$$\chi_- = \frac{d^A M_s^A}{\left(H - K^A + i\Delta H^A\right)} + \frac{d^B M_s^B}{\left(H - K^B + i\Delta H^B\right)} \qquad 4.44$$

Two resonances are observed. The well known resonance condition for each of the individual layers in the perpendicular configuration is

$$H_o - \frac{\omega}{\gamma} - \left(4\pi M_{eff}\right)^A + \frac{2K_{1\perp}^A}{M_s^A} = 0$$

and $\qquad 4.45$

$$H_o - \frac{\omega}{\gamma} - \left(4\pi M_{eff}\right)^B + \frac{2K_{1\perp}^B}{M_s^B} = 0$$

Note that the amplitude in eq. 4.44 of the two decoupled modes are proportional to the $d^A M_S^A$ or $d^B M_S^B$ which represents the total magnetic moment in each individual layer. The total magnetic moment can be measured by monitoring the intensity of the FMR signal.

For very strong interlayer exchange coupling, $J^{AB} \approx \pm \infty$, only the terms in J^{AB} survive (see eq.4.43). Therefore the expression for χ_- reduces to

$$\chi_- = \frac{d^A M_s^A + d^B M_s^B}{H - \alpha K^A - (1 - \alpha) K^B} \qquad 4.46$$

where $\alpha = \dfrac{d^A M_s^A}{d^A M_s^A + d^B M_s^B}$

In this case there is a single resonance at

$$H_o - \frac{\omega}{\gamma} - \alpha\left[\left(4\pi M_{eff}\right)^A - \frac{2K_{1\perp}^A}{M_s^A}\right] - (1-\alpha)\left[\left(4\pi M_{eff}\right)^B - \frac{2K_{1\perp}^B}{M_s^B}\right] = 0 \qquad 4.47$$

Note that for strong coupling the overall effective demagnetizing field is a

sum of the demagnetizing fields of the individual layers, A and B, scaled by factors α and $(1-\alpha)$ respectively. This resonant field lies between the resonant fields of the individual layers. The amplitude in eq. 4.46 for this acoustic mode is proportional to $d^A M_S^A + d^B M_S^B$ which represents the total moment of two layers.

A general solution for resonant fields is rather long but it is worth while to examine it. The denominator D_- has always two roots for arbitrary J^{AB}, which are given below

$$2\left(H_o - \frac{\omega}{\gamma}\right) = K^A + K^B - J^{AB}\left(\frac{1}{d^A M_S^A} + \frac{1}{d^B M_S^B}\right)$$

$$\pm\left\{(K^B - K^A)^2 + \left(\frac{J^{AB}}{d^B M_S^B} + \frac{J^{AB}}{d^A M_S^A}\right)^2 + (K^B - K^A)\left(\frac{2J^{AB}}{d^A M_S^A} - \frac{2J^{AB}}{d^B M_S^B}\right)\right\}^{1/2} \qquad 4.48$$

For $J^{AB}=0$ this equation leads to the resonant fields of the independent layers, see eq. 4.45. Let's assume that layers A and B have different magnetic properties, e.g. different uniaxial anisotropies. This will result in two different resonant fields, H_o^A and H_o^B, for $J^{AB}=0$ (see Figure 4.3). Let us assume that the layer A has a lower value of the resonant field compared with the layer B.

For an arbitrary J^{AB} there are two resonance modes in this model: firstly, the low-frequency acoustic mode in which all magnetizations are in phase and nearly parallel, and secondly, the optical mode in which the magnetizations of the two layers precess out of phase.

For antiferromagnetic coupling ($J^{AB}<0$) the position of the acoustic peak moves with an increasing $|J^{AB}|$ up from H_o^A gradually towards the fixed point which is given by eq. 4.47 (see Figure 4.3). The resonant field for the

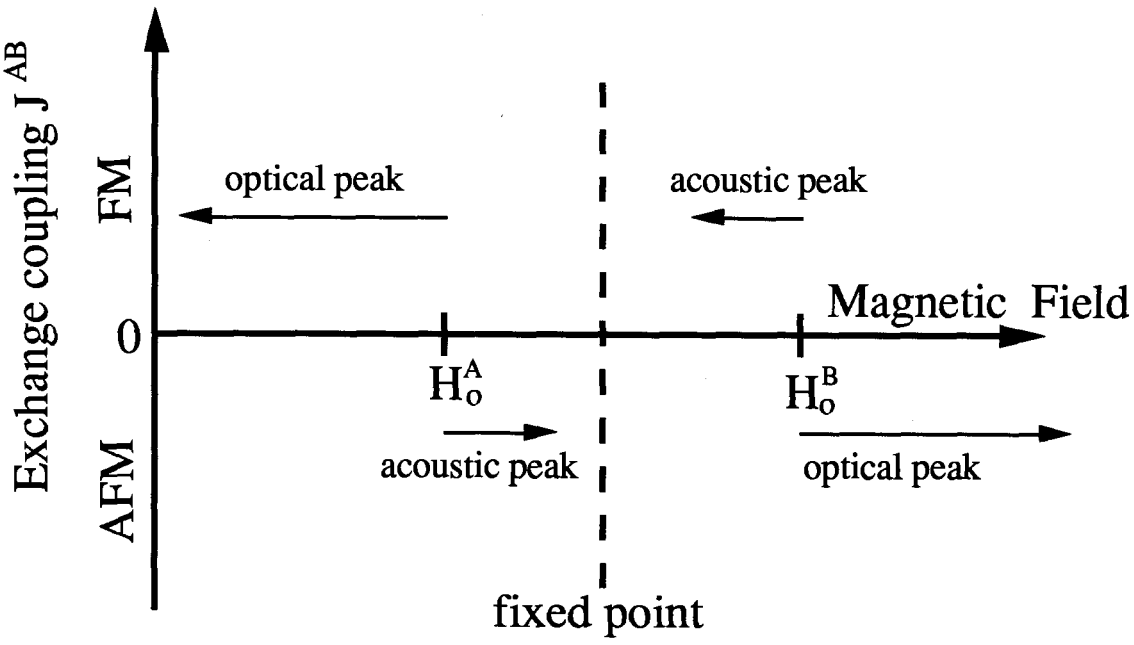

Fig. 4.3 Schematic diagram of the acoustic and optical peak positions for the ferromagnetic and antiferromagnetic coupling between two ferromagnetic layers separated by a non magnetic interlayer.

optical mode has its value larger than H_o^B. The intensity of the acoustic peak increases with an increasing $|J^{AB}|$ while intensity of the optical mode decreases. Figure 4.4a shows numerical results for antiferromagnetic coupling calculated for the *parallel* configuration. In the limit of very strong antiferromagnetic coupling the acoustic peak approaches the fixed point and its intensity is proportional to the total moment $d^A M_S^A + d^B M_S^B$.

For ferromagnetic coupling ($J^{AB}>0$) the acoustic peak is at a higher field than the optical peak, see Figure 4.3. The resonant field of the acoustic peak decreases with an increasing J^{AB} and reaches eventually a fixed point. The resonant field of the optical mode decreases rapidly with an increasing J^{AB} and is always lower than H_o^A. Figure 4.4b shows numerical results for ferromagnetic coupling calculated for the *parallel* configuration. The intensities of acoustic and optical modes behave as in the case of antiferromagnetic coupling. With an increasing ferromagnetic coupling the

intensity of the acoustic mode increases while the intensity of the optical mode decreases.

It can be shown that the optical mode is observable in a uniform driving field only if the magnetic properties of the individual layers A and B are different. If they are the same the resonant field for the acoustic mode for any J^{AB} is equal to $H_o = H_o^A = H_o^B$ and its intensity is proportional to the total moment of the two layers. The position of the optical mode depends on the value of the exchange coupling but for any J^{AB} the intensity for this mode is equal zero for a uniform rf driving field.

FMR measurements of the ultrathin layers were performed in the parallel configuration using a linearly polarized rf field. The resulting system of 4×4 equations leads to complicated solutions. Details of such calculation can be found in the paper by Heinrich et al. [4.2]. The measured experimental data were analyzed by comparison with numerical calculations. Figure 4.4 shows examples of computer calculations of the derivative of the rf susceptibility for different values of J^{AB}. Subsection 5.2 contains additional examples of computer calculations which are compared with the experimental data.

Appendix A contains descriptions of the FMR apparatus and the computer programs which were used to analyze the data.

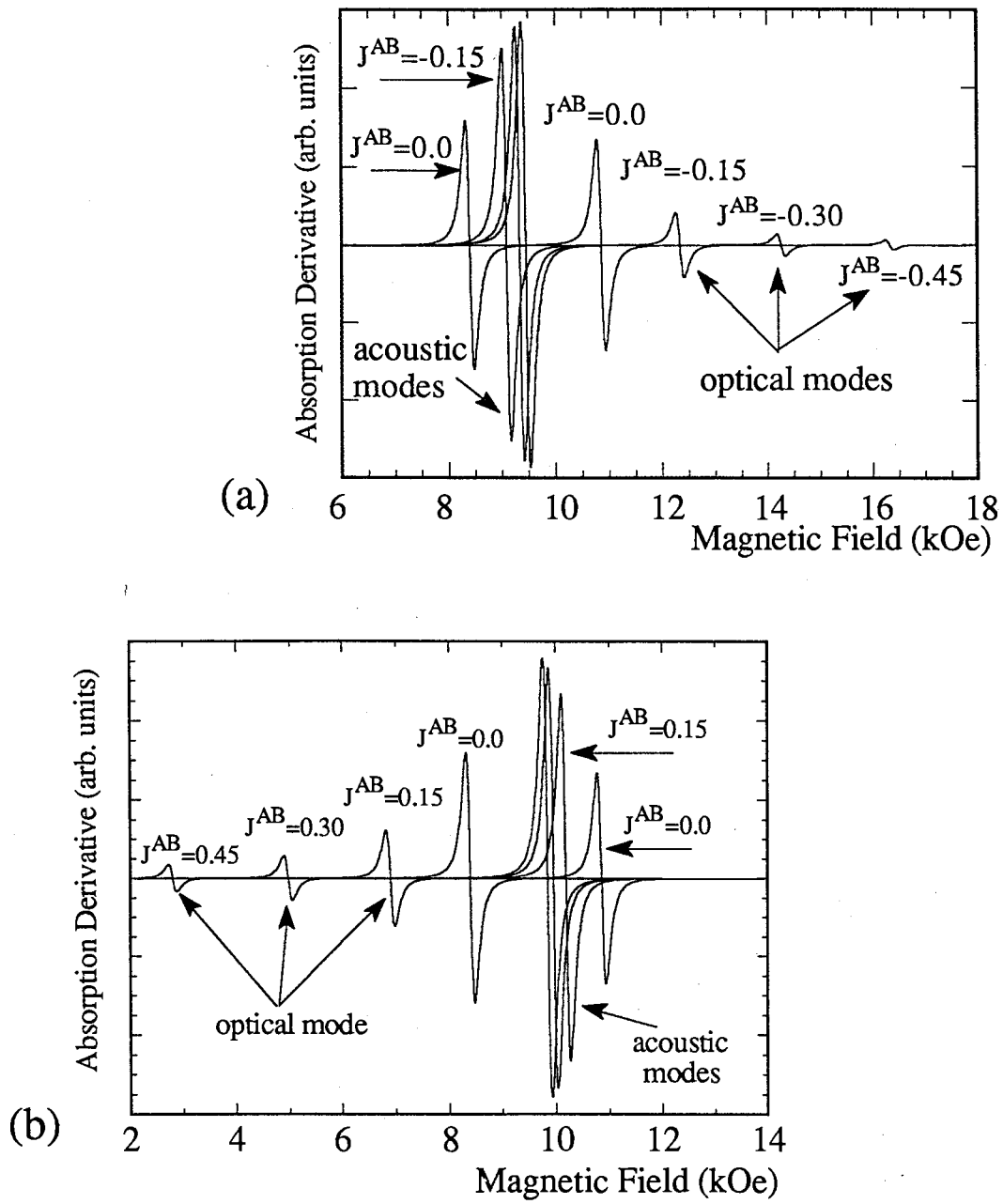

Fig. 4.4 The computer calculation of the absorption derivatives as a function of the applied dc magnetic field at 36.3 GHz for the system composed of two Fe layers. The magnetic parameters; $4\pi M_{eff}$=3.5, and 9.5 kOe for 5.7 and 5.5ML thick Fe layers respectively; the four fold in-plane anisotropy field $2K_{1||}^{eff}/M_S$=0.1kOe for both layers. (a) antiferromagnetic coupling; Note that the resonance field of the optical peaks increases with increasing J^{AB} while the intensity decreases. (b) ferromagnetic coupling; Note that the resonance fields of the optical peaks and their intensities decrease with increasing J^{AB}.

Chapter 5

The exchange coupling in Fe(001)/Cu,Pd,Ag,Au(001)/Fe(001) trilayers

5.1 Introduction

In this chapter magnetic studies of Fe(001)/X(001), X(001)/Fe(001) bilayers and Fe(001)/X(001)/Fe(001) trilayers are reported where X(001) denotes metastable bcc Cu(001), metastable fcc Pd(001), fcc Ag(001) or fcc Au(001). The main attention is paid to the exchange coupling between two ferromagnetic films separated by a nonmagnetic interlayer. Interest in the field of metallic MBE increased considerably by the discovery of antiferromagnetic coupling in Fe(001)/Cr(001)/Fe(001) structures [1.3]. Moreover the observation of the giant magnetoresistance in antiferromagnetically coupled $[Fe/Cr]_n$ superlattices [1.4] has raised expectations of exciting application of these structures in the future. A year ago magnetization measurements on sputtered Fe/Cr and Fe/Ru sandwiches [1.5] revealed long range oscillations with the period of ~ 10ML in the exchange coupling. In recent months short range oscillations, with the period of ~2ML, in the Fe/Cr/Fe systems were found by three groups [5.1, 5.2, 5.3].

Cr has an approximately half filled 3d band and it is antiferromagnetically ordered for temperatures below 311K. The oscillatory behavior of the exchange coupling between ferromagnetic layers separated by 3d and 4d transition elements such as Cr or Ru might be expected since both Cr and Ru

band structures possess sufficiently complex Fermi surfaces to allow long and short range RKKY-like coupling.

The investigations presented in this thesis were intended to extend our knowledge by studying the exchange coupling through interlayers with filled or nearly field d-bands such as Cu, Ag, Au and Pd. Cu, Ag, and Au have their d-bands filled and they are known to exhibit no magnetic tendencies. The metallic Pd has nearly filled 4d bands and is expected to have a strong tendency towards ferromagnetism.

Cu, Ag and Au form the 1B column of the Atomic Periodic Table. Their 3d, 4d and 5d shells are filled and they have one electron in their 4s-p, 5s-p and 6s-p conduction bands. Since there are some similarities in the electronic band properties of Cu, Ag and Au it might be expected that Ag(001) and Au(001) interlayers could facilitate the exchange coupling in a way similar to that of Cu(001).

Metallic Pd is different when compared with elements from the 1B column. Its 4d bands are not entirely filled. With a few holes, (1.0/atom), in the 4d bands the Fermi energy in metallic Pd is near the peak of the 4d electron density of states. In this case a Stoner instability tending towards ferromagnetism can be expected. The magnetic properties of metallic Pd have long fascinated physicists. The valence band of Pd metal is similar to that of Ni. Numerous attempts have been made to convert metallic Pd to the ferromagnetic state [5.4]. Several theoretical papers predicted interesting magnetic properties in metallic Pd. The nonrelativistic calculations of Moruzzi and Marcus [5.5] and of Chen et al. [5.6] predicted the onset of ferromagnetism in a 5% expanded fcc Pd lattices. Blügel et al. [5.7] showed in their calculation that a Pd substrate enhances the magnetic moment at the

Fe-Pd interface. The Fe interface moment is enhanced by $0.9\mu_B$ and the two nearest Pd atomic layers possess magnetic moments of $0.35\mu_B$ and $0.17\mu_B$ respectively. Recently Bouarab et al. [5.8] reported calculations for Pd slabs grown on Ag(001) using a self-consistent tight-binding calculation in the unrestricted Hartree-Fock approximation of the Hubbard Hamiltonian. The authors predicted that the onset of ferromagnetism in Pd slabs depends dramatically on the number of atomic layers. A magnetic moment was obtained only for Pd films in the thickness range of 2 to 5ML. Anomalous Hall effect measurements [5.9] showed that dilute Fe - surface atoms (~ 0.05 ML) covered with a few layers of Pd form giant moments which exhibit superparamagnetism. This result implies that Fe atoms polarize the nearest Pd atoms. SMOKE studies [5.10] of a submonolayer of Fe on a Pd(100) substrate suggests that Fe atoms induce moments on neighboring Pd sites. Brillouin Light Scattering studies [5.11] on very thin Pd(111) overlayers grown on an Fe(110) film template found evidence for the formation of magnetic moments at the Pd/Fe interface. The spin - polarized photoemission data by Weber et al. [5.12] showed that at least the first, and possibly the second, atomic Pd(001) layer possessed a magnetic moment.

Two circumstances should strongly affect the magnetic properties of Pd. Firstly, fcc Pd layers on Fe(001) templates grow with the lateral lattice spacing of Fe; the lateral spacing of Fe is 5.1% larger than that in bulk fcc Pd. Secondly, the proximity of ferromagnetic Fe layers should further enhance the onset of ferromagnetism in Pd through the hybridization of their 3d and 4d bands. Metallic Pd in Fe/Pd/Fe trilayers should be very inclined to become ferromagnetic.

FMR and SMOKE techniques were used to study the exchange coupling and the results are presented in this chapter. The Brillouin Light Scattering (BLS) studies carried out by Muir et.al. [5.13] and by Cochran et al. [5.14] on the same structures allowed one to answer the question of the uniformity of the structures which were prepared. In subsection 5.2 the results of magnetic studies of the Fe-Cu, Fe-Pd, Fe-Ag, and Fe-Au systems are presented. Finally, the summary of those studies is presented in subsection 5.3.

5.2 Results of magnetic studies

The results of magnetic studies of multilayers composed of bcc Fe(001), metastable bcc Cu(001), fcc lattice expanded Pd(001), fcc Ag(001) and fcc Au(001) are presented in this subsection. The role of the different interfaces on the perpendicular uniaxial and in-plane 4-fold anisotropies, were studied in bilayers structures using FMR [5.15]. The exchange coupling between two iron films separated by nonmagnetic interlayers was determined from FMR measurements. A phenomenological theory of the exchange coupling between ultrathin films [1.2] was used to interpret the experimental data and Chapter 3 provides a detailed account of this theory. In addition dc measurements of the antiferromagnetic coupling were carried out by means of SMOKE. The results of SMOKE measurements and their comparison with the FMR data are presented in this subsection.

5.2.1 Magnetism in ultrathin structures

The ultrathin structures studied consisted of two ferromagnetic layers which were thinner than the exchange length L_{ex}. Magnetic moments separated by a distance smaller than the exchange length are locked together by the exchange interaction and respond as a single unit to the total torque. The exchange length, $L_{ex} = [A_{ex},(2\pi M_s^2)]^{1/2}$, is given by a minimization of the exchange and dipolar energies: for iron $L_{ex} = 20ML$. Therefore Fe films thinner than 20ML have their magnetic moments locked together. Ferromagnetic structures thinner than L_{ex} will be referred to as "ultrathin".

Ultrathin (001) structures can be tetragonaly distorted. Therefore the magnetic anisotropy energy per unit volume can be expressed as

$$E_K = -\frac{1}{2}K_{1\parallel}^{eff}\left[\alpha_x^4 + \alpha_y^4\right] - \frac{1}{2}K_{1\perp}\alpha_z^4 - K_u^{eff}\alpha_z^2 \qquad 5.1$$

where α_x, α_y, α_z are the directional cosines with respect to the cubic axes, $K_{1\parallel}^{eff}$ describes the strength of the effective four fold in-plane anisotropy, and K_u^{eff} and $K_{1\perp}$ are the effective second order and fourth order terms for the perpendicular uniaxial anisotropy. The magnetic torques acting on the individual atomic moments are shared equally by all magnetic moments and therefore the surface anisotropies, $K_{1\parallel}^s$ and K_u^s, divided by the film thickness, d, appear as effective bulk anisotropies [5.16]. The total anisotropies combine the bulk and surface contributions:

$$K_{1\parallel}^{eff} = K_{1\parallel} + \frac{K_{1\parallel}^s}{d}; \quad K_u^{eff} = K_u + \frac{K_u^s}{d} \qquad 5.2$$

The FMR resonant field depends on the effective fields. The anisotropy fields are proportional to

$$H_{K_1} = \frac{2K_{1\perp}^{eff}}{M_S} \quad \text{and} \quad H_u = \frac{2K_u^{eff}}{M_S} \qquad 5.3$$

The second order perpendicular uniaxial anisotropy enters into the FMR equations of motion as an effective demagnetization field

$$4\pi M_{eff} = 4\pi D M_S - \frac{2K_u^{eff}}{M_S} \qquad 5.4$$

where D is the dipole-dipole demagnetization factor which is less than 1 for small numbers of atomic layers [1.2, 4.2].

5.2.2 Magnetic properties of Fe(001)-Cu(001) system

FMR studies of Fe(001)/Cu(001), Cu(001)/Fe(001) bilayers and Fe(001)/Cu(001)/Fe(001) trilayers are summarized in Table 5.1. At 300 K the Fe/Cu interface exhibits the second strongest interface anisotropy, K_u^S=0.67ergs/cm^2, among measured interfaces. The in-plane 4-fold anisotropies were found to be almost identical for all four of the studied interfaces at both 295 and 77K. The magnetic properties of the individual Fe layers changed very slightly when measured either separately or together in Fe/Cu/Fe trilayers - see Table 5.1. The only exception was observed in the 5.7Fe/7Cu/9.7Fe trilayer at 295K. In this sample the in-plane anisotropies were different from those in individual layers. However the strong ferromagnetic exchange coupling decreased the intensity of the optical peak so substantially that it made difficult to determine the peak positions along its easy and hard axes with better accuracy than ~ 100 Oe. The measured accuracy is comparable to the anisotropy fields involved, see Figure 5.2, and thus affecting strongly their trilayer values.

Table 5.1 Magnetic parameters of Fe(001)/Cu(001), Cu(001)/Fe(001) bilayers and Fe(001)/Cu(001)/Fe(001) trilayers. For trilayers the upper and lower values apply to the first (usually 5.7Fe) and to the second Fe film respectively.

Sample	$4\pi M_{eff}$ (kG)		$2K_{1\|\|}^{eff}/M_S$ (kG)		J^{AB} (ergs/cm^2)	
	295K	77K	295K	77K	295K	77K
5.7Fe/12Cu/20Au	3.08	1.72	0.112	0.282	-	-
5.7Fe/7Cu/20Au	2.76	0.94	0.117	0.324	-	-
5.7Fe/8Cu/42Au	3.01	0.91	0.140	0.378	-	-
8.7Fe/10.5Cu/20Au	7.47	4.52	0.281	0.499	-	-
5Cu/9.5Fe/20Au	12.69	12.64	0.216	0.401	-	-
20Cu/9.5Fe/20Au	12.88	12.45	0.221	0.364	-	-
9Cu/10Fe/20Au	13.50	13.75	0.257	0.285	-	-
12Cu/11Fe/20Au	14.54	14.45	0.304	0.454	-	-
10.5Cu/16Fe/20Au	16.36	16.66	0.389	0.521	-	-
5.6Fe/5Cu/9.7Fe	3.0 13.5	1.0 13.8	0.11 0.26	0.29 0.37	~1.5	~1.6
5.7Fe/6Cu/9.7Fe	3.15 14.10	1.75 14.25	0.13 0.33	0.29 0.44	~1.0	~1.0
5.6Fe/7Cu/9.7Fe	1.81 13.45	1.0 13.8	0.03 0.23	0.29 0.41	0.337	~0.5
5.6Fe/8Cu/9.7Fe	2.35 14.5	3.00 12.55	0.040 0.402	0.106 0443	0.048	0.119
5.75Fe/9.0Cu/9.7Fe	3.01 13.31	1.80 13.55	0.149 0.252	0.112 0.257	-0.103	-0.205

5.65Fe/9.5Cu/9.5Fe	3.01 13.31	1.80 13.05	0.195 0.231	0.233 0.405	-0.188	-0.379
8.7Fe/10.5Cu/15.3Fe	7.47 16.50	4.59 16.66	0.303 0.389	0.438 0.527	-0.216	-0.390
5.7Fe/11.6Cu/10.3Fe	3.08 13.47	1.1 13.8	0.252 0.112	0.29 0.41	-0.223	~-0.54
5.4Fe/12.6Cu/9Fe	2.73 15.16	1.55 15.35	0.166 0.258	0.373 0.413	-0.139	-0.238
5.7Fe/13.7Cu/9.8Fe	3.09 13.38	2.21 13.34	0.135 0.229	0.293 0.409	-0.081	-0.148
5.7Fe/16.3Cu/8.9Fe	2.27 14.07	3.08 13.85	0.118 0.229	0.356 0.374	0.006	0.026
5.7Fe/18.3Cu/10.3Fe	3.70 14.56	1.62 14.80	0.120 0.263	0.300 0.427	-0.017	-0.054
5.7Fe/20Cu/10.5Fe	3.06 14.38	1.80 14.49	0.075 0.241	0.238 0.380	-0.041	-0.091
5.7Fe/22Cu/10.7Fe	3.06 14.38	1.80 14.49	0.075 0.241	0.242 0.404	-0.035	-0.077
5.8Fe/25.5Cu/10Fe	3.07 14.09	1.74 14.16	0.080 0.206	0.243 0.357	-0.028	-0.065

Reconstructed Cu(001) overlayers did not enhance the 4-fold in-plane anisotropy in the Fe layer. Apparently the crystallographic defects created during the lattice reconstruction are not sufficient on their own to change the in-plane anisotropy. This result suggests that the observed large in-plane anisotropies in the lattice transformed Fe/Ni(001) bilayers [1.2] were caused by an additional magnetic energy created by the broken symmetry around the 4-fold network of crystallographic defects in Ni.

The surface of the Cu(001) template strongly affects the quality of the Fe(001) films. The FMR linewidth, ΔH, is a parameter used to characterize the quality of ultrathin films. The frequency independent part, $\Delta H(0)$, reflects the contribution of magnetic inhomogeneities [5.17]. The intrinsic Gilbert damping parameter, G, is proportional to the slope of the linearly dependent part of the FMR linewidth [5.18]. Fe layers grown on unreconstructed Cu templates exhibited an isotropic FMR linewidth ($\Delta H(0)$ ~15 Oe). On the other hand the Fe layers grown on reconstructed Cu templates showed an anisotropic behavior in both the zero frequency FMR linewidth and the intrinsic damping parameter. $\Delta H(0)$ in these samples is small (~15 Oe along the hard axis and ~45 Oe along the easy axis) which shows that Fe films grown on reconstructed Cu(001) film templates maintain their high magnetic quality. Details of these studies can be found in [5.19].

The exchange coupling was measured using Fe/Cu/Fe trilayers. Figure 5.1 shows the exchange coupling as a function of Cu interlayer thickness at 295 and 77K. Trilayers having a bcc Cu(001) interlayer thinner than 9ML exhibited only ferromagnetic coupling. Trilayers with 7 and 8ML thick interlayers showed two resonance peaks. The weaker peaks (corresponding to optical modes) were located at lower fields than their acoustic counterparts indicating clearly a weak ferromagnetic coupling ($J^{AB} < 0.4$ ergs/cm^2) - see Figure 5.2. For smaller Cu thicknesses (d = 5, 6ML) only acoustic modes were observed. The exchange coupling in these samples was determined by using the acoustic peak position only. In this case the interpretation of measured results is quite inaccurate (~25%). In measurements in which both peaks were observed the accuracy with which the exchange coupling was determine was much better. The error was

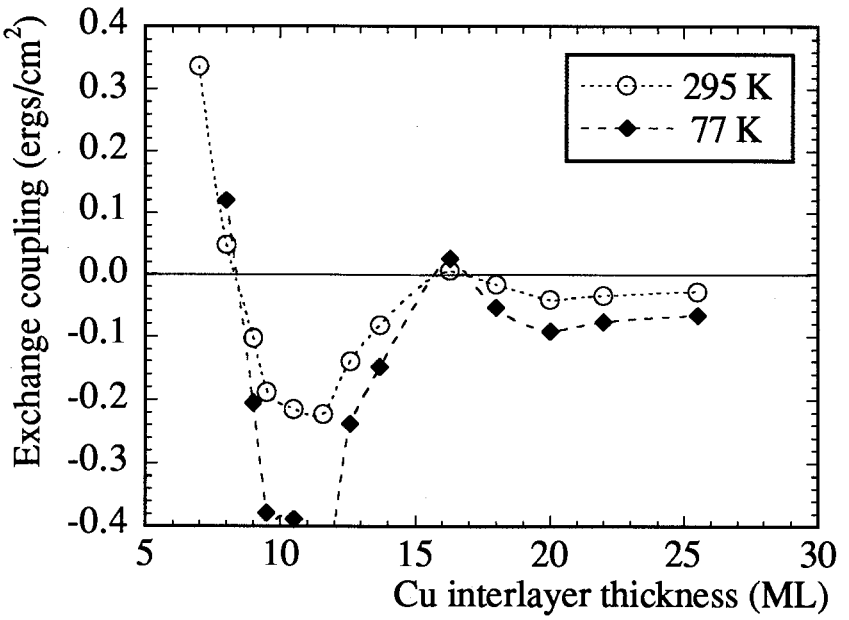

Fig. 5.1 The thickness dependence of the exchange coupling J^{AB} in 5.7Fe/Cu/9.7Fe trilayers. Close and open symbols correspond to 77 and 295K respectively. Dashed lines have been added to help guide the reader's eye. The error in J^{AB} and interlayer thickness is smaller than the symbol size.

estimated to be ±0.006 and ±0.008 ergs/cm^2 at 295 and 77K respectively.

For Cu interlayers thicker than 8ML the exchange coupling became antiferromagnetic. Figure 5.3 shows an example of FMR measurements for antiferromagnetically coupled layers. The FMR optical peak is at a higher field than the acoustic peak indicating clearly that the coupling between two Fe layers through a 9ML thick Cu interlayer is antiferromagnetic. The antiferromagnetic coupling reached the first broad maximum at 10.5 - 11.5ML thick Cu interlayer, see Figure 5.1. It is interesting to note that the strength of the exchange coupling is not affected by the onset of bcc Cu reconstruction. The exchange coupling in Cu increases appreciably with decreasing temperature for all Cu thicknesses and preserves its sign. The

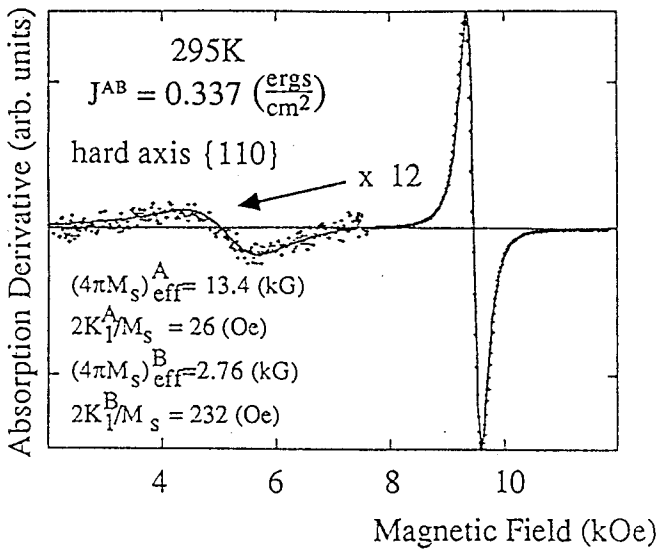

Fig. 5.2 The field derivative of FMR absorption along the hard axis in the 5.7Fe/7Cu/9.7Fe trilayer at 295 K. The solid line was calculated using the theory of exchange coupled Fe layers. The optical mode is located at a lower magnetic field than the acoustic peak and therefore the exchange coupling is ferromagnetic. A fitting routine was used to match the resonance fields of the optical and acoustic modes along the easy and hard magnetic axes with the theory.

sample with 13.7ML of Cu exhibited a monotonically increasing antiferromagnetic coupling (almost a factor of 2) when the temperature decreased from 295 to 77K - see Figure 5.4. This increase is substantially larger than that expected from the temperature dependence of the saturation magnetization M_S, and therefore the exchange coupling mechanism is not due to dipole-dipole interactions but it originates in the electron spin transport properties. The exchange coupling through 8ML thick Cu exhibited a non monotonic dependence on temperature, see Figure 5.4. This may not be a surprising result, if it is realized that the exchange coupling in this sample is in the region of the crossover from ferromagnetic to antiferromagnetic coupling.

The magnetic coupling in Fe/Cu/Fe trilayers exhibits an oscillatory behavior, see Figure 5.1. However after the first crossover the exchange

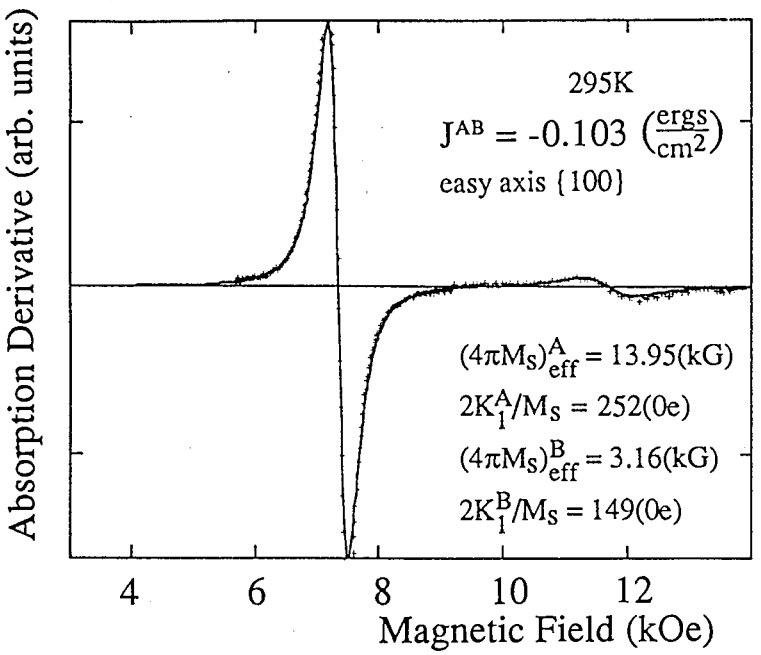

Fig.5.3 The field derivative of FMR absorption along the easy axis in the 5.7Fe/9Cu/9.7Fe trilayer at 295 K. The solid line was calculated using the theory of exchange coupled Fe layers. The A and B labels represent the constituent Fe layers 9.7 and 5.7 ML thick respectively. The magnetic parameters of the individual Fe layers were determined in separate measurements using 9.5Cu/10Fe and 5.7Fe/12Cu bilayers. The magnetic properties in the individual Fe layers are depicted in Table 5.1. Note that the magnetic parameters of Fe layers in the 5.7Fe/9Cu/9.7Fe trilayer are nearly the same as those measured in the individual Fe layers. The optical mode is located at a higher magnetic field than the acoustic peak and therefore the exchange coupling is antiferromagnetic.

coupling remains antiferromagnetic. The periodicity is ~10ML which is similar to that observed for Cr and Ru [1.5]. Short range oscillations (~2ML) were not observed in Fe/Cu/Fe trilayers grown at room temperature. Recent studies on Fe/Cu/Fe trilayers with the last three monolayers of the first Fe layer grown at elevated temperature (150 °C) showed 2 ML oscillation on the envelope of long range oscillations. Details of these studies will be published by Heinrich et al. [5.20]. These results indicate that the roughness due to the Henzler structure (see subsection 4.4) averages

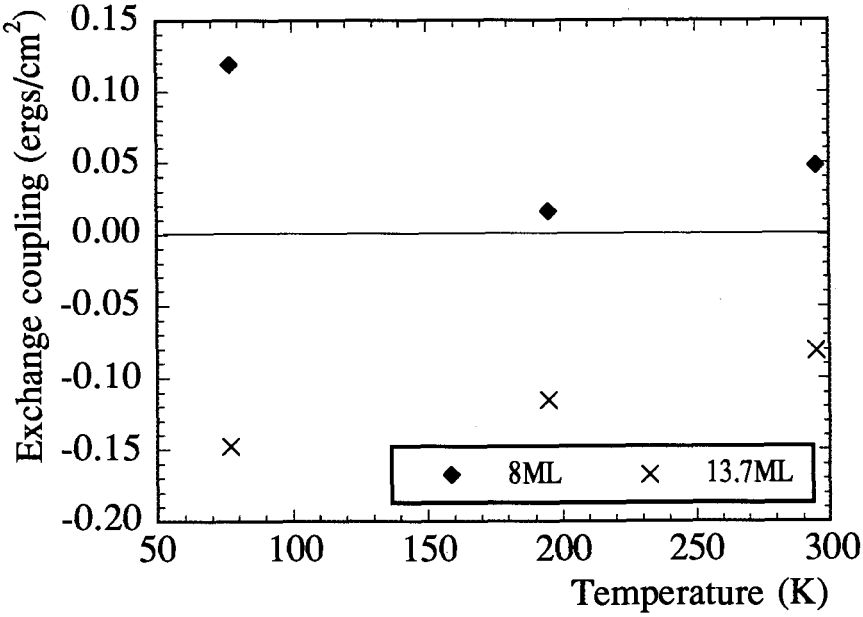

Fig. 5.4 The exchange coupling coefficient J^{AB} as a function of temperature in Fe/Cu/Fe trilayers with 8 and 13.7 ML thick Cu interlayer.

out the short wavelength oscillations.

The antiferromagnetic exchange coupling determined from SMOKE measurements were in good agreement with the results obtained from the FMR measurements. The SMOKE data from the 5.7Fe/9.5Cu/9.7Fe trilayer are shown in Figure 5.5. The strength of the antiferromagnetic coupling is determined from the value of the applied dc field, H_e, at which the magnetic moments start to rotate away from the applied magnetic field direction. Assuming the rotational process a minimization of the interface, Zeeman, and anisotropy energies (with applied dc field along the easy magnetic axis) results in

$$H_e + \frac{2K_{1\parallel}^{eff}}{M_S} = \frac{4J^{AB}}{M_S}\left(\frac{1}{d_A} + \frac{1}{d_B}\right) \qquad 5.6$$

where d_A and d_B are the thicknesses of the individual Fe layers. For small

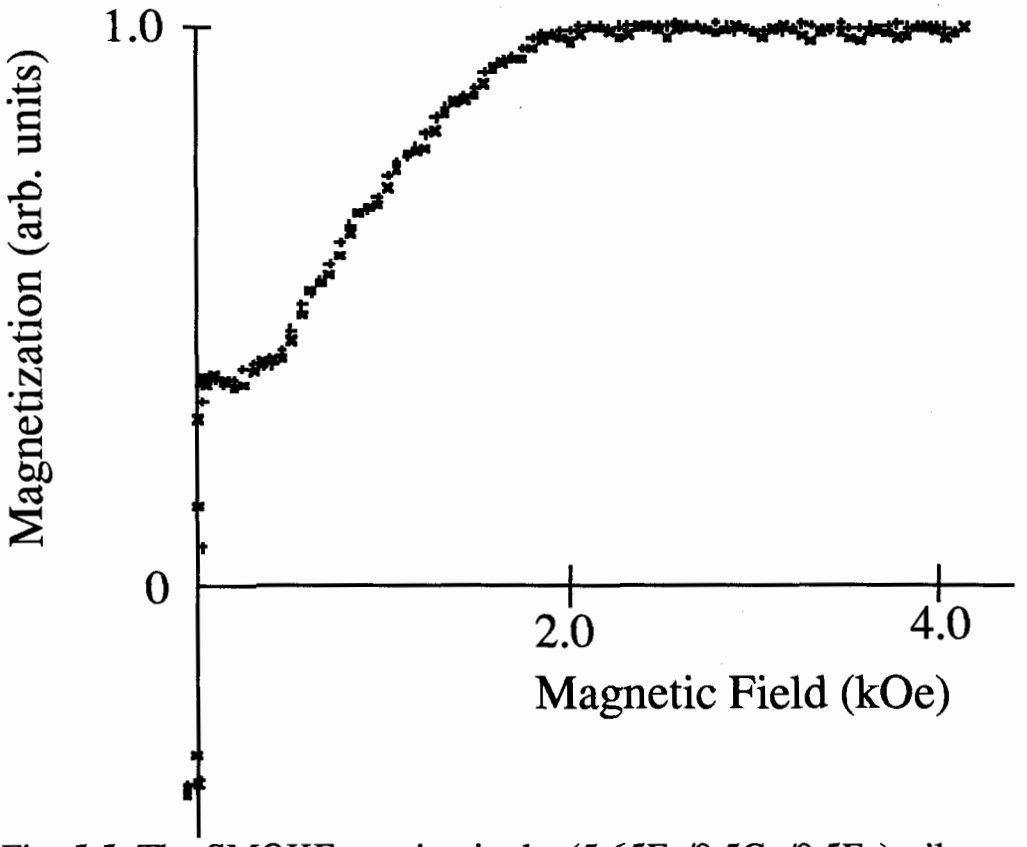

Fig. 5.5 The SMOKE rotation in the (5.65Fe/9.5Cu/9.5Fe) trilayer with the magnetic field along the magnetic easy, {100} direction. For H<2kOe Fe magnetic moments rotate away from the applied field. For H<500 Oe the moments in the two layers are opposed reducing the total magnetic moment by nearly 1/3 as expected. For H<40 Oe, the net magnetic moment reverses its direction.

enough dc fields the antiferromagnetic coupling overcomes the torque of applied field and results in the antiferromagnetic configuration, reducing the magnetization almost by factor of 3. In the neighborhood of zero fields the magnetic moments suddenly reverse their direction by a domain wall nucleation and a subsequent propagation - see the changing sign of the SMOKE signal in Figure 5.5. The exchange coupling from the SMOKE measurements is, J^{AB} =-0.19 ergs/cm^2, which is very close to the value obtained from FMR, J^{AB} =-0.188 ergs/cm^2.

In FMR measurements an area 13mm in diameter is probed by the microwaves. In BLS measurements the laser beam was focused on an area ~20 μm in diameter. Good agreement between FMR and BLS results for the exchange coupling indicates that the studied Fe/Cu/Fe trilayers were very uniform on the μm scale. For the same Fe/Cu/Fe trilayers the optical peak linewidth was broader than expected from individual layer linewidths. This broadening is attributed to a lateral variation of the exchange coupling. The additional line broadening can be used to estimate the distribution of the exchange coupling across the interlayer surface. The total linewidth

$$\Delta H = \left((\Delta H)^2_{intrin} + (\Delta H)^2_{inhom} \right)^{1/2} \qquad 5.7$$

where $(\Delta H)_{intrin}$ is the intrinsic linewidth of the individual layers and $(\Delta H)_{inhom} = \lambda^{-1} 2\Delta J^{AB}$. λ is an approximated linear slope of J^{AB} around the optical peak position and ΔJ^{AB} is the distribution of the exchange coupling. Figure 5.6 shows the distribution of ΔJ^{AB} as a function of Cu interlayer thickness. These results indicate that values of ΔJ^{AB} are correlated with the magnitudes of the rates of change of the J^{AB} with Cu interlayer thickness, producing a minimum at 11.5ML.

The strength of the exchange coupling in bcc Cu(001) is weaker than that observed in Cr. The first maximum in the antiferromagnetic coupling in Cr was found for thinner interlayers (5ML). It is interesting to note that the strength of the exchange coupling in Cr is very dependent on the growth [1.3, 1.5, 5.21]. Recent studies by Bennett et al.[5.22], Parkin et al.[5.23], Mosca et al. [5.24] and Miranda et al. [5.25] showed that fcc Cu(001) interlayers also provide antiferromagnetic coupling with the period of oscillations somewhat shorter in ML (8ML), but very similar in Å (15Å), to that observed in bcc Cu.

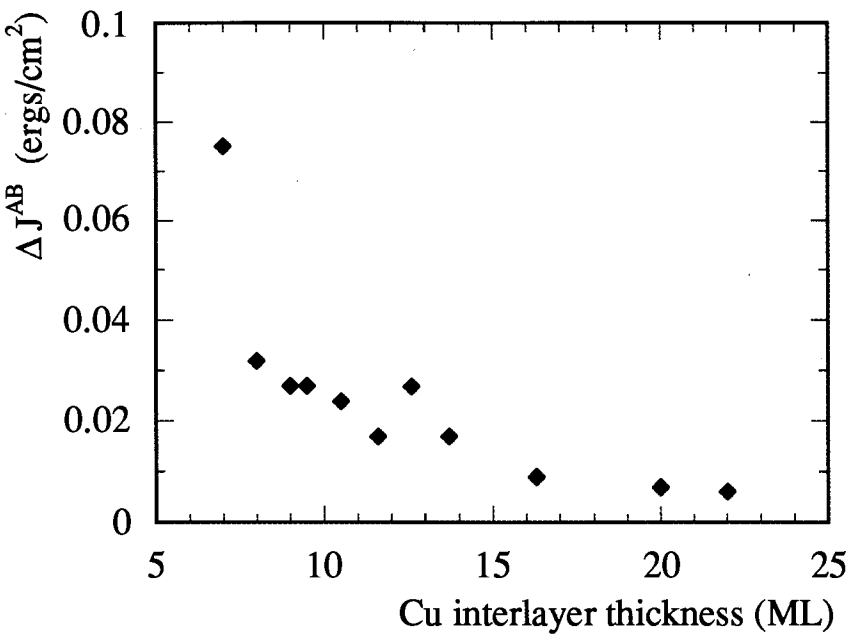

Fig. 5.6 The thickness dependence of the exchange coupling distribution ΔJ^{AB} in Fe/Cu/Fe trilayers.

The symmetry of exchange coupling oscillations in these studies could not be verified since the SMOKE measurements were unable to determine quantitatively the strength of the ferromagnetic coupling. The maximum value of the antiferromagnetic coupling at room temperature in both structures, bcc and fcc Fe/Cu/Fe, are very similar, $J^{AB} \sim -0.24$ ergs/cm^2 [5.22], in spite of the fact that the maximum of the antiferromagnetic coupling in fcc Cu(001) occurs at shorter distances (5ML in [5.22, 5.24] and 8ML in [5.23]) than in bcc Cu(001).

In conclusion: The crossover from the ferromagnetic to antiferromagnetic coupling occurred at 8ML and the antiferromagnetic coupling reached the first broad maximum at 10.5 - 11.5 ML [5.26, 5.27, 5.28]. The exchange coupling exhibits an oscillatory behavior and remains antiferromagnetic with the periodicity of ~10ML (15Å) [5.29, 5.30].

5.2.3 The magnetic properties of Fe(001)-Pd(001) system

FMR studies of Fe(001)/Pd(001), Pd(001)/Fe(001) bilayers and Fe(001)/Pd(001)/Fe(001) trilayers are summarized in Table 5.2. The Fe/Pd interface exhibited the weakest interface anisotropy, K_u^s=0.17ergs/cm^2 [5.15], among all four of the systems studied at 300 K. The magnetic parameters of the individual Fe layers, such as the 4-fold in-plane anisotropy field ($2K_{1||}^{eff}/M_S$) and the effective magnetization ($4\pi M_{eff}$), remained unchanged in Fe/Pd/Fe trilayers. Therefore the exchange coupling is the only variable which is strongly dependent on the Pd(001) interlayer thickness. This fact is illustrated by Figure 5.7.

The exchange coupling in Fe/Pd/Fe trilayers revealed several interesting regimes. The thickness dependences of the exchange coupling at 295, 195 and 77K are shown in Figure 5.8. The exchange coupling decreases with an increasing thickness in a non trivial manner. An oscillatory behavior superimposed on the monotonically decreasing background is clearly visible. The oscillations in Pd are again not symmetric as was reported for Ru interlayers [1.5]. The short wavelength period, 4ML, in metallic Pd is larger than that period of Cr, 2ML, [5.1, 5.2, 5.3].

The temperature dependence identifies two regions. For Pd interlayer thicknesses less than 8ML the exchange coupling is strongly dependent on temperature. The temperature dependence is appreciably weaker for 8 and 8.5ML thick Pd interlayers. For thicknesses greater than 9ML the exchange coupling is small and the observed differences at various temperatures are within experimental errors. Clearly the physics of the exchange coupling changes with changing Pd thickness.

Theoretical predictions [5.8] suggest that a 4ML Pd interlayer possesses

Table 5.2 Magnetic parameters of Fe(001)/Pd(001), Pd(001)/Fe(001) bilayers and Fe(001)/Pd(001)/Fe(001) trilayers. For the trilayers the upper and lower values apply to the thinner and thicker Fe films respectively.

Sample	$4\pi M_{eff}$ (kG)		$2K_{1\|\|}^{eff}/M_s$ (kG)		J^{AB} (ergs/cm^2)	
	295K	77K	295K	77K	295K	77K
5.7Fe/8Pd/20Au	9.40	10.71	0.116	0.238	-	-
5.6Fe/7Pd/20Au	9.48	10.91	0.112	0.223	-	-
5.7Fe/7Pd/20Au	9.35	10.59	0.109	0.225	-	-
5.7Fe/8Pd/20Au	9.22	9.87	0.106	0.231	-	-
8Pd/9.6Fe/20Au	16.94	18.56	0.171	0.303	-	-
5.7Fe/4Pd/9.8Fe	9.40 16.94	10.71 18.56	0.116 0.171	0.238 0.303	~0.7	~0.9
5.7Fe/5Pd/9.6Fe	9.97 16.49	10.92 18.47	0.110 0.243	0.192 0.307	0.113	0.301
5.7Fe/5.5Pd/9.6Fe	9.9 16.87	10.14 18.18	0.149 0.193	0.186 0.329	0.071	0.217
5.7Fe/6Pd/9.8Fe	9.38 16.93	10.51 18.52	0.119 0.192	0.238 0.363	0.043	0.189
5.7Fe/7Pd/10.2Fe	9.25 17.74	9.8 19.31	0.143 0.193	0.228 0.304	0.058	0.177
5.7Fe/8Pd/9.6Fe	9.06 16.85	10.32 18.70	0.113 0.199	0.266 0.391	0.078	0.102
5.7Fe/8.5Fe/10.1Fe	9.40 17.72	10.45 18.91	0.112 0.193	0.225 0.331	0.034	0.047
5.7Fe/10Pd/9.6Fe	9.30 16.85	10.67 18.63	0.111 0.219	0.235 0.358	0.017	0.018

5.7Fe/11Pd/9.6Fe	9.44 16.73	10.93 18.30	0.108 0.209	0.232 0.339	0.027	0.018
5.7Fe/13Pd/9.3Fe	9.40 17.20	10.71 18.60	0.117 0.206	0.226 0.350	-0.014	-0.004
5.7Fe/14.3Pd/9.4Fe	9.36 17.19	10.71 18.58	0.101 0.206	0.220 0.356	-0.014	-0.014
5.7Fe/16Pd/9.3Fe	9.40 16.80	10.71 18.40	0.114 0.194	0.247 0.340	-0.004	-0.011
5.7Fe/18Pd/9.4Fe	9.50 16.95	10.80 18.38	0.105 0.194	0.243 0.330	0.00	0.00

an appreciable magnetic moment ($0.2\mu_B$) in its central region. In ferromagnetically ordered Pd one should expect a strong ferromagnetic coupling between Fe layers and indeed, in a 4 ML thick Pd interlayer only the acoustic mode was observed. However one additional atomic layer of Pd decreased the exchange coupling sufficiently that the optical mode could be observed. This is definitely a weak coupling. The temperature dependence of the exchange coupling in this sample (5.7Fe/5Pd/9.6Pd trilayer) was almost inversely proportional to the absolute temperature, T, following the Curie-Weiss type of dependence ~ $1/(T+\theta)$, see Figure 5.9. This behavior indicates the presence of fluctuating magnetic moments in Pd. The exchange field of the surrounding Fe layers polarizes the fluctuating Pd magnetic moment. This contribution is ferromagnetic and obviously dependent on temperature and gradually decreases with increasing Pd thickness. A 5ML thick Pd interlayer does not possess a long range ferromagnetic order.

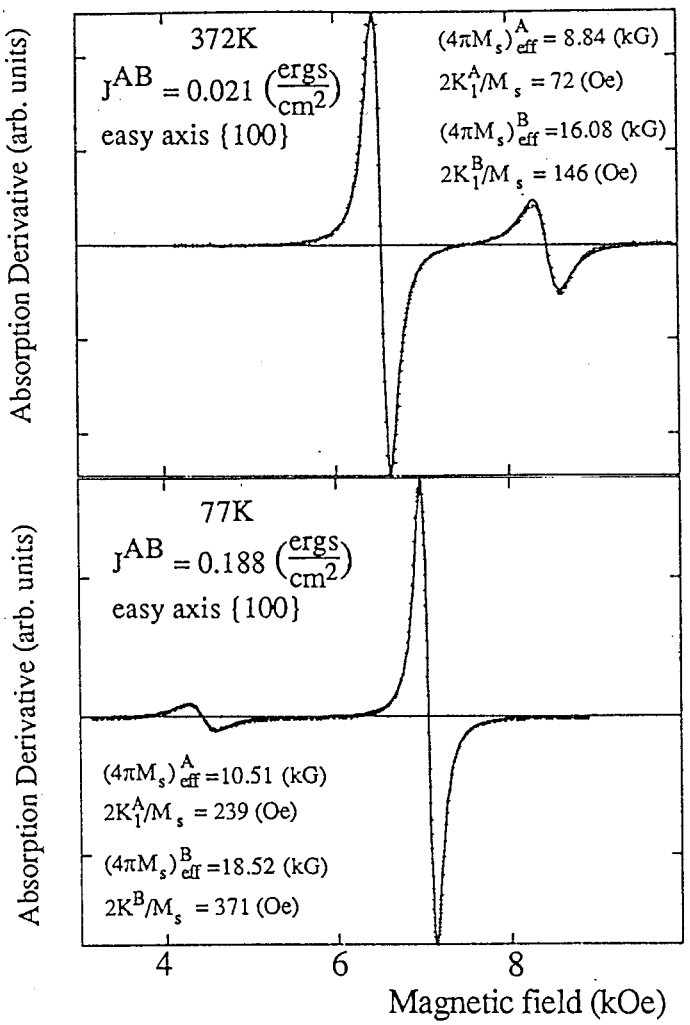

Fig. 5.7 The field derivative of FMR absorption at 36 GHz in the (5.7Fe/6Pd/9.8Fe) trilayer (+) at 372 and 77K . The solid line was calculated using the theory of exchange coupled Fe layers [1.2] with magnetic parameters (inserted in figure) obtained from a chi-square fit. The magnetic parameters of individual 5.7Fe/8Pd and 8Pd/9.6Fe bilayers are shown in Table 5.2. A denotes the 5.7ML Fe layer and B denotes the 9.8ML Fe layer.

Epitaxial Pd layers did not grow in a pure fcc expanded lattice. X-ray diffraction studies of a Pd layer grown on Fe(001) templates [3.8] showed that the vertical lattice spacing decreased. The Pd atomic volume increased only by 2% compared with 15% expected in the lattice expanded Pd grown on Fe(001), see subsection 4.4. X-ray diffraction data show that

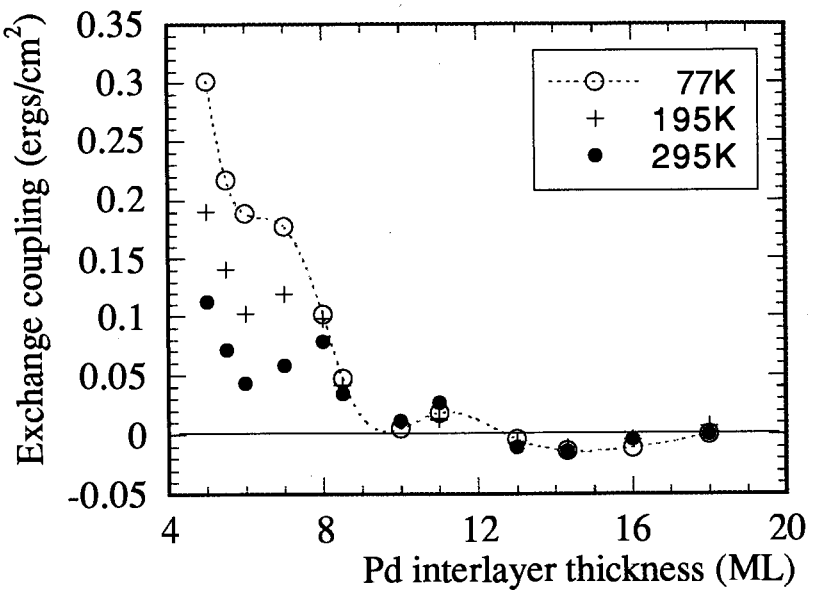

Fig. 5.8 The thickness dependence of the exchange coupling J^{AB} in 5.7Fe/Pd/9.6Fe trilayers. Dashed line have been added to help guide the readers eye. The error in JAB and the interlayer thickness is smaller than the symbol size.

ferromagnetic order is not able to support the vertical expansion of the Pd lattice [5.6, 5.7, 5.8]. The observed result contradicts a popular view that the metallic Pd needs just a little push to become ferromagnetic.

For Pd interlayers thicker then 12ML the exchange coupling became antiferromagnetic. The maximum of the antiferromagnetic coupling was found to be ~14ML (see Figure 5.8). The Surface Magneto-Optical Kerr Effect (SMOKE) was used to confirm this weak antiferromagnetic coupling (~-0.01 ergs/cm^2) which was measured by the FMR technique. Figure 5.10 shows the result of SMOKE measurements in the 5.7Fe/14Pd/9.4Fe trilayer with the dc magnetic field along the easy {100} direction which clearly indicates an antiferromagnetic coupling. The strength of antiferromagnetic coupling, J^{AB}=-0.008 ergs/cm^2, was deduced from the value of the field, H_e,

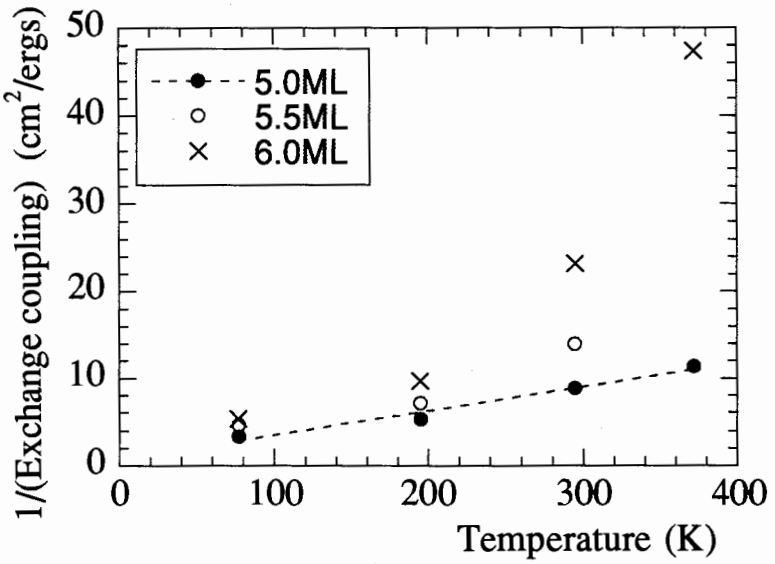

Fig. 5.9 The inverse of the exchange coupling as a function of temperature in 5.7Fe/xPd/9.6Fe for x=5, 5.5, 6ML.

at which the magnetization started to rotate away from the direction of the applied field. The thickness of the Fe layers used in this trilayer was chosen to be small in order to decrease the role of the in-plane four fold anisotropy in the SMOKE measurements. The role of the Pd(001) surface reconstruction on the exchange coupling is not entirely clear. However the bcc Cu(001) interlayer undergoes also a similar surface reconstruction (d ~ 10 - 11ML) in Fe/Cu/Fe trilayers. Yet no noticeable effect of the Cu surface reconstruction on the exchange coupling was observed in Fe/Cu/Fe trilayers. Therefore it is very likely that the crossover to the antiferromagnetic coupling in Pd is caused by the intrinsic properties of thick Pd and not by a surface roughening associated with the Pd surface reconstruction. This hypothesis is further supported by the fact that a maximum of the antiferromagnetic coupling occurs at ~ 14ML and the

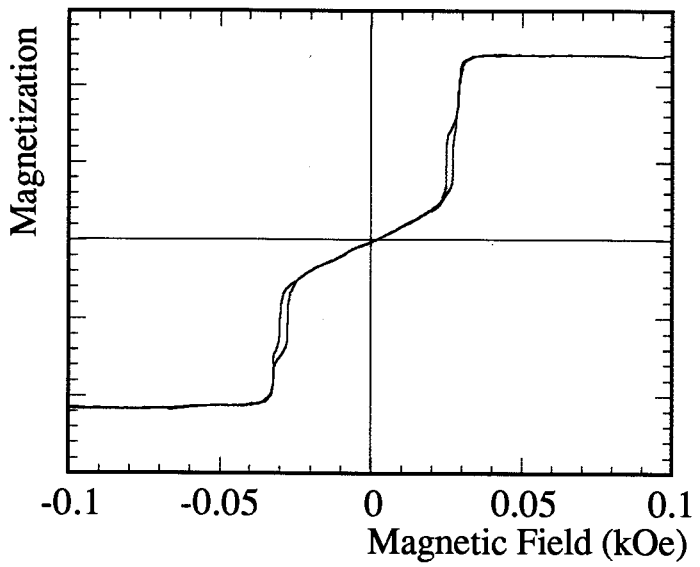

Fig 5.10 The SMOKE rotation in the 5.7Fe/14Pd/5Fe trilayer with the magnetic field along the magnetic easy axis [100].

exchange coupling decreases to nearly zero at 16-17ML. The exchange coupling caused by an interface roughness would not decrease rapidly with an increasing interlayer thickness.

Good agreement between FMR and BLS results for the values of the exchange coupling J^{AB} indicates that the studied Fe/Pd/Fe trilayers were again very uniform across the whole surface on the BLS probe scale. In studied Fe/Pd/Fe structures the optical peak linewidth was broaden only for trilayers with 5 and 5.5ML thick Pd interlayers. It is estimated that ΔJ^{AB}=0.0075 and 0.003 ergs/cm^2 ($\Delta J^{AB}/J^{AB}$=6.5 and 4%) for 5 and 5.5 thick Pd interlayer.

In conclusion: It was found that metallic Pd does not exhibit a long range ferromagnetic order for films thicker than 4 ML despite the fact that it is surrounded by ferromagnetic Fe layers. Pd atoms possess a fluctuating magnetic moment for films thinner than 8ML [5.31]. In the thickness range from 4 to 12ML the exchange coupling between two Fe layers is

ferromagnetic and weak, yet it exhibits an oscillatory behavior with a period of ~ 4ML [5.30, 5.32]. The crossover from the ferromagnetic to the weak antiferromagnetic coupling occurs at 12 ML and the antiferromagnetic coupling shows a broad maximum at ~14ML [5.30, 5.32].

5.2.4 The magnetic properties of Fe(001)-Ag(001) system

FMR studies of Fe(001)/Ag(001), Ag(001)/Fe(001) bilayers and Fe(001)/Ag(001)/Fe(001) trilayers are summarized in Table 5.3. The Fe/Ag interface has the highest interfacial anisotropy among all four studied systems, K_u^s=0.69 ergs/cm^2 [5.15] at room temperature. The magnetic properties of the individual Fe layers ($4\pi M_{eff}$ and $2K_{1||}^{eff}/M_s$) changed very slightly when measured either separately or together in Fe/Ag/Fe trilayers - see Table 5.3.

Despite the fact that Ag belongs to the 1B group of elements together with Cu, the exchange coupling between two Fe(001) layers with an Ag(001) interlayer exhibits a completely different behavior compared to that in Fe/Cu/Fe trilayers. Figure 5.11 shows the exchange coupling as a function of the Ag interlayer thickness at 295 and 77K. The exchange coupling in Fe/Ag/Fe trilayers is temperature independent. The ferromagnetic exchange coupling decreases rapidly with increasing interlayer thickness. It reaches zero at ~ 7ML and remains decoupled for thicker interlayers. Similar results were recently reported by Grünberg's group [5.33].

The absence of the exchange coupling for Ag interlayers thicker than 7ML is a surprising result. To study this unique behavior, new trilayer structures were grown. The trilayer 8.8Fe/11Cu/16Fe exhibits a strong antiferromagnetic coupling. It was interesting to determine the effect of

Table 5.3 Magnetic parameters of Fe(001)/Ag(001), Ag(001)/Fe(001) bilayers and Fe(001)/Ag001)/Fe(001) trilayers. For the trilayers the upper and lower values apply to the first (usually 5.7Fe) and to the second Fe film respectively.

Sample	$4\pi M_{eff}$ (kG)		$2K_{1\|\|}^{eff}/M_S$ (kG)		J^{AB} (ergs/cm)	
	295K	77K	295K	77K	295K	77K
5.7Fe/7Ag/13Au	1.99	1.21	0.092	0.204	-	-
5.5Fe/7Ag/20Au	1.98	1.21	0.093	0.218	-	-
6.3Fe/24Ag/26Au	5.04	4.88	0.144	0.289	-	-
10.9Fe/7Ag/13Au	9.34	6.84	0.358	0.543	-	-
10.9Fe/7Ag/20Au	9.55	7.06	0.361	0.544	-	-
3Ag/5.5Fe/20Au	5.81	7.20	0.082	0.194	-	-
6.1Fe/4Ag/12.2Fe	4.23 12.81	2.66 12.90	0.205 0.331	0.354 0.613	0.425	0.407
6.1Fe/5.5Ag/12.2Fe	3.18 13.42	2.01 12.92	0.125 0.416	0.339 0.542	0.100	0.094
6.1Fe/7Ag/12.4Fe	2.87 13.95	1.88 13.07	0.218 0.397	0.306 0.548	-0.009	-0.008
5.7Fe/7Ag/5.6Fe	2.02 6.00	1.25 7.20	0.083 0.089	0.219 0.201	0.017	0.017
5.7Fe/9-10Ag/5.6Fe	1.74 6.05	1.22 7.28	0.027 0.080	0.053 0.085	0.00	0.00
5.8Fe/13Ag/5.7Fe	2.35 6.14	1.56 7.60	0.103 0.098	0.219 0.232	0.00	0.00

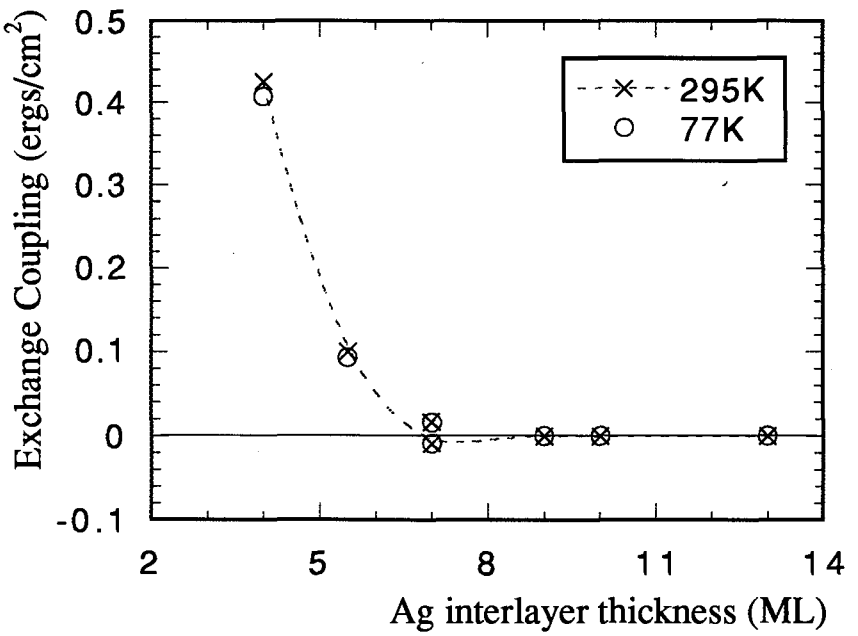

Fig.5.11 The thickness dependence of the exchange coupling J^{AB} in 6.2Fe/Ag/12.4Fe and 5.7Fe/Ag/5.7Fe trilayers. Dashed line have been added to help guide the reader's eye. The error JAB and interlayer thickness is smaller than the symbol size.

adding Ag(001) atomic layers to the already antiferromagnetically coupled Fe/Cu/Fe trilayers. The replacement of one atomic Cu(001) layer by Ag (8.8Fe/10Cu/1Ag/16Fe) resulted in an appreciable decrease of the antiferromagnetic coupling (by a factor of 2). Two atomic layers of Ag (8.8Fe/4Cu/2Ag/5Cu/16Fe and 8.8Fe/9Cu/2Ag/16Fe) were sufficient to completely suppress relatively strong antiferromagnetic coupling in Fe/Cu/Fe trilayers. This result show that Ag(001) interlayers have a very strong tendency to eliminate the exchange coupling. Similar results were reported in the Fe-Cr system by B.A. Gurney et al. [5.34].

The termination of the growth of the first Fe layer either at a minimum or at a maximum of RHEED oscillations did not lead to any

noticeable changes of the exchange coupling in Fe/Ag/Fe trilayers. The optical peak linewidth was significantly broadened only for the trilayer with a 4 ML thick Ag interlayer. It was estimated that $\Delta J^{AB} = 0.11$ ergs/cm^2 ($\Delta J^{AB}/J^{AB} \sim 27\%$). In trilayers with 5.5, 7, 9, and 13 ML thick Ag interlayers the observed line broadening was much smaller resulting in $\Delta J^{AB} = 0.011$, 0.008, 0.005 and 0.004 ergs/cm^2 respectively

In conclusion: It was found that the exchange coupling in Fe/Ag/Fe trilayers is ferromagnetic and rapidly decreases to zero at ~7ML and remains at this value for thicker interlayers. The exchange coupling is temperature independent [5.30].

5.2.5 The magnetic properties of Fe(001)-Au(001) system

The FMR studies of Fe(001)/Au(001), Au(001)/Fe(001) bilayers and Fe(001)/Au(001)/Fe(001) trilayers are summarized in Table 5.4. The surface uniaxial anisotropy, K_u^S, in the Fe/Au interface is equal to 0.40 ergs/cm^2 [5.15] at 300K. The magnetic properties of the individual Fe layers ($4\pi M_{eff}$ and $2K_{1||}^{eff}/M_S$) changed very slightly when measured either separately or together in Fe/Au/Fe trilayers - see Table 5.4.

Figure 5.12 shows the exchange coupling as a function of the Au interlayer thickness at 295 and 77K. Trilayers having the fcc Au(001) interlayer thinner than 11ML coupled the Fe layers ferromagnetically. The exchange coupling in Fe/Au/Fe trilayers is nearly temperature independent. The ferromagnetic exchange coupling decreases with an increasing interlayer thickness. The crossover in Fe/Au/Fe trilayers from ferromagnetic to antiferromagnetic coupling was observed at 11ML. Note that the crossover occurred at a thicker interlayer than observed in Fe/Cu/Fe

Table 5.4 Magnetic parameters of Fe(001)/Au(001), Au(001)/Fe(001) bilayers and Fe(001)/Au(001)/Fe(001) trilayers. For the trilayers the upper and lower values apply to the first (usually 5.7Fe) and the second Fe film respectively.

Sample	$4\pi M_{eff}$ (kG)		$2K_{1\|\|}^{eff}/M_s$ (kG)		J^{AB} (ergs/cm^2)	
	295K	77K	295K	77K	295K	77K
5.7Fe/20Au	6.27	6.93	0.100	0.233	-	-
5.7Fe/20Au	6.10	7.54	0.119	0.223	-	-
5.7Fe/50Au	6.17	7.44	0.094	0.255	-	-
5.7Fe/20Au	5.98	7.34	0.088	0.200	-	-
10.2Fe/20Au	11.44	9.70	0.327	0.470	-	-
12.5Fe/20Au	13.6	12.81	0.281	0.355	-	-
9Au/4.95Fe/20Au	10.21	12.23	0.020	0.083	-	-
12.3Fe/7Au/4.75Fe	13.7 9.96	12.80 12.10	0.300 0.040	0.350 0.050	0.117	0.116
5.65Fe/9.5Au/4.95Fe	6.61 9.99	7.88 12.05	0.090 0.010	0.209 0.055	0.028	0.045
5.75Fe/11Au/4.9Fe	6.25 10.05	7.75 12.05	0.075 0.016	0.202 0.047	0.000	0.008
5.65Fe/13Au/5.25Fe	6.17 10.35	7.48 12.37	0.075 0.016	0.202 0.047	-0.022	-0.004
5.85Fe/16Au/5.55Fe	6.27 10.15	7.53 12.23	0.105 0.007	0.217 0.050	0.015	0.017

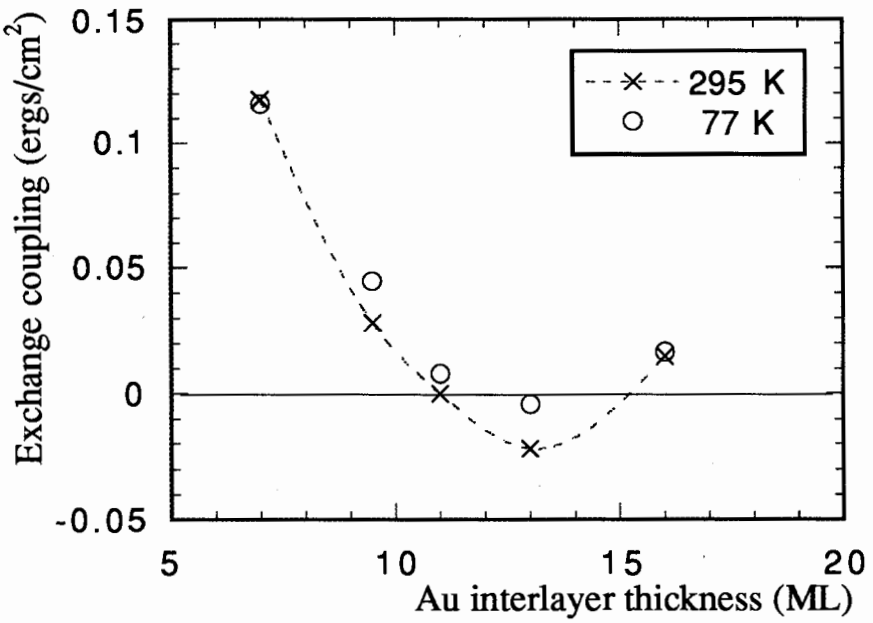

Fig.5.12 The thickness dependence of the exchange coupling J^{AB} in 5.7Fe/Au/5.4Fe trilayers. Dashed line have been added to help guide the reader's eye. The error in J^{AB} and interlayer thickness is smaller than the symbol size.

trilayers. The measured value of the antiferromagnetic coupling obtained using FMR was very weak. For a 13 ML thick Au interlayer J^{AB} = -0.022 ergs/cm^2. The observed value of the antiferromagnetic coupling was 10 times smaller than the maximum of the antiferromagnetic coupling in Fe/Cu/Fe trilayers at 300K. Figure 5.13 shows the result of SMOKE measurements in the 5.85Fe/13Au/5.25Fe trilayer with the dc magnetic field along the [100] direction. This figure clearly indicates a weak antiferromagnetic coupling. Its value, J^{AB}=-0.01 ergs/cm^2, was deduced from the value of the field, H_e, at which the magnetization begins to rotate away from the direction of applied field. The thicknesses of Fe layers in this trilayer were chosen to be small in order to decrease the role of the four fold

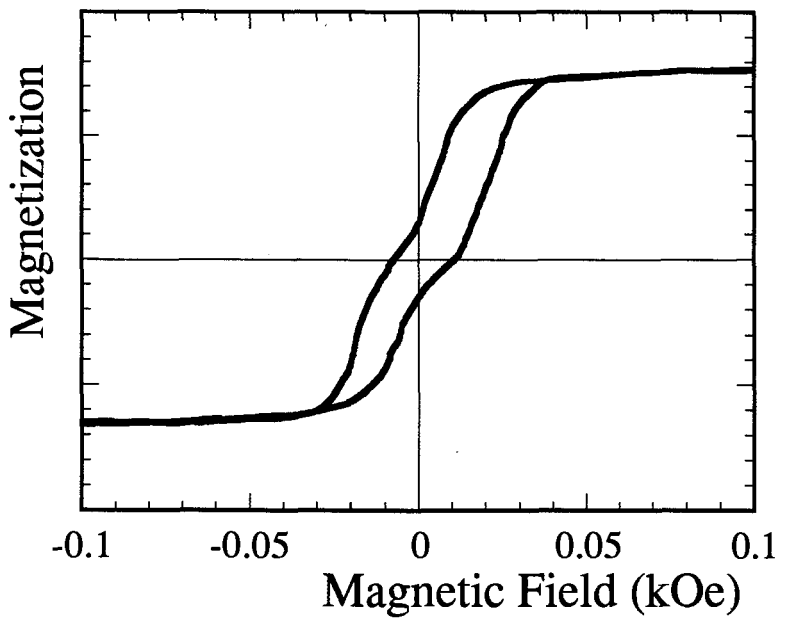

Fig. 5.13 The SMOKE measurement in the 5.65Fe/13Au/5.25Fe trilayer with the magnetic field along the easy axis [100] ($K_{1\|}/M_S$~0.10 kOe).

in-plane anisotropy in SMOKE measurements. For 16ML thick Au interlayer the exchange coupling became ferromagnetic again.

In Fe/Au/Fe structures the observed FMR optical peak line broadening was small. An estimated ΔJ^{AB} = 0.012, 0.008, 0.006, 0.006, and 0.004 ergs/cm^2 for 7, 9.5, 11, 13, and 16 ML thick Au interlayers respectively.

In conclusion: It was found that the exchange coupling in Fe/Au/Fe trilayers is ferromagnetic for Au interlayers thinner than 11ML and then it crosses over to a weak antiferromagnetic coupling. A maximum value of antiferromagnetic coupling, -0.022 ergs/cm^2, was observed for 13ML thick Au interlayer. The exchange coupling is temperature independent [5.30].

5.3 Discussion and conclusions

This thesis contains the results of magnetic studies carried out on ultrathin Fe(001) structures. The Fe(001)/X(001), X(001)/Fe(001) bilayers and Fe(001)/X(001)/Fe(001) trilayers were grown by MBE techniques on Ag(001) single crystal substrates. Eleven different epitaxial structures were characterized using RHEED and AES techniques:
Fe(001) on Ag(001) single crystal substrates,
Fe(001) on Cu(001), Pd(001), Ag(001) and Au(001) templates,
Cu(001), Pd(001), Ag(001), and Au(001) on Fe(001) templates,
Cu(001), and Pd(001) on Ag(001) single crystal substrates.
The understanding of RHEED pattern features and RHEED intensity oscillations permitted determination of the main growth characteristics.

It was found that bcc Fe(001) grows at room temperature with the two top layers partially covered. The recent STM results by Dr. J. Stroscio and coworkers showed [5.35] that the Fe(001) growth indeed proceeds that way. At the same time his studies added greatly to our understanding of the physics of RHEED intensity oscillations. RHEED intensity maxima occurred when the top atomic layer consists of numerous but separated atomic islands. On the other hand at the RHEED intensity minima the top atomic islands strongly coalesced and only a few new atomic islands are formed on the top of the coalescent atomic layer. These results indicate that the intensity of the diffracted beams depend strongly on the electron beam attenuation along the sample surface. The SFU group showed [2.11] the importance of the electron beam attenuation (for a small electron impinging angle ($<1.5^{o}$) in the initial stage of Fe(001) growth. Stroscio and coworkers STM results [5.35] indicate that for small impinging angles this mechanism is important for the entire

growth.

The growth of Cu(001), Pd(001) and Ag(001) on Fe(001) templates does not show the Henzler streak splitting which was observed for the template. Their RHEED patterns sharpen and lose the Henzler streak splitting after only one additional atomic layer was deposited. Clearly the tops of Cu, Pd and Ag layers are terminated by significantly larger atomic terraces than those observed in Fe. This configuration smears out very effectively the short wavelength components of the exchange coupling. Well defined 2ML exchange coupling oscillations reported in Fe/Cr/Fe systems [5.1, 5.2, 5.3] were not observed in the above studied Fe/X/Fe structures. This result is expected considering the nature of the Fe/X and X/Fe interfaces.

The ability to grow Cu and Pd on a Fe(001) template is non trivial. In fact entirely new epitaxial phases were discovered [5.26, 5.31]. Metastable bcc Cu(001) films were grown up to ~11ML before these layers underwent a complex lattice reconstruction. Metastable fcc Pd(001) layers maintained the in-plane symmetry and spacing of the Fe(001) template indicating that the in-plane palladium lattice was laterally expanded. The volume per Pd atom was increased (2%) compared with that of bulk Pd, even with the accompanying vertical contraction. A weak surface reconstruction occurs in Pd(001) layers thicker then ~12ML.

The exchange coupling in Fe/X/Fe trilayers exhibited a rich variety of trends especially as function of the interlayer thickness and temperature. The fact that a wide variety of structures were grown under the same conditions using Ag(001) single crystals substrates is very useful. It allows one to rule out any ambiguities which emerge when the systems are grown under

different conditions. Systems grown under similar circumstances can be compared and discused within the framework of existing theoretical models.

At the present time the theory of exchange coupling is being strongly debated [5.36 - 5.43]. Understanding is still limited. The theoretical studies are carried out using either first principles calculations based on the spin polarized local density approximation or employing various simplified models. The exchange coupling energy is a very small fraction of the total energy. Conclusions from the first principles band calculations are uncertain due to the numerical errors involved. It appears that the results of recent numerical calculations by Herman et al. [5.36] represent significant progress in this matter.

Simple model calculations are based on a generalization of the RKKY interaction. The Edwards and Mathon model [5.37] is based on the exchange confinement of the interlayer electrons by the ferromagnet/interlayer interfaces. Their main conclusion is that the exchange coupling and particularly the observed periodicities are determined by the topology of the interlayer Fermi surface. The electron nesting, between the stationary parts of the Fermi surface which are perpendicular to the sample surface plays a dominant role. Edwards and Mathon pointed out the importance of inter-zonal transitions with a short spanning k vector and showed that they are responsible in their model for the long range exchange coupling. Levy and coworkers [5.38] and Garcia and Hernando [5.39] based their calculations on the hybridization between the interlayer and ferromagnetic electrons. Their respective treatments of the electron hybridization are very different and they also came to very different conclusions. Both groups obtained ferromagnetic and antiferromagnetic

contributions to the exchange coupling. Levy [5.38] predicts that the antiferromagnetic contribution decreases exponentially to zero and therefore the long range coupling remains RKKY like. On the contrary the other group obtained a very weakly decreasing antiferromagnetic coupling which becomes dominant with increasing interlayer thickness.

FMR studies of Fe/X, X/Fe bilayers and Fe/X/Fe trilayers revealed that the magnetic properties, such as $4\pi M_{eff}$ and $2K_{1||}^{eff}/M_S$, of the individual layers remain practically unchanged when incorporated into trilayer structures. The exchange coupling coefficient J^{AB} was the dominant fitting parameter. This shows that the magnetic properties of stable bcc Fe(001) layers are very little affected by proximity effects (see Tables 5.1-5.4). This observation is not true in general, see metastable fcc Co(001) on fcc Cu(001) [4.2].

The exchange coupling between two Fe(001) layers through metastable bcc Cu(001) is unique among 1B elements. Among Fe/Cu, Pd, Ag, Au/Fe structures the Fe/Cu/Fe trilayers exhibited the strongest antiferromagnetic coupling. A strong temperature dependence and the strength of the exchange coupling show that its origin is not in the dipole-dipole interaction but it is most likely caused by the electron spin transport properties of the interlayers. The measured crossover from ferromagnetic to antiferromagnetic coupling at 8ML and a maximum of the antiferromagnetic coupling at ~ 10.5-11.5ML appears to be partially explained by the recent first principle calculations by Herman et al. [5.36]. To obtain agreement between the theory and the data one would need to replace the Cu interlayer thickness in Figure 5.1 by Angstroms to get the thickness dependence of the exchange coupling as obtained from the

numerical calculations [5.36]. That is the Cu interlayer thickness in the numerical calculations has to be expanded by 40% in order to be in agreement with experiment. In addition the first principle calculations showed a sharp, ~2ML wide, dip in the exchange coupling around the point where the experimental results showed a broad maximum in the antiferromagnetic coupling. The calculated dip is presumably due to the presence of short wavelength variations in the exchange coupling.

The Henzler streak splitting disappears entirely by growing the last few atomic layers of Fe at elevated temperatures, T ~150 ^{o}C. That way the atomic terraces of the first Fe layer become comparable to those of Cu overlayers. The resulting Fe/Cu/Fe trilayers are more likely to exhibit short wavelength oscillations in the exchange coupling than those grown at 295K only. Indeed Fe/Cu/Fe trilayers prepared that way exhibited a 2ML wide dip in the antiferromagnetic exchange coupling [5.20] as predicted by Herman et al. [5.36].

The Cu interlayers which are thicker then 12 ML show a noticeable lattice transformation. The exchange coupling in these trilayers remain antiferromagnetic with the second maximum in the antiferromagnetic coupling around 30Å. The separation between antiferromagnetic maxima suggests that the Fe/Cu/Fe trilayers exhibit a long wavelength periodicity of 15Å in the region beyond reconstruction. The same long wavelength periodicity was observed in subsequent studies carried out on fcc Fe/Cu/Fe and Co/Cu/Co systems [5.22 - 5.25].

Deaven et al. [5.43], Edwards and Mathon [5.37] and Herman et al. [5.36] proposed that the exchange coupling periodicity, λ, is related to the Fermi nesting $2\Delta k$ vector and it is given by relation

$$\lambda = \frac{2\pi}{(2\Delta k)} \qquad 5.8$$

see Figure 5.14. For the fcc Cu lattice along the Γ–X direction this results in λ~7ML which is close to that observed in the fcc Fe/Cu/Fe and Co/Cu/Co systems [5.22 -5.25]. Similarly the wavelength of the exchange coupling in bcc Cu can be established in the same way, however the reciprocal space of the bcc lattice has to be taken into account. For one electron per atom the Fermi sphere occupies half of the first zone (BZ)

$$\frac{4\pi k_F^3}{3} = \frac{1}{2}\left(\frac{2(2\pi)^3}{a^3}\right).$$

Therefore the radius of the spherical Fermi surface is $k_F = 0.62\frac{2\pi}{a}$, where a is the bcc lattice spacing and 2π/a corresponds to the reciprocal lattice vector of the first BZ. The bcc Cu nesting vector

$$2\Delta k_F = 2\left(\frac{2\pi}{a} - k_F\right) = 0.76\frac{2\pi}{a}.$$

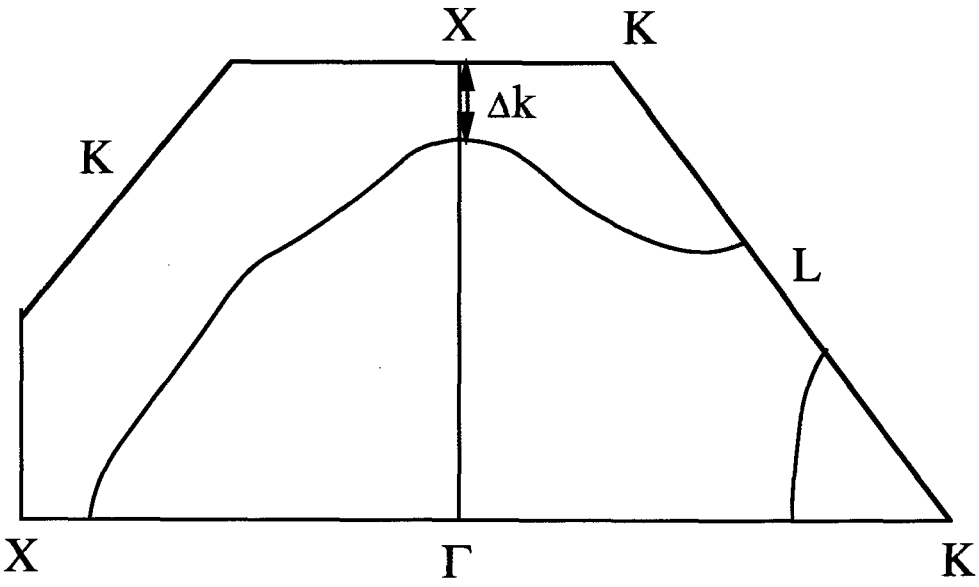

Fig. 5.14 A schematic diagram of Fermi surface profile for fcc Cu - unfolded irreducible zone. Γ-X is along [001] which is perpendicular to the film surface.

According to Formula 5.8, $\lambda \sim 2.6$ML. This wavelength is clearly significantly shorter than that observed experimentally. An appreciable stretch (~40%) of the Fermi surface ($k_F = 0.9\frac{2\pi}{a}$) along the [001] direction would be needed to explain the observed long wavelength periodicity. However it is probable that the Cu(001) lattice transformation results in a significant deviation from the bcc structure. A similar behavior was found in the lattice transformed Ni(001) grown on bcc Fe(001) [1.2]. The nearest neighbor atomic configuration of the lattice transformed Cu may be closer to that of fcc Cu. The similar periodicities observed in bcc Fe/Cu/Fe and fcc Fe/Cu/Fe may be a consequence of the lattice transformation of bcc Cu interlayer.

There is an alternative explanation by Garcia and Hernando [5.39]. In their calculations localized Cu electron levels lead to a long range antiferromagnetic coupling. The long wavelength oscillations, which do not cross to ferromagnetic coupling, are attributed in their calculations to additional in-plane k vectors which arise from the surface roughness. Their calculations describe the long wavelength variations of the exchange coupling through Cu.

The exchange coupling in Fe/Ag/Fe and Fe/Au/Fe trilayers exhibited different behavior compared with that of Fe/Cu/Fe. The exchange coupling in Fe/Ag/Fe trilayers was temperature independent and ferromagnetic. It reaches zero value for 7ML thick Ag interlayers and remains at this value for thicker Ag interlayers. The observed increase in FMR linewidth suggests only very weak symmetric oscillations ($\pm$ 0.005 ergs/cm^2) in the exchange coupling. These results seems to contradict predictions by Garcia and Hernando [5.39]. However it is important to note that the Fe-Cu

hybridization is significant while Fe does not hybridize well with Ag [5.44] and therefore their calculation are not as applicable in their present form to Fe/Ag/Fe.

The Fe/Au/Fe structures showed a weak antiferromagnetic coupling. The exchange coupling is temperature independent as in Fe/Ag/Fe trilayers. These results again do not support the Garcia - Hernando model [5.39]. However the top most atomic layers of the Au(001) interlayer are strongly reconstructed and corrugated, which may affect the exchange coupling.

For thick interlayers the Garcia and Hernando model leads always to the antiferromagnetic coupling with negligible short wavelength oscillations. The recent results on Fe/Cu/Fe system [5.20] showed that the RKKY behavior prevails especially in the thick interlayer limit. Therefore the Garcia - Hernando model can be useful only for special cases.

The Fe/Pd/Fe trilayers exhibited interesting behavior. A relatively weak ferromagnetic exchange coupling was observed for Pd interlayers thinner than 12ML. Then the exchange coupling crosses over to a weak antiferromagnetic coupling and reaches its maximum at 14ML. The recent calculations by Garcia and Hernando predicted a crossover to the antiferromagnetic coupling in Fe/Pd/Fe trilayers for Pd thicker than 12 ML [5.39]. The observed oscillatory behavior in the exchange coupling with a periodicity of 3-4ML was superimposed on a monotonically decreasing background. The first principles band calculations by Chen et al. [5.6] allow one to estimate the periodicities of the exchange coupling in fcc Pd(001). The stationary point , see Figure 5.15, of the large belly shaped sheet will contribute significantly to the exchange coupling through Pd. Formula 5.8 with $2\Delta k=0.7\,\frac{2\pi}{a}$, see Figure 5.15, results in the periodicity λ of 3ML which

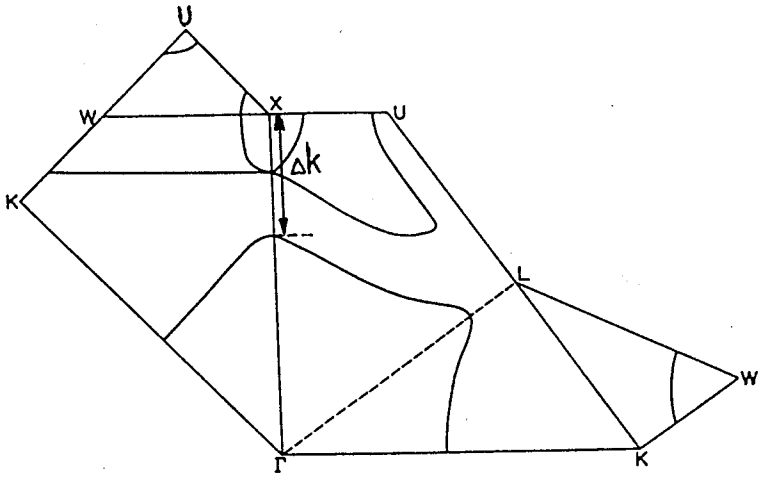

Fig. 5.15 A schematic diagram of Fermi surface profile for fcc Pd - unfolded irreducible zone [5.6]

is close to that observed in the lattice expanded Fe/Pd/Fe systems. The exchange coupling exhibited a strong temperature dependence for Pd interlayers thinner than 8ML. For the 5ML thick Pd interlayer it was almost inversely proportional to the absolute temperature, T, following the Curie-Weiss type of dependence ~ $1/(T+\Theta)$. This may indicate the presence of fluctuating magnetic moments in Pd which are polarized by the exchange field of the surrounding Fe layers. It is generally believe that the metallic Pd need just a little push to become ferromagnetic [5.4]. The exchange coupling behavior in Fe/Pd/Fe trilayers does not support this point of view. The metallic Pd was laterally expanded by 5% and was surrounded by ferromagnetic Fe layers. The lateral lattice expansion and the strong hybridization between Fe and Pd valence bands should result in ferromagnetic Pd. Contrary to this expectation the metallic Pd(001) found its minimum energy by contracting its lattice vertically and showed no long range ferromagnetic order for Pd interlayers thicker than 4ML.

Appendix A

Measurements of the exchange coupling using Ferromagnetic Resonance

This appendix describes measurements of the exchange coupling between two ferromagnetic layers separated by a non magnetic interlayer using FMR. The subsection A.1 provides an introduction to the FMR technique. The detailed procedure of measurements of the exchange coupling using FMR and the description of computer programs, which were used for data acquisition and data analysis are given in subsection A.2.

A.1 Ferromagnetic Resonance technique.

Most of the FMR measurements were carried out at 36 GHz and a few at 9, 24, and 73 GHz. A simple diagram of the 36 GHz FMR spectrometer is shown in Figure A.1. The specimens formed the end-wall of a microwave cavity. The microwave cavity operating in the TE_{012} mode was particularly useful since the cylindrically symmetric rf magnetic field mode permitted full 360^{o} in-plane angular FMR studies. As the applied in-plane dc magnetic field was rotated about the cavity axis, the component of the microwave cavity rf field perpendicular to the dc field did not change. The microwave power with electric component E_o was supplied by a klystron. The microwave power is partly reflected and partly absorbed by the microwave cavity which terminates the end of the waveguide.

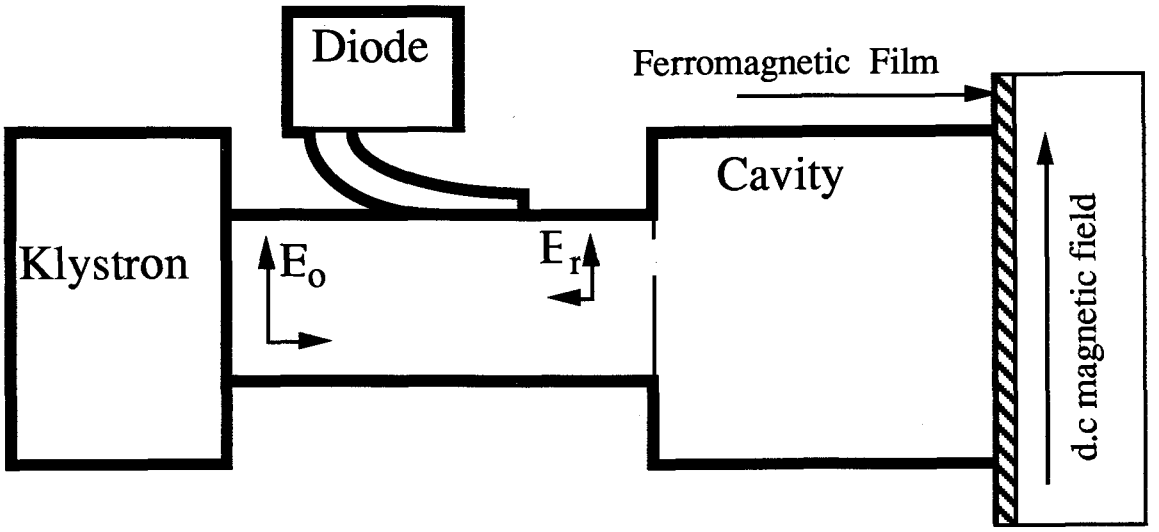

Fig. A.1 A schematic diagram of the FMR spectrometer.

The cavity is coupled to the waveguide through a small coupling hole, see Figure A.1. The frequency of the microwaves was kept constant by using a lock-in feedback technique. The dc magnetic field was swept through an appropriate range. In the vicinity of a resonant field the amount of absorbed microwave power changed, altering E_r. The signal was detected by a point-contact diode that generated a voltage proportional to the reflected amplitude E_r. The dc magnetic field was weakly modulated at 176 Hz. The dc component of the diode signal was collected by a computer controlled acquisition system. The amplitude 176 Hz component from the diode was measured using was a lock-in amplifier to improve the signal to noise ratio. For small modulation this signal is proportional to the field derivative of the microwave absorption.

The ultrathin ferromagnetic film absorbs power from the microwave field h_{rf}. This power absorption, P_{abs}, is associated with the imaginary part of the rf susceptibility χ'' of the films, $P_{abs} \sim \omega\chi''h_{rf}^2$. The ultrathin trilayers grown on Ag substrates are much thinner than then skin depth. In these

experiments h_{rf} is independent of depth within the sample. The detector diode was used to set the rf power level. The measurements were carried out with a constant incoming power. Changes in diode voltage will depend on changes in the quality factor Q_{int} of the cavity. There are five Q factors:

Loaded Q: $$Q_L = \frac{2\pi(\text{energy stored})}{\text{total energy lost per cycle}}$$

External Q: $$Q_e = \frac{2\pi(\text{energy stored})}{\text{energy lost through the coupling hole per cycle}}$$

Unloaded Q: $$Q_u = \frac{2\pi(\text{energy stored})}{\text{energy lost (ohmic) in cavity walls per cycle}}$$

Sample Q: $$Q_\chi = \frac{2\pi(\text{energy stored})}{\text{energy dissipated in the sample per cycle}}$$

According to definition $1/Q_\chi \sim \chi''\eta$ where is the imaginary part of the rf susceptibility and η is the filling factor for the sample in the cavity. In the microwave reflection measurements Q_e and Q_{int} play a dominant role, where

$$\frac{1}{Q_{int}} = \frac{1}{Q_u} + \frac{1}{Q_\chi} \qquad \text{A.1}$$

The reflection coefficient Γ is defined as the ratio between the reflected amplitude E_r and the incident amplitude E_o.

$$\Gamma = \frac{|E_r|}{|E_o|} \qquad \text{A.2}$$

The resonant cavity is coupled to the waveguide by means of a coupling hole. The coupling parameter β is defined as a ratio between Q_e and Q_{int}

$$\beta = \frac{Q_e}{Q_{int}} \qquad \text{A.3}$$

and Γ is given by [A.1]

$$\Gamma = \frac{1 - \beta}{1 + \beta} \qquad \text{A.4}$$

If the aperture size is adjusted so that $Q_e = Q_{int}$ the resonant cavity is matched to the waveguide. This condition is known as a critical coupling and results in all the incident power being absorbed by the cavity. For smaller apertures Q_e is bigger than Q_{int} and this situation is known as the undercoupled case. The measurements were carried out with an undercoupled cavity. The detecting diode was working in the linear region of its sensitivity. By going through the resonance the voltage on the diode changes in proportion to the change in E_r. These changes are related to the change of Q_χ of the cavity. For the undercoupled case Γ and β are given by the relation

$$\Gamma = \frac{1-\beta}{1+\beta} \qquad \text{A.5}$$

From eq.A.3

$$\beta = \frac{Q_e}{Q_{int}} = \frac{Q_e}{Q_u} + \frac{Q_e}{Q_\chi} \qquad \text{A.6}$$

and therefore from eq. A.5

$$\frac{|E_r|}{|E_o|} = \frac{(1 - \beta_o - x(H_{dc}))}{(1 + \beta_o + x(H_{dc}))} \qquad \text{A.7}$$

where $x(H_{dc}) = \frac{Q_e}{Q_\chi} \sim \chi''\eta$ is a function of the applied dc magnetic field and $\beta_o = \frac{Q_e}{Q_u}$. For ultrathin films $x(H_{dc})$ is significantly smaller than β_o and therefore the change in the reflected amplitude ΔE_r can be evaluated by using a Taylor expansion.

$$\frac{(E_{ro} + \Delta E_r)}{E_o} = \frac{(1 - \beta_o - x(h_{dc}))}{(1 + \beta_o + x(h_{dc}))} = (1 - \beta_o - x(hdc)) \frac{(1 - \frac{x(h_{dc})}{(1+\beta_o)} + ..)}{(1 + \beta_o)} \qquad \text{A.8}$$

$$\Delta E_r \sim \frac{\chi''\eta\, E_o}{(1+\beta_o)^2} \qquad \text{A.9}$$

The diode is proportional to ΔE_r therefore intensity is proportional to E_o, to the filling factor η and to the factor $(1+\beta o)^2$ which is coupling

dependent. Note that this formula (eq. A.9) is valid only for a large enough β_o that the diode operates in the linear regime.

A.2 Detailed procedure of measurements of the exchange coupling .

This subsection has a unique character. It is intended to provide a detailed recipe for taking FMR measurements which were used to evaluate the exchange coupling in Fe/X/Fe trilayers on the 36GHz spectrometer used at the Surface Science Laboratory, Simon Fraser University. The preparation for the measurements, a short description of the apparatus, the data acquisition system and computer programs are described.

A schematic diagram of the 36 GHz spectrometer is shown in figure A.1. Figure A.2 shows a schematic diagram of the connections among the low frequency electronic components.

The reflected microwaves (see Figure A.1) are converted into a dc signal by a detection diode. This dc voltage is measured by voltmeter (Fluke model 8842A, device address "02") and sent to a PC computer via an IEEE488 bus. The detection diode is also connected to the input of two lock-in amplifiers (Princeton Applied Research model 116 and 5209). The applied dc magnetic field is modulated at 176Hz by a pair of Helmholtz coils mounted on the magnet pole pieces. The diode signal is measured by a lock-in amplifier (PAR model 116). The output of this lock-in amplifier is connected to the voltmeter (Fluke model 8842A, device address "01") and the derivative of the FMR absorption signal, as a function of dc magnetic field, is sent to the PC computer via the IEEE488 bus. The second lock-in amplifier

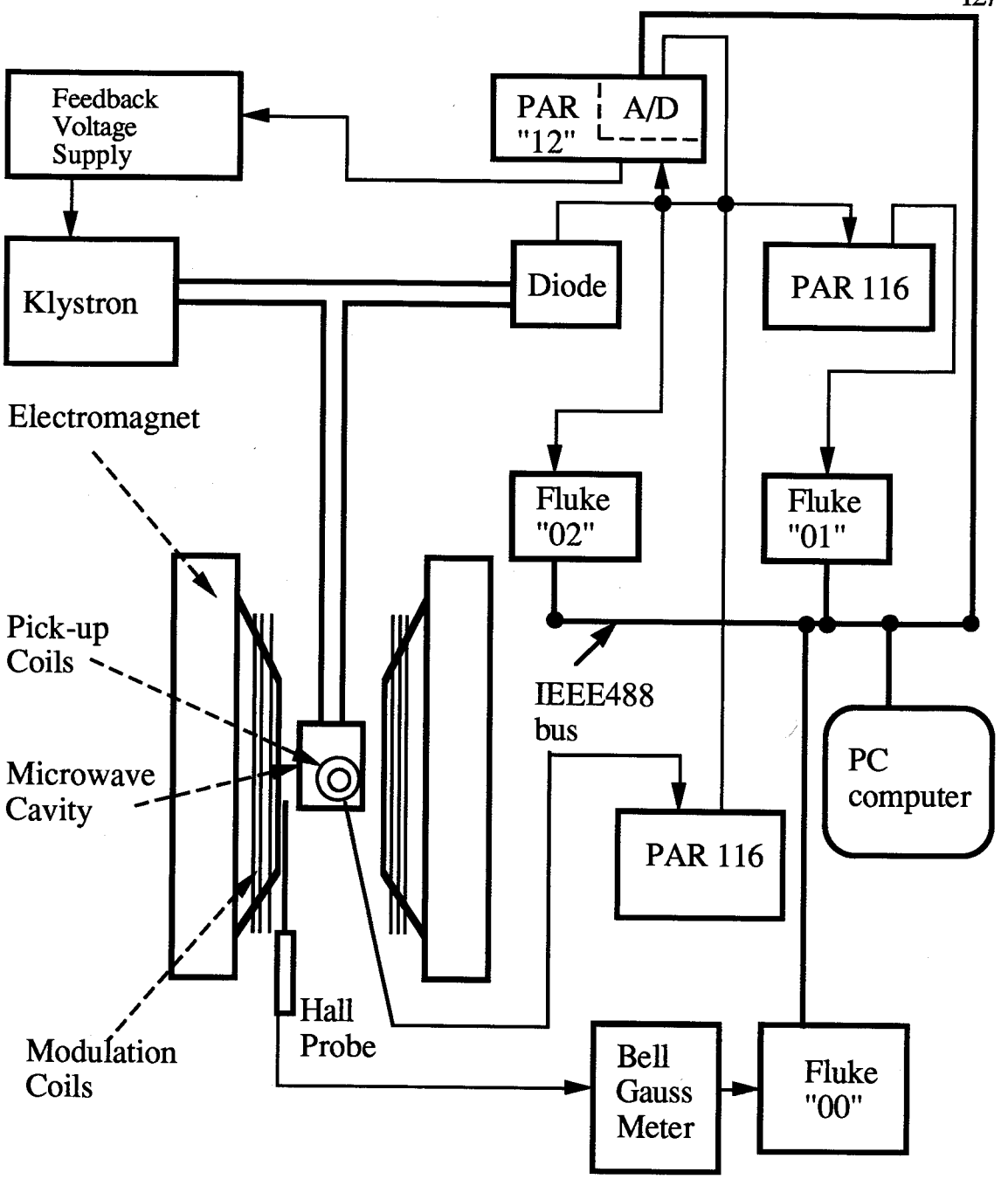

Fig. A.2 Block diagram of connections among electronic components.

(PAR model 5209) is connected to the same detector diode but is tuned to the frequency (68kHz) which is used to modulate the klystron reflector. The output of this lock-in amplifier is part of the feedback which stabilizes the klystron frequency.

The Hall probe (Bell model 630) is attached close to the center of the magnet pole piece. The output from the Hall probe electronic box is connected to the voltmeter (Fluke mode 8842A, device address "00") and data are send to the computer via the IEEE488 bus.

A small pick-up coil is attached permanently to a stainless steel can which separates the resonant cavity and the microwave track from the air. This pick-up coil is placed close to the resonant cavity and is used to monitor the modulation of the dc magnetic field. Its signal is sent to the third lock-in amplifier (PAR model 116). The output of the lock-in amplifier is connected to channel 1 in the A/D convertor which is a part of the lock-in amplifier (PAR model 5209, device address "12") with IEEE488 bus. Note that the main purpose of this lock-in is to stabilize the klystron frequency. The modulation amplitude is dependent on the strength of the dc field and therefore the derivative of the absorption signal must be normalized by the modulation field seen by the measured sample.

The data acquisition is controlled by a PC computer equipped with a IEEE488 card. Two programs in Turbo Pascal were used to collect data:"First" and "FirstNew". Both of them must use the IEEE488 driver which is loaded after the computer reboots by pressing the "i" key. The programs are located at the directory c:\tp5. The program "First" can collect 3 or 4 channels using two Fluke voltmeters (device addresses "00" and "01") and the lock-in amplifier (channel 1 and 2 in A/D convertor, device address "12"). The program "FirstNew" collects 4 channels using three Fluke voltmeters (device address "00", "01", and "02") and the lock-in amplifier (channel 1 of A/D convertor, device address "12"). The accuracy of the A/D convertor is 1mV in the ±15V range therefore it is only suitable for a pick-up

coil signal which is of the order of a few Volts. The Hall probe signal, detector diode signal and the derivative of the FMR signal must be collected from Fluke voltmeters which guarantee an appropriate accuracy.

All measurement were taken with a constant incoming microwave power. The value of this power can be adjusted by a variable attenuator.

Programs used for data acquisition are a self explanatory. The main menu is easy to follow. Therefore they will not be described here in detail. Each procedure can be repeated. For the magnetic field calibration two fields must be chosen. A typical time interval between two points taken during the measurements is 0.7-1.0 s. The quality of the data can be examined on the computer screen using the "Graph" procedure.

After all data at the given temperature are saved on the disk it is necessary to measure the resonant microwave frequency using a microwave frequency meter.

A few corrections have to be carried out before the final analysis. A nuclear magnetic resonance (NMR) probe was used to calibrate the dc magnetic field with an accuracy ±1 Oe. The field NMR corrections to the magnet Hall probe voltages are linear in field. Such corrections are incorporated by the program TMBE (#R TMBE 1=DataFile.FMR 2=OutputFile).

The $K_{1\perp}^{eff}$ and $4\pi M_{eff}$ for each individual layer must be calculated using the program FANT located in the KRSH account. This program is well documented in the laboratory computer folder and will not be described here. The two programs called BILAYERS3 and TRILAYERS2 were used to analyze the exchange coupling data. These program were written by Dr. B. Heinrich. BILAYERS3 uses the GANDER graphic shell and requires a

Tektronix graphic terminal (T4013 or T4015). The program TRILAYERS2 uses a Fortran least square fitting routine MINUIT from the CERN libraries available on mainframes. The program TRILAYERS2 uses a VT100 terminal. All programs are available on request.

The program BILAYERS3 is used to evaluate the strength of the exchange coupling. To run the program the following commands must be executed:

#SO BILAYERS3(3) {program is loaded}

&CPLOT=DABSOR {program will calculate the derivative of the absorption line}

&START=value of lower boundary of the dc magnetic field

&FROM=value of lower boundary of the dc magnetic field {this value will be display on the screen}

&END=value of upper boundary of the dc magnetic field

&STEP=value of step used in calculation of resonance line

&DAT {all parameters are shown - updated values should be introduced}

&D1=thickness of layer "1" (cm)

&D2=thickness of layer "2" (cm)

&CUBK1=value of the in-plane cubic anisotropy for layer "1" (ergs/cm^3)

&CUBK2=value of the in-plane cubic anisotropy for layer "2" (ergs/cm^3)

&PER1=value of the uniaxial field for layer "1" (kOe)

&PER2=value of the uniaxial field for layer "2" (kOe)

&F=microwave frequency (GHz)

&ANGLE=value of the angle from the easy magnetic axes (rad)

&GIL1=value of the Gilbert parameter for layer "1" (Hz)

&GIL2=value of the Gilbert parameter for layer "2" (Hz)

&ACOP=value of the exchange stiffness coupling coefficient between layer "1" and "2" (ergs/cm) {J^{AB} = 4ACOP/a where a is Fe lattice constant}

&CALC {start of calculations - program will display a new set of resonance lines. Using commands WHERE or RES the positions of calculated lines can be obtained and compared with the experimental results. The value of ACOP should be changed until the differences between the calculated resonance positions and the experimental results are smaller then 50 Oe for the easy and hard axis.}

&STOP {to terminate program BILAYER2}

The final adjustment of the magnetic parameters is carried out in order to keep the exchange coupling independent of the orientation of M_S with respect to the crystallographic axis. The least squares fitting routine MINUIT is used in program TRILAYER2. The file of parameters must be created; all parameters from DAT call plus the experimental positions of the easy and hard axis for the optical and acoustic peaks. The program TRILAYER2 will be used to adjust the values of the in-plane four-fold anisotropies (see eq. 5.2), the uniaxial anisotropies (see eq. 5.3) with the value of the exchange coupling coefficient. To execute program the following commands must be executed:

#R TRILAYER2+XPS3 {program is loaded}

[1]PLOAD ParametersFileName {parameters are loaded}

[2]DLOAD DataFile {data are loaded}

[3]LP {list all parameters}

[4]FIX ParameterNumber, ...,ParameterNumber
{appropriate parameters are fixed;for the first run all except the exchange coupling are fixed}

[5]SIMP 1E-6 {program performs a minimization}

[6]REL CUBK1, CUBK2 {in-plane anisotropies are released}

[7]SIMP 1E-7 {program performs a minimization with three parameters}

[8]FIX CUBK1, CUBK2 {in-plane anisotropies are fixed again}

[9]REL PER1, PER2 {uniaxial anisotropies are released}

[10]SIMP 1E-8 {program performs minimization with three parameters}

[11]REL CUBK1, CUBK2 {in-plane anisotropies are released}

[12]SIMP 1E-9 {program performs minimization with five parameters}

After a minimization converges the parameters are printed and the program is terminated using the command STOP. Note that all previous calculations were based only on positions of the acoustic and optical modes without taking into account the intensities. In order to check the uniqueness of the fit program BILAYER2 is run again with the new set of parameters and the experimental derivatives of FMR absorption signal are compared with theoretical lines, (see for example Figure 5.6). The agreement between the experimental and calculated intensities ensures that the minimization converged to a real minimum and therefore the calculated magnetic parameters are meaningful.

References:

1.1 B. Heinrich, K.B. Urquhart, A.S. Arrott, J.F. Cochran, K. Myrtle, and S.T. Purcell, Phys. Rev. Lett. **59**, 1756 (1987)

1.2 B. Heinrich, S.T. Purcell, J.R. Dutcher, J.F. Cochran, and A.S. Arrott, Phys. Rev. B **38**, 12879 (1988)

1.3 P. Grünberg, R. Schreiber, Y. Pang, M.B. Brodsky, and H. Sowers, Phys. Rev. Letter. **57**, 2442 (1986)

1.4 M.N. Baibich, J.M. Broto, A. Fert, F. Nguyen Van Dan, E. Petroff, P. Eitenne, G. Creuzet, A. Friederich, and J. Chazelas, Phys. Rev. Lett. **61**, 2472 (1988).

1.5 S.S.P. Parkin, N. More, and K.P. Roche, Phys. Rev. Lett. **64**, 2304 (1990)

2.1 W.F. Egelhoff Jr., private communication

2.2 D. Briggs and M.P. Seah, Practical Surface Analysis by Auger and X-ray Photoelectron Spectroscopy, John Wiley & Sons, New York (1987), p.95

2.3 L.E. Davis, N.C. MacDonald, P.W. Palmberg, G.E. Riach, and R.E. Weber, Handbook of Auger Electron Spectroscopy, Physcal Electronics, Minnesota, (1978)

2.4 M.P. Seah and W.A. Dench, Surface and Interface Analysis **1**, 2, (1979)

2.5 P.R. Pukite, Reflection High Energy Electron Diffraction of Interface Formation., Ph.D. Thesis, University of Minnesota, (1988)

2.6 S.T. Purcell, Structural and Magnetic Properties of Ultrathin Epitaxial Nickel Grown on Iron (001) Surface., Ph.D. Thesis, Simon Fraser University, (1989)

2.7 E. Bauer, in Techniques of Metalls Research, ed. by R.F. Bunshach, John Wiley &Sons - Interscience, New York, 1969, vol.2, p.201

2.8 C.S. Lent and P.I. Cohen, Surf. Sci. **139**, 121 (1984)

2.9 J.H. Neave, B.A. Joyce, P.J. Dobson and N. Norton, Appl. Phys. **A31**, 1 (1983)

2.10 J.M. Van Hove, P.R. Pukite, P.I. Cohen, J. Vac. Sci. Technol. **B3**(2), 563 (1985)

2.11 A.S. Arrott, B. Heinrich and S.T. Purcell, Kinetics of Ordering and Growth at Surface, ed. by M.G. Lagally, Plenum Press, New York, 1990, p.321

3.1 E. Bauer, Z. Kristallogr. **110**, 372 (1958)

3.2 R.L. Lyles, Jr., S.J. Rothman and W. Jager, Metallography, **11**, 363 (1978)

3.3 K. Urquhart, The magnetic properties of ultrathin films of Fe(001) grown on Ag(001) substrates, Ph.D. Thesis, Simon Frase Univ., 1989

3.4 B. Heinrich and A.S. Arrott, to be published in Phys. Rev. B.

3.5 J. Kirschner, 5th Joint MMM Intermag Conference, Pittsburgh 1991, J. Appl. Phys., **70**, 5938 (1991)

3.6 P. Hahn, J. Clabes, M. Henzler, J. Appl. Phys. **51**, 2079 (1980)

3.7 B. Heinrich, A.S. Arrott, J.F. Cochran, Z. Celinski and K. Myrtle, NATO Advanced Study Institute on the Science and Technology of Nanostructured Magnetic Materials, Greece 1990, eds. G.Hajipanais and G.A. Prinz, Plenum Press, New York, 1991, p.15

3.8 E. Fullerton, privite communication

3.9 S.T. Purcell, private communication

3.10 W.F. Egelhoff, Jr. and I. Jacob, Phys. Rev. Lett. **62**, 921 (1988)

3.11 D.T. Jiang, D. Crosier, and B. Heinrich, Phys. Rev. **B44**, 6401 (1991)

3.12 G. Zajac, S.D. Bader, and R.J. Fiddler, Phys. Rev. B**31**, 4947 (1985)

4.1 J.R. Macdonald, Proc. Phys. Soc. **A 64**, 968 (1951)

4.2 B. Heinrich, J. Kirschner, M. Kowalewski, J.F. Cochran, Z. Celinski, and A.S. Arrott, Phys. Rev. B **44**, 9348 (1991)

4.3 W.F. Brown Jr., Micromagnetics, Interscience Publisher, New York, (1963)

4.4 F. Hoffmann, Phys. Stat. Sol. **41**, 807 (1970); F. Hoffmann, A. Stankoff, and H. Pascard, J. Appl. Phys., **41**,1022 (1970)

5.1 J. Unguris, R.J. Celotta and D.T. Pierce, Phys. Rev. Lett. (1991)

5.2 S.T. Purcell, W. Folkerts, M.T. Johnson, N.W.E. McGee, K. Jager, J. an de Stegge, W.B. Zeper, W. Hoving, and P. Grunberg, Phys. Rev. Lett., **67**, 903 (1991)

5.3 S. Demokritov, J.A. Wolf, P. Grunberg, and W. Zinn, in Proceedings of the Materials Research Society, Spring Symposium, 1991 (to be published).

5.4 M.B. Brodsky, J. Magn. Magn. Mater., **35**, 99 (1983)

5.5 V.L.Moruzzi and P.M.Markus, Phys. Rev. B **39**, 471 (1989)

5.6 H.Chen, N.E.Brener, and J.Callaway, Phys. Rev. B **40**, 1443 (1989)

5.7 S.Blügel, B.Drittler, R.Zeller, and P.H.Dederichs, Appl.Phys. **A49**, 457 (1989).

5.8 S. Bouarab, C. Demangeat, A. Mokrani, and H Dreysse, to be published in Phys. Letter A

5.9 G.Bergmann, Phys.Rev., B **23**, 3805 (1981)

5.10 C.Liu, and S.D.Bader, Physica B **161**, 253 (1989)

5.11 B.Hillebrands, P.Baumgart, and G.Guntherodt, Appl.Phys., **A49**, 589 (1989)

5.12 W. Weber, D.A. Wesner, G. Guntherodt, and U. Linke, Phys. Rev. Lett., **66**, 942 (1991)

5.13 W.B. Muir, J.F.Cochran, J.M. Rudd, B.Heinrich, and Z. Celinski, 1990 Strasbourg Spring MRS Meeting, J. Mag. Mag. Mater., **93**, 229 (1991)

5.14 J.F.Cochran, J.M. Rudd, W.B. Muir, B.Heinrich, and Z. Celinski, Phys. Rev. B **42**, 508 (1990)

5.15 B.Heinrich, Z. Celinski J.F.Cochran, A.S.Arrott, and K. Myrtle, 5th Joint MMM Intermag Conference, Pittsburgh 1991, J. Appl. Phys., **70**, 5769 (1991)

5.16 B. Heinrich, J.F. Cochran, A.S. Arrott, S.T. Purcell, K.B. Urquhart, J.R. Dutcher, and W.F. Egelhoff, Jr., Appl. Phys. A**49**, 473 (1989)

5.17 B. Heinrich, J.F. Cochran, and R. Hasegawa, J. Appl. Phys., **54**, 3690 (1985)

5.18 V. Kambersky, Czech. J. Phys. **B26**, 1366 (1976); V. Korenman and R.E. Prange, Phys. Rev. **B6**, 2769 (1972)

5.19 Z. Celinski and B. Heinrich, 5th Joint MMM Intermag Conference, Pittsburgh 1991, J. Appl. Phys., **70**, 5935 (1991)

5.20 B. Heinrich et al., to be published

5.21 J.J. Krebs, P. Lubitz, A. Chaiken, and G.A. Prinz, Phys. Rev. Lett., **63**, 1645 (1989)

5.22 W.R. Bennett, W.Schwarzacher, and W.F. Egelhoff Jr., Phys. Rev. Lett., **65**, 3169 (1990)

5.23 S.S.P. Parkin, R. Bhadra, and K.P. Roche, Phys. Rev. Lett., **66**, 2152 (1991)

5.24 D.H. Mosca, F. Petroff, A. Fert, P.A. Schroeder, W.P. Pratt, Jr., R. Laloee, and S. Lequien, J. Mag. Mag. Mat., **94**, L1 (1991)

5.25 R.Miranda et al. to be published in J. Mag. Mag. Mat.

5.26 B.Heinrich, Z.Celinski,J.F.Cochran, W.B. Muir, J.Rudd, Q.M. Zhong, A.S.Arrott, K.Myrtle, and J. Kirschner, Phys. Rev. Lett., **64**, 673 (1990)

5.27 B.Heinrich, Z.Celinski, K.Myrtle, J.F.Cochran, A.S.Arrott, and J. Kirschner, J. Mag. Mag. Mater., **93**, 75 (1991)

5.28 Z.Celinski, B.Heinrich, K.Myrtle, and J.F.Cochran, NATO Advanced Study Institute on the Science and Technology of Nanostructured Magnetic Materials, Greece 1990, eds. G.Hajipanais and G.A. Prinz., Plenum Press, New York, 1991, p.77

5.29 B. Heinrich, Z. Celinski, K. Myrtle, J.F. Cochran, M. Kowalewski, A.S. Arrott, and J. Kirschner; 35th MMM Conference, San Diego 1990, J. Appl. Phys., **69**,5217 (1991)

5.30 Z. Celinski and B. Heinrich, J. Mag. Mag. Mater., **99**, L25 (1991)

5.31 Z. Celinski, B.Heinrich, J.F.Cochran, W.B. Muir,A.S.Arrott, and J. Kirschner, Phys. Rev. Letter, **65**,1156 (1990)

5.32 Z. Celinski, B. Heinrich, and J.F. Cochran, 5th Joint MMM Intermag Conference, Pittsburgh 1991, J. Appl. Phys., **70**, 5870 (1991)

5.33 P. Grünberg, S. Demokritov, A. Fuβ, R. Schreiber, J.A. Wolf, and S.T. Purcell, (invited) ICM 1991, Edinburgh, to be published

5.34 B.A. Gurney, D.R. Wilhoit, V.S. Speriosu, and I.L. Sanders, IEEE Trans. Magn., **26**, 2747 (1990)

5.35 J. Stroscio et al., to be published, private communication

5.36 F. Herman, J. Sticht, and M. van Schilfgaarde, Proc. Spring MRS Meeting, Anaheim (1991) to be published

5.37 D.M. Edwards and J. Mathon, R.B. Muniz, and M.S. Phan, Phys. Rev. Lett., **67**, 493 (1991)

5.38 Y. Wang, P.M. Levy, and J.L. Fry, Phys. Rev. Lett., **64**, 2304 (1991)

5.39 N. Garcia and A. Hernando, J. Magn. Magn. Mater., **99**, L12 (1991)

5.40 R. Coehoorn, submitted to Phys. Rev. B

5.41 K.B. Hathaway and J.R. Cullen, paper presented at International Workshop on Spin-valve Layered Structures, Madrid, Sep. 9-12, 1991

5.42 P. Bruno and C. Chappert, paper presented at International Workshop on Spin-valve Layered Structures, Madrid, Sep. 9-12, 1991

5.43 D.M. Deaven, D.S. Rokhsar, and M. Johnson, paper presented at 1991 March Meeting of the American Physical Society, 18-22March 1991, Cincinnati, Ohio

5.44 M. Hansen, Constitution of Binary Alloys, McGraw-Hill Book Company, Inc., New York, 1958

A.1 G. Feher, Bell Syst. Tech. J., **36**. 449 (1957)